Czech Technical University in Prague
Faculty of Nuclear Sciences and Physical Engineering
Department of Physical Electronics

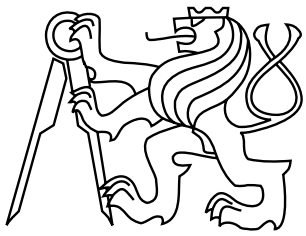

# Multi–Foil X–Ray Optical Systems and Image Analysis in High–Temperature Plasma Physics

**Ph.D. THESIS**

**Libor Švéda**

Supervisor: Ladislav Pína
Doctoral Study Programme: Applications of Natural Sciences
Doctoral Study Subprogramme: Physical Engineering

Prague, July 2006

## Declaration

The thesis was worked out at the Department of Physical Electronics, Faculty of Nuclear Sciences and Physical Engineering of the Czech Technical University in Prague, from October 2003 to July 2006.

"I hereby declare that I have worked out the thesis independently while noting all the resources employed as well as co-authors. I consent to the publication of the thesis under Act No. 111/1998, Coll., on universities, as amended by subsequent regulations."

Prague, July 14, 2006

signature

This work would never reach its current shape without the support of four beautiful ladies. I would like to thank to Veronika Semencová for a number of discussions and measurements, to Hana Jirglová for helping me with the thesis layout and other formalities, to Radka Havlíková for the measurements and a great help with the administrative stuff, and to Ivana Stoklasová for being patient with my English.

The discussions with Adolf Inneman and Ladislav Pína led to the optics designs which are now an inseparable part of the work, therefore their support was essential. It would be also much more difficult to present the results of our work at conferences without the support and help of René Hudec and Jiří Limpouch.

The finalisation of the work would be impossible without the help of Milan Bašta, Tomáš Caudr, Martin Kempa, and Michaela Skulinová who have read the work and corrected a number of mistakes. However, I was able to produce a lot of the new ones in the meantime.

The work would have never been started without the support of my family, my parents and my two brothers.

And last, there were people in these years who came into my life, as well as those who were already there, who have given me the strength to continue.

Thank you all.

**Název práce:** Multifóliová rentgenová optika a analýza obrazu ve fyzice vysokoteplotního plasmatu
**Autor:** Mgr. Libor Švéda
**Katedra (ústav):** Katedra fyzikální elektroniky, Fakulta Jaderná a Fyzikálně Inženýrská, České Vysoké Učení Technické
**Školitel:** Doc. Ing. Ladislav Pína, DrSc.

**Abstrakt:** Prezentujeme výsledky výzkumu zobrazovacích schopností Multi–Foil optiky a dále několika modifikací, které mají řešit nalezené problémy. Zabýváme se jak zobrazováním statickým tak skenovacím. Část věnovanou Multi–Foil optikám doplňujeme návrhem rotačně symetrické optiky, která vznikla v průběhu hlavního výzkumu jako vedlejší produkt. Výsledky získané v první části používáme jako vstup pro analýzu metod zpracování obrazu z Multi–Foil optik. Ukazujeme několik standardních metod a jejich potřebných modifikací aplikovaných na simulovaná data. Řešíme vhodnost použití různých metod pro různá vstupní data.

**Klíčová slova:** návrh optiky, rentgenová optika; račí oko; Multi–Foil optika; zpracování obrazu, kondenzor, multi–resolution

**Title:** Multi–Foil X–Ray Optical Systems and Image Analysis in High–Temperature Plasma Physics
**Author:** Mgr. Libor Švéda
**Department:** Department of Physical Electronics, Faculty of Nuclear Sciences and Physical Engineering, Czech Technical University in Prague
**Supervisor:** Doc. Ing. Ladislav Pína, DrSc.

**Abstract:** We present the results of an analysis of imaging properties of the Multi–Foil optics and its several modifications, which should solve the found problems. We show both the pointed and the scanning observation simulations. We add a short overview of the axially symmetric design which have emerged as a spin–off during our main research. The outputs of the first part are the inputs for the second part, where we analyse the image processing methods suitable for processing the data from Multi–Foil optics. We show several standard methods, and their necessary modifications, applied to a number of simulated images. We discuss the right selection of the processing method based on the nature of the input data.

**Keywords:** optics design; X–Ray optics; Lobster Eye; Multi–Foil optics; image processing; condenser; multi–resolution

# Contents

Unless defined in another way, abbreviations and acronyms have the following meanings:

| | |
|---|---|
| ASM | All–Sky Monitor |
| CWT | Continuous Wavelet Transform |
| DWBA | Distorted–wave Born Approximation |
| DWT | Discrete Wavelet Transform |
| EUV | Extreme Ultra Violet |
| FFT | Fast Fourier Transform |
| FOV | Field Of View |
| FWHM | Full Width at Half Maximum |
| HEA | High Energy Astronomy |
| $\Im$ | Imaginary part of |
| K | degree of Kelvin |
| KB | Kirkpatrick–Baez optics |
| LE | Lobster Eye |
| LEO | Low Earth Orbit |
| LR | Lucy–Richardson |
| $M_\odot$ | Mass of the Sun |
| mas | mili arc second |
| MEM | Maximum Entrophy Method |
| MFO | Multi–Foil Optics |
| MR | Multiresolution |
| OTF | Optical Transfer Function |
| PCD | Photon Counting Device (Detector) |
| PSF | Point Spread Function |
| $\Re$ | Real part of |
| RMS | Root Mean Square |

# Chapter 1

# Preface

There exists a large number of X–Ray applications, from medical imaging, material science, or microchip manufacturing to astronomical observations. The X–Rays have to be adjusted, guided, or focused in a number of these applications.

A typical appearance of an X–Ray optics is rather surprising for anyone familiar with "classical" optics. It often looks like a polished golden pipe rather than a regular optics known from the visible light. Yet, still, the optics is works perfectly and the strange shape is governed by the interaction of X–Rays with matter.

One can be surprised even more if something consisting of a number of side–by–side arranged plates is introduced to him, without any hesitation, as an X-Ray optics. Such a strange system is called the Lobster Eye Optics (or more generally the Multi–Foil optic) and has some specific and interesting properties.

It was theoretically developed thirty years ago [1, 2], but was not successfully built until the last decade. Unfortunately, we were not able to find any kind of already produced and satisfactory review of the Lobster Eye optical properties or optical deformations. Hence, our work was originally devoted to the study of this kind of optics, to perform a more sophisticated analysis of its optical properties, to be able to predict and to design the right configuration. As a consequence, we wanted to review the methods of image processing amenable to images obtained from this kind of optics.

As normally, after we started to understand the properties of this original optics and as we were able to simulate its properties, new and new questions and problems have been discovered. They led us to several basic modifications of the original design, which should correct or improve its properties in various ways. Moreover, some other interesting designs have come to light. These designs had almost nothing in common with the Lobster design, but we have created a universal tool for simulations and we have used it for solving specific problems which we encountered during the work.

Therefore, in this work, we will:

- show the currently used optics designs, the concepts, and the basic motivation (Chapter 2)
- show the methods and means which have been used in the design of any of our presented optics (Chapter 3)
- show and describe several interesting optics designs, some of which were points of our original main concern and some of them have appeared as a kind of spin–offs (Chapter 4)
- show how to process the data obtained from the Multi–Foil optics for both laboratory and astronomical purposes (Chapter 5)

When describing the optics design, we were trying to follow the same structure rules for each of them:

- original motivation for the optics — why such an optics would be needed, what should be the benefits
- general concept description & design — what should the optics look like, how it should solve some particular problems which were the reason for developing it, designing some particular optics
- computer simulation — prove that the concept really works, show the optical properties of some particular optics, try to generalize the results
- summary — tell whether the optics truly solved the initial request, try to specify the problems, where it can be successfully used

When describing the data processing, we have concentrated on two basic deconvolution methods and for each of them we have tried to:

- show a brief theoretical background and describe the algorithm
- apply the method to some particular data, both astronomical as well as non–astronomical
- try to decide which one should be used under which conditions

We have tried not to write long stories, which would be boring and confusing, especially if speaking about images and optical properties. Instead, we have tried to write a shorter and structured text with a lot of images. We only write the parts which

can not be found nicely written in other works, or give just a very brief introduction to give the reader the first insight and necessary concepts. We believe that this leads to an increased information density and clearness.

# Chapter 2

# Introduction

## 2.1 Sources

We are going to briefly review the relevance and/or importance of the Wide Field X–Ray Optics or the Multi–Foil Optics for a variety of sources, ranging from particular laboratory sources and applications to astronomical and exotic sources.

### 2.1.1 Laboratory Sources

There is a strong demand for bringing as much photons as possible from the diverging source into a small focal area for further processing in both industry and academic research. X–Rays from a plasma source or the bremsstrahlung radiation are simply collected from a large solid angle and concentrated into the point where the experiment is carried out or the production process is performed. The EUV lithography is a nice example of such an experimental setup. Gathered X–Rays are sometimes processed by other subsequent optics to produce a more precisely defined beam.

The most common way how to gather the X–Rays is to concentrate them using an axially symmetric X–Ray condenser with just a single reflection. The single reflection can be a problem for the imaging [3], but it is completely sufficient in this case, because no remarkable imaging properties are required from the condenser.

However, the Multi–Foil Optics (see Section 4.1) can be a good alternative to the currently used axially symmetric condensers. The effective collecting solid angle, which is the main figure of merit for the condensing system, is comparable with the axially symmetric condenser of the same external dimensions. However, it can be built at lower costs.

The question of the cost becomes important in a situation where relatively large

fluxes are concentrated. Therefore, the properties of the material of the condenser degrade relatively rapidly. Moreover, the whole condenser becomes radioactive. In fact, the condenser has to be treated as a consumable and has to be replaced quite often in this case, which makes the question of the price very important.

### 2.1.2 Space Sources

Space sources are typically thermal X–Ray sources which are often mixed with the synchrotron radiation. Therefore, we can expect to detect X–Rays of all energies, but we often observe in the soft X–Ray band due to the typical spectrum profile of the sources (from 0.1 keV to 10.0 keV for instance). All the sources are extremely bright and extremely variable. They can last only a few seconds (GRBs) or a few days (SNe). This fact, together with the distribution on the sky, implies that it is difficult to perform a statistically significant observation of these sources using the Narrow Field Instruments.

All space sources can be considered to be point sources, especially these extra–galactic ones. The source structure can sometimes be resolved for those inside the Galaxy, but the angular resolution has to be $\sim 1$ arc sec or better.

Our understanding of these sources would largely benefit from the usage of the sensitive Wide Field X–Ray optics used for sky monitoring and/or observations, which does not currently exists. The comparison of current and/or proposed missions is plotted in Figure 2.1.

#### Sun and Stars

It has been shown [5] that almost each star at the main sequence of the Hertzsprung–Russell diagram (HR diagram) [6], the Sun among them, is an X–Ray source. The origin of X–Rays and the overall X–Ray intensity depends on the position in the HR diagram.

Hot (above $\sim 10^4$ K) and massive (above $\sim 15\mathrm{M}_\odot$) stars, from O–type to early B–type, are strong X–Ray emitters. X–Rays are produced in hot and shocked regions of massive radiatively driven stellar winds. The X–Ray flux variability is relatively low.

Late B and A type stars, i.e. temperature $7500 - 10000$ K and mass $3.2 - 15$ $\mathrm{M}_\odot$, lack an X–Ray emission, although there are some detections of X–Rays of unknown origin from several late B stars. Absence of the X–Ray emission is due to the absence of massive radiatively driven stellar winds while the convection zone and strong magnetic fields are still missing. There is no way how to heat a stellar wind and a corona

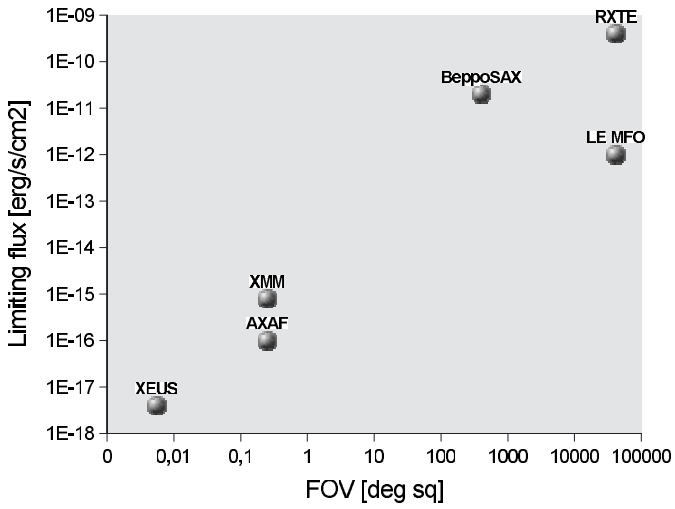


**Figure 2.1:** *The comparison of an expected Limiting Flux and a typical Field of View of current and/or proposed astronomical X–Ray instruments [4]. Fluxes are for typical use of each instrument, hence the exposure time differs. For the RXTE and the LE, the effective FOV is almost the whole sky due to the scanning observations, although the real pointed FOV is smaller. The limiting flux is rather informative, because each of these instruments are intended to be used in a different way. While the XMM and the XEUS are used mainly for spectroscopy, therefore essentially the large effective area of the telescope is needed, the AXAF mission has the unique angular resolution and the limiting flux is taken from one of the observed deep fields after a long exposure time. The limiting flux for the BeppoSAX is taken for* 30 *ks exposing time, while the limiting fluxes for the RXTE and the LE ASM are for daily scans (several revolutions).*

to sufficient temperatures under these conditions.

From F type down to M type, i.e. temperatures below 7500 K and mass below 3.2 $M_{\odot}$, the X–Ray emission appears again and all of these stellar classes are relatively strong X–Ray sources. The corona is heated by dynamo–generated magnetic fields. A large convection zone is important in this process. X–Ray flux spans over a wide range of magnitudes and is more variable than in case of hot stars. The X–Rays represent an important probe to convection, angular momentum evolution, and magnetic dynamos. The Sun belongs exactly to this part of the HR diagram.

X–Rays are also generated during strong flares, which are well known in case of the Sun. The flares are catastrophic releases of magnetic energy leading to particle acceleration and electromagnetic radiation. Durations and energies of the flares may vary over many orders of magnitude.

In fact, X–Rays are systematically monitored from the Sun and detected at a few nearby stars using X–Ray All Sky Monitors. The sensitivity of the current All Sky Monitors is too low for detecting a larger number of stars. The coverage of the sky

by more sensitive narrow field instruments is poor, on the other hand, and thus only a small number of stars have been observed in X–Rays.

### X–Ray Binaries

X–Ray binaries and cataclysmic variables are both objects consisting of two bodies. One is an ordinary star of the main sequence and second is a compact object. A matter is transferred from the less evolved star, typically the larger and the less massive one, to its compact companion. In case of the matter accreting onto a white dwarf we speak about a cataclysmic variable, in case of a neutron star or a black hole we speak about an X–Ray binary. The matter swirling around the compact star is heated up and emits in X–Rays.

There are two main types of X–Ray binaries. The High Mass X–Ray Binaries (HMXBs), where material is transferred via a strong stellar wind from a massive O–type or B–type star to the compact object, and the Low Mass X–Ray Binaries (LMXBs), where the less evolved star does not have sufficiently strong stellar wind. The secondary star fills its Roche lobe [7] and the matter is transferred through the Lagrangian point L1 [8].

All X–Ray binaries are highly variable and luminous X–Ray sources. Their luminosity can change at the timescales from minutes to days. The total X–Ray output of the Galaxy is comparable to the total output of all X–Ray binaries in the Galaxy, or, in other words, X–Ray binaries are dominant X–Ray sources in the Galaxy. The total number of X–Ray binaries in the Galaxy has been estimated to only 700 [9]. However, the total flux from all of them and also the overall X–Ray output of the Galaxy can be changed by a factor of $2 - 3$ because of the variability or the outburst of just one individual source!

### Supernovae

Supernovae are giant explosions of the stars. One kind of supernovae, the less bright, is believed to be a nuclear detonation of carbon+oxygen (C+O) white dwarfs. The matter is accreting onto the dwarf in an X–Ray binary in such a speed, that the mass of the accreted matter exceeds the so called Chandrasekhar limit [10] and nothing can stop the explosion. These are Supernova type Ia.

The rest of supernova types is believed to be a result of a massive star evolution. Extremely massive stars, above 8 $M_\odot$ at the final stage or $10 - 30$ $M_\odot$ during their life, consume the hydrogen in their interiors at high speeds. After the consumption of the whole amount of the fuel, the pressure of the radiation is no longer preventing the outer parts of the star from falling towards the center. The star starts to collapse,

the pressure increases. Because of the extreme mass of the star, there is no way for the gas to stop the "free–fall" of the stellar outer parts. The immense gravitational energy released during the fall causes a giant explosion. For a while (minutes), a single star can be more luminous at all wavelengths than the whole galaxy.

Hundreds of Supernovae have been observed in visible light, but only a few in X–Rays [11, 12], unfortunately typically a long time after the explosion. There is simply only a small number of Narrow Field instruments or just low sensitivity Wide Field instruments at the orbit. Therefore, there exists no observation of the explosion itself.

#### Gamma Ray Bursts

Gamma Ray Bursts are extremely bright and short flashes of gamma rays, often accompanied by an X–Ray emission. It has been shown in the last decade that GRBs are extra–galactic sources and, because of their extreme apparent intensity, that GRBs are the most luminous events in the known Universe.

The sky distribution of several thousands of already detected GRBs seems to be rather uniform and temporally random. The duration of the GRBs has a bimodal distribution. The first maximum is at $\sim$ 2 s and the second at $\sim$ 90 s [13]. While the origin of the first group remains unclear, the second group is believed to be connected to the catastrophic end of extremely massive stars, the so called hypernovae (hypernova even much brighter than supernova). The GRB is then only an observation of the central energy source (the hypernova) influence on the surrounding medium.

Therefore, because of the random spatial distribution and short durations, it is extremely difficult to observe the GRBs by the narrow field instruments even if the first observation is done by the Gamma–Ray wide field satellite and a message about the event is spread through the network.

## 2.2 Reflective X–Ray Optics Principles

### 2.2.1 X–Ray Reflectivity

Several main interactions of X–Rays with matter are typically considered:

- Photoelectric absorption
- Thomson scattering

- Rayleigh scattering
- Compton scattering

It is sufficient to deal only with the photoelectric absorption and the Thomson scattering for soft X–Rays, i.e. $\sim 0.1 - 10.0$ keV photons.

Interactions are then given by the atomic scattering factor $f = f_1 + if_2$ [14]. Although the values of $f$ can be calculated in principle, one comes into troubles for soft X–Rays. The models work mostly for higher photon energies or for much smaller energies. Hence, the atomic scattering factors are typically measured and tabulated for all important elements [15, 16] and are simply accessible via the internet [17].

Now, let us suppose that $f$ is the known function of photon energy and the material. The photoabsorption cross-section $\mu_a$ can be calculated as:

$$\mu_a = 2r_0\lambda f_2 \tag{2.1}$$

where $r_0 \simeq 2.818\times10^{-15}$ m is the classical electron radius [18] and $\lambda$ is the wavelength. The transmissivity $T$ for a stab of thickness $d$ is given by:

$$T = e^{-\rho_n\mu_a d} \tag{2.2}$$

where $\rho_n$ is the number of atoms per unit volume in the material. The refractive index $n$ for a given material can be approximated as:

$$n = 1 - \frac{\rho_n r_0\lambda^2(f_1 + if_2)}{2\pi} \tag{2.3}$$

Please note that the refractive index becomes a complex number for soft X–Rays and typical materials (carbon, iron, silicon...). Moreover, the real part, which is responsible for refraction, is very close to but less than unity.

In our work, we need to calculate the reflectivity and transmissivity of X–Rays at the interface of two materials, where we can generally use the Fresnel equations. Here the interface is the surface where two media with different refractive indexes $n_1$ and $n_2$ are touching. An electromagnetic wave comes from the first medium. If $\vec{E}$ is the electric intensity vector, index $_\perp$ stands for the vector (polarisation) perpendicular to the plane of incidence, $_\parallel$ stands for vector (polarization) parallel to the plane of incidence, $_i$ stands for the incoming photon, $_r$ for the reflected one, $_t$ for the transmitted one, $\theta_i$ is the angle of incidence (angle between the normal to the interface and the incoming beam), $\theta_t$ is the angle of transmitted beam (angle between the normal to the interface and the transmitted beam), then:

$$\frac{E_{r\perp}}{E_{i\perp}} = \frac{n_1\cos\theta_i - n_2\cos\theta_t}{n_1\cos\theta_i + n_2\cos\theta_t} \tag{2.4}$$

$$\frac{E_{r\parallel}}{E_{i\parallel}} = \frac{n_2 \cos\theta_i - n_1 \cos\theta_t}{n_2 \cos\theta_i + n_1 \cos\theta_t} \tag{2.5}$$

are Fresnel equations [19, 20], which can be rewritten as follows:

$$\frac{E_{r\perp}}{E_{i\perp}} = \frac{n_1 \cos\theta_i - \sqrt{n_2^2 - n_1^2 \sin^2\theta_i}}{n_1 \cos\theta_i + \sqrt{n_2^2 - n_1^2 \sin^2\theta_i}} \tag{2.6}$$

$$\frac{E_{r\parallel}}{E_{i\parallel}} = \frac{n_2^2 \cos\theta_i - n_1 \sqrt{n_2^2 - n_1^2 \sin^2\theta_i}}{n_2^2 \cos\theta_i + n_1 \sqrt{n_2^2 - n_1^2 \sin^2\theta_i}} \tag{2.7}$$

Reflectivity $R$ or transmittance $T$ can be calculated as:

$$R_\perp = \left(\frac{E_{r\perp}}{E_{i\perp}}\right)\left(\frac{E_{r\perp}}{E_{i\perp}}\right)^* \tag{2.8}$$

$$R_\parallel = \left(\frac{E_{r\parallel}}{E_{i\parallel}}\right)\left(\frac{E_{r\parallel}}{E_{i\parallel}}\right)^* \tag{2.9}$$

where $^*$ means the complex conjugate.

The only difference for X–Rays if compared to visible light in typical optical applications is that the refractive index is a truly complex number and its complex conjugate has to be really used for computing the reflectivity.

Because the wavelength of X–Rays is comparable to the atomic distances, no interface can be considered to be perfectly flat. The roughness of the interface has to be taken into account. The reflected intensity $I_d$ has to be corrected as the first approximation:

$$I_d = I_u e^{-\left(\frac{4\pi\sigma\cos\theta_i}{\lambda}\right)^2} \tag{2.10}$$

where $I_u$ is the intensity reflected in case of an ideally flat interface, and $\sigma$ is the RMS micro–roughness of the surface. The effect of a rough surface will be discussed in more details in Section 3.2.1.

The key phenomenon for reflective X–Ray optics is the total external reflection. It is an analogy of the total internal reflection in visible light. Because the real part of the refractive index for typical materials is $\Re(n) < 1$, the rays are reflected with $\sim 100\%$ efficiency for incidence angles $\theta_i > \sin^{-1}\Re(n)$ (or grazing angles $\theta_g < \cos^{-1}\Re(n)$). Or, in other words, the more the ray is close to the surface, the higher is the reflectivity.

The 100% efficiency is based on the assumption that the refractive index is a purely real number. Because it has an imaginary part for X–Rays, the reflectivity is always lower, although close to 100% (see Figure 2.2). Because the reflectivity is non–zero only for grazing angles, the reflective optics is often called the grazing incidence optics.

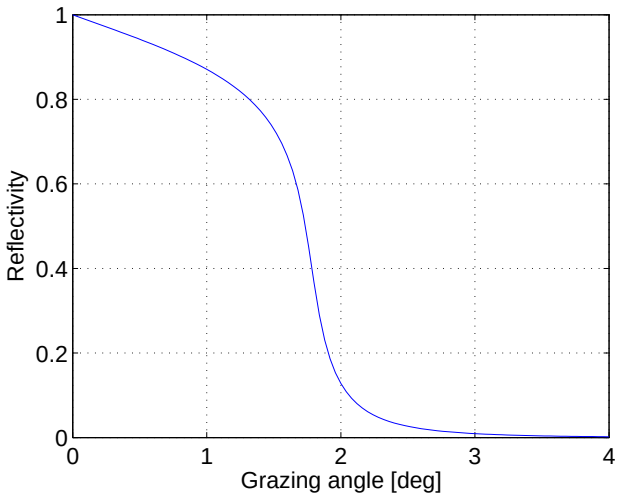


**Figure 2.2:** *An example of the X–Ray reflectivity of a perfectly smooth thick carbon layer [17]. The angle is the grazing angle, i.e. the angle between the ray and the surface. Note that the reflectivity is quite high below* $\sim 2$ *deg due to the Total External Reflection.*

It can be helpful for future reading to emphasize the difference between the angle of incidence and the grazing angle:

**Angle of incidence** is the angle between the ray and the normal to the surface, it is often used in calculations of reflectivity and is well known from visible light.

**Grazing angle** is the angle between the ray and the surface plane, it is equal to $\pi/2 -$ "angle of incidence" and is typically used in X–Ray science.

## 2.3 Common X–Ray Optics

The results of the previous section can lead us to the conclusion that for focusing from infinity into a single point we can use a narrow parabolic mirror where the photon strikes the mirror far before the focus. This is the exact opposite of a classical mirror telescope where the light is reflected back to the detector from an almost flat parabolic mirror.

Although this idea is mathematically absolutely correct, it is often shown that the so called Abbe Sine Condition can not be sufficiently fulfilled for any design with only one reflection at grazing angles [3]. Although there is some discussion, this fact is widely used and the optics is constructed to overcome this problem. The Abbe

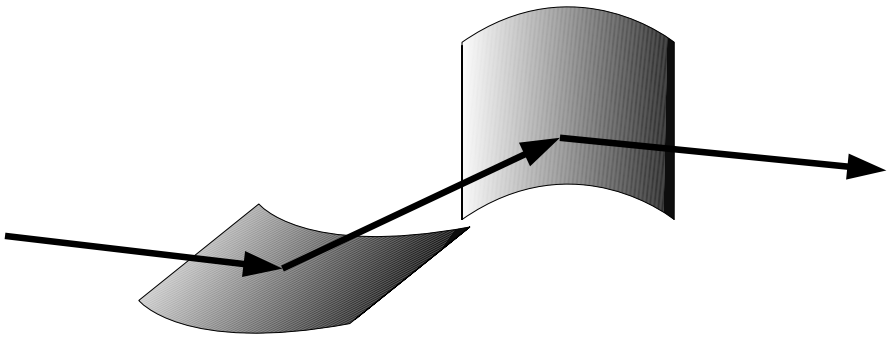

**Figure 2.3:** *A schematic view of the Kirkpatrick–Baez X–Ray optics which focuses rays from infinity into a single point. The ray reflects first from the horizontal parabolic mirror and then from the vertical parabolic mirror. Abbe sine condition is much better satisfied in this case.*

Sine Condition states [21]:

$$u' \sin U' = u \sin U \tag{2.11}$$

where $u'$ and $u$ is the same variable for two different rays, and $u$ and $u'$ are the slopes of the paraxial ray from the object to the image, while $U$ and $U'$ are the slopes of the marginal ray. The marginal ray is the ray in the plain containing the optical axis that starts at the point where the object crosses the optical axis, and touches the edge of the aperture stop of the system.

In other words, violating the above mentioned condition for a single reflection at grazing angles leads to the conclusion that any X–Ray reflecting optics with only a single reflection would suffer from an extreme coma, which is one of the optical distortions. Any off–axis source would be displayed as a comet–like spot, fairly large in this case, with the axis passing through the optical axis.

The problem is so severe for X–Ray optics designs that people had to develop more sophisticated optics designs to solve the problem since the very beginning the X–Ray science.

### 2.3.1 Kirkpatrick–Baez

Kirkpatrick–Baez [22] system was historically the first attempt to reduce the problems of the corrupted Abbe condition at a single reflection X–Ray optics using the "two reflection" design.

The optics is constructed from two orthogonal sets of specially shaped mirrors. The sets are placed one behind each other and each reflects in only one of the orthogonal directions. For an instrument focusing from infinity to a single point, each mirror

has to be one–dimensionally shaped into a parabola. The mirror reflects exactly in the direction into which it is shaped. A schematic view is plotted in Figure 2.3.

However, the optics plotted in Figure 2.3 has only a small effective area because the front area of each of the mirrors is just tiny. Thus, instead of one mirror in each direction, we use a set of mirrors to get a larger effective area. Each mirror of the single set has to focus into a common focal line, while the whole system will focus into a single point.

The Field of View (FOV) can be estimated from the critical angle. The critical angle is the angle at which the intensity falls steeply, in the ideal case, or falls below 1/2 in practice. The first guess for the FOV can be set equal to the critical angle.

For a typical photon energy 1 keV and gold coated mirrors with good surface quality the critical angle is $\sim 2$ deg. Consequently, the FOV as large as $\sim 2 \times 2$ deg$^2$ can be expected.

A serious vignettagion effect has to be taken into account for a proper image processing, but the deformation of the image shape near the edge of the FOV is relatively small if compared to the axially symmetric optics. The reason is that the Kirkpatrick–Baez optics (KB) can be viewed as a small part of a small sector of a large axially symmetric optics. Hence, the image deformation is more or less uniform across the whole image and tends to shift the image instead of changing its shape substantially.

Although the design is relatively simple and can be successfully used, there is a technological complication which had prevented a common usage of such a system at the expense of the Wolter type optics up to the recent years.

The problem is that it is rather difficult to position all the mirrors and even force them to stay in the correct positions. Each single mirror has to be positioned differently, each single mirror has to have a different shape. It is technologically much more simple to do it with an axially symmetric design.

Only in the recent years, when the technology of manufacturing of the Lobster Eyes and the Multi–Foil optics was successfully developed and tested, we can move again back to successful experiments with the Kirkpatrick–Baez optics at adequate costs.

In fact, the Kirkpatrick–Baez Optics is the special case of the Multi–Foil Optics, as presented in Section 4.1.

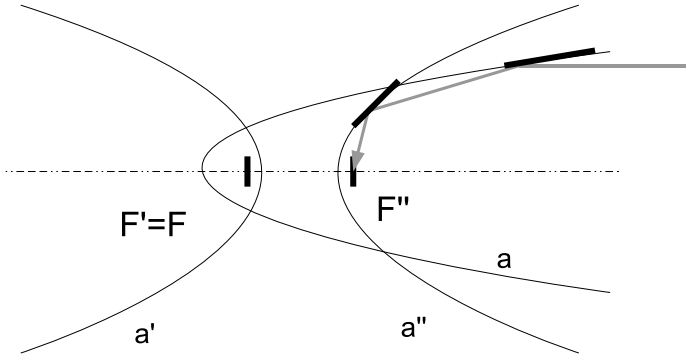


**Figure 2.4:** *Wolter type I X–Ray optics. The ray is reflected from the inner part of the parabolic mirror (a) and then from the inner part of the hyperbolic mirror (a") into the focus F". The focus F of the parabolic mirror is identical with the focus F" of the second part of the hyperbola.*

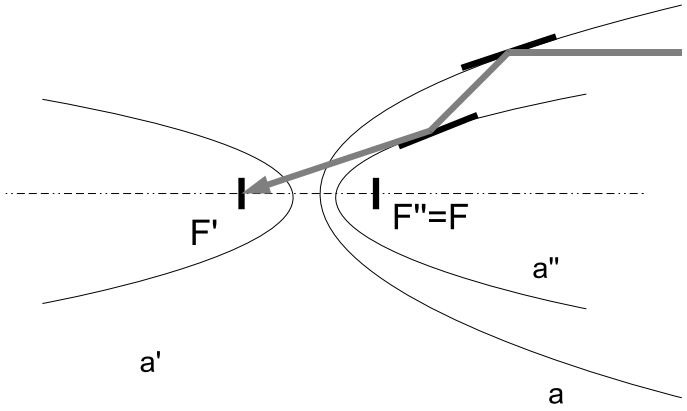


**Figure 2.5:** *Wolter type II X–Ray optics. The ray is reflected from the inner part of the parabolic mirror (a") and then from the outer part of the hyperbolic mirror (a) into the focus F'. The focus F of the parabolic mirror is identical with the focus F" of the second part of the hyperbola.*

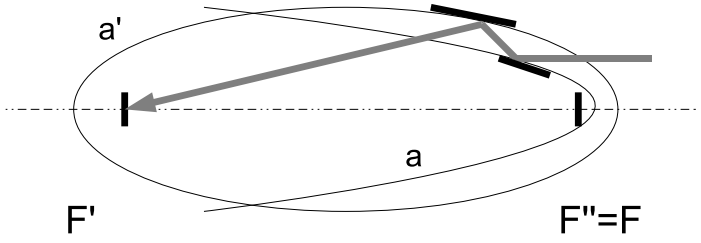


**Figure 2.6:** *Wolter type III X–Ray optics. The ray is reflected from the outer part of the parabolic mirror (a) and then from the inner part of the ellipsoidal mirror (a') into the focus F'. The focus F" of the ellipsoidal mirror is identical with the focus F of the parabolic mirror.*

### 2.3.2 Wolter

The design of axially symmetric X–Ray optics using two reflections was proposed by Wolter [23] in the mid 20th century. He realized that a combination of two aligned rotational quadratic surfaces can focus either from infinity into a single point, or from a single point to a single point. Let us first suppose that we are focusing from infinity into a single point. The following Wolter types can be constructed:

**Wolter I** - a combination of the inner reflection from the parabola and the inner reflection from the hyperbola as plotted in Figure 2.4.

**Wolter II** - a combination of the inner reflection from the parabola and the outer reflection from the hyperbola as plotted in Figure 2.5

**Wolter III** - a combination of the outer reflection from the parabola and the inner reflection from the ellipse as plotted in Figure 2.6

Inner reflection means the reflection from the surface at its convex side, whereas the outer reflection means the reflection of its concave side.

Analogical combination can be created for focusing from a single point to a single point. A combination of inner reflection from the ellipsoid and outer reflection from the paraboloid can be one of the solutions.

The Wolter concept is widely used for both laboratory X–Ray optics and for astronomical X–Ray telescopes. An axially symmetric profile with precisely shaped and polished surface can be machined with a high level of success if compared to any other shape. In case of the Wolter I design, only the inner surface has to be polished and precisely shaped, which is even a larger advantage. Also, in case of the Wolter I design, a number of "shells" consisting of the parabola–hyperbola pair can be nested one into another to get a larger effective area. Hence, the Wolter I is the most widely spread X–Ray optics.

However, because of the axial symmetry of the design and only the small angles at which it can reflect the X–Rays, the Wolter type optics has always rather a small Field of View (FOV). First estimate of the FOV can be set equal to the critical angle for X–Rays supposing a given mirror material.

For the typical photon energy 1 keV and gold coated mirrors with a good surface quality the critical angle is $\sim$ 2 deg. Consequently, the FOV as large as $\sim$ 2 deg in diameter can be expected.

If a large number of nested shells is incorporated in the optics, a serious vignettation effect has to be taken into account for a proper image processing. The deformation of the image shape near the edge of the FOV is also massive.

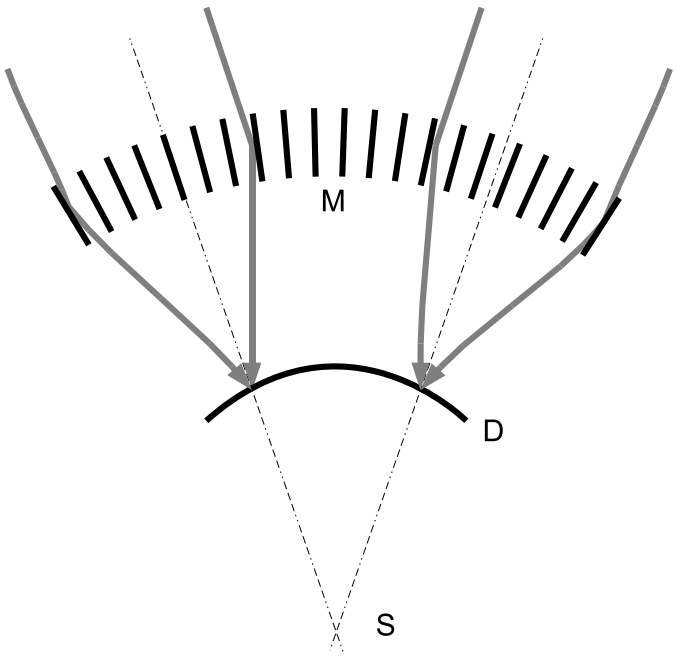


**Figure 2.7:** *A section through the Lobster Eye optics. The mirrors M are aligned onto a cylinder/sphere. The detecting surface D is also curved into a cylinder/sphere. Rays from different sources illuminate different mirrors.*

### 2.3.3 Lobster Eye

The Lobster Eye optics is currently the only focusing X–Ray optics with the large (wide) Field of View (FOV), contrary to the axially symmetric designs and even the KB system.

The concept of the focusing wide FOV X–Ray imaging system was developed in the seventies of the last century, when people realized that nature itself has already solved the problem. Eyes of marine crustaceans have a special structure. They reflect light inside a large number of tiny channels aligned on a sphere. People have realized that exactly the same principle can be used for X–Rays.

A Lobster Eye design for X–Rays was proposed by the Schmidt [2] and Angel [1]. The section of such an optics is plotted in Figure 2.7. It consists of a number of channels (Angel design) or the orthogonal sets of flat mirrors (Schmidt design). They mimic the channels as in case of the Lobsters. The light from the source is reflected by a few mirrors near the axis towards the source and focused onto a curved focal surface.

Thus, we can construct the focusing instrument which can cover the whole $2\pi$ angle

in the one–dimensional case, or $4\pi$ in the two–dimensional case.

The image shape, however, will be substantially deformed and an advanced computer processing has to be applied. When we artificially cut down the FOV or make the optics using the Schmidt design, which has naturally a limited FOV, we can use a planar detector, and image processing is needed only under some conditions.

However, as in case of the Kirkpatrick–Baez optics, the manufacturing problems were immense up to the recent years and first working optics were built in the last decade using several technologies.

Because of its unique nature among the other focusing X–Ray optics, i.e. the wide FOV, we have chosen the Lobster Eye optics as the basic optics for our study. Up to recent days, there exist only a small number of papers. Most of them are about the technological aspects of the LE production. There exists almost no comprehensive paper about the optical properties of the optics and/or the image processing of the data.

Currently, there are two main groups working on the Lobster Eye optics:

**University of Leicester Group:** the group led by George Fraser works on the Lobster Eye using the multi–channel plate technology [24]. The group has a great experience in space X–Ray missions and leads the Lobster ISS project, which is the intended X–Ray scanning telescope onboard the International Space Station.

**Czech Group:** the group uses the technology of the Multi–Foil optics (Section 4.1) and connects people from the Reflex Ltd around Adolf Inneman, the Czech Technical University around Ladislav Pína, and the Astronomical Institute of the Academy of Sciences of the Czech republic around René Hudec.

There also exists a group at the University of Melbourne [25], where a people who were originally working in the Leicester group perform some simulations of the Soft X–Ray All–Sky monitor. However, the output of the group is rather theoretical [25].

There also emerged some purely private companies during the security business boom after the terrorist attacks on New York, which use probably some modifications of the Lobster Eye optics for mobile scanning instruments for police, special forces, and/or airports [26]. The optics is used to focus the back–scattered photons from the scanned object. Unfortunately, because of the purpose of the optics, i.e. the security applications, and because of the potential revenues of the project, there exists almost no detailed information about the project.

# Chapter 3

# Ray–Tracing

## 3.1 Existing Software

There exist a bunch of various kinds of sophisticated ray–tracing softwares, which have already been developed and are actively used. Let us mention the most popular ones:

#### SHADOW

SHADOW [27], a ray–tracing code developed at the University of Wisconsin, has become a standard for tracing the synchrotron X–Ray optics int the last years. The code is powerful, yet quite user unfriendly. Each ray is described by the starting position, the wave vector, and the electric fields of two perpendicular polarisations.

Each ray from the source is traced through an optical system composed of a number of optical elements (mirrors, gratings, crystals etc.). An optical surface can be defined in SHADOW using a combination of internally defined shapes: plane, parabolic, hyperbolic, ellipsoidal, toroidal and polynomial. SHADOW is also able to calculate the interaction with perfect and mosaic crystals. SHADOW encapsulates the database of physical properties of a large ensemble of predefined materials, which can be used to calculate the reflectivity.

#### RAY & REFLEC

RAY [28] is a ray–tracing code developed at the BESSY (Berlin electron storage ring company for synchrotron radiation). The code supports a number of radiation sources with a special emphasis on the synchrotron radiation. The optical elements include

mirrors of various shapes, gratings, zone plates, foils, or crystals.

REFLEC [29] is based on a large data set of optical constants and/or atomic scattering factors for UV and X–Ray radiation and is used by RAY to calculate the reflections and/or overall interaction with matter.

## 3.2 Developed Software

We have decided to create our own code and/or system for simulating the X–Ray optics. There were several reasons for our decision:

- If we have to write the code ourselves, we have to better understand the process of X–Ray interaction with the matter. This is a kind of educational reason, basically.
- Much faster implementation of potential changes, because of our perfect knowledge of our own code.
- Code design philosophy providing a simple incorporation into various specialized simulations, where the ray–tracing is just one part of the whole computer experiment.

In fact, each of the reasons itself can not be sufficient for the decision to write a new code, but the combination is fairly important to us. Although the code brings nothing new in principle, it is perfectly suited for further usage in specialized ray–tracing simulations thanks to the library/object design. The simulations include:

- ray–tracing of non–point sources, in fact of the complex and unusual sources
- ray–tracing of the scanning observation of the sky based on the satellite X–Ray source catalogue
- incorporation into specialized design and/or optimising codes for various kinds of optics

We have decided to include only the non–polarized rays and no diffraction elements into our code. Although this is a substantial drawback if compared to the codes mentioned in Section 3.1, it is sufficient for all kinds of optics which we intend to deal with.

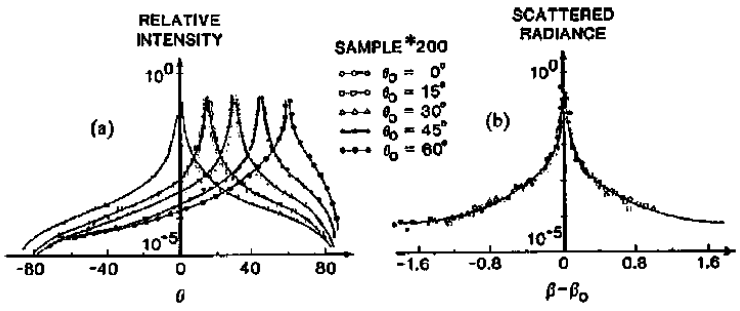


**Figure 3.1:** *Scattered intensity versus a) scattering angle and b) cosine of scattering angle. The profiles match each other in the second case. Harvey et al. [31]*

### 3.2.1 Linear X–Ray Scattering

Scattering can be calculated according to various models. We can use kinematical, dynamical, or a semikinematical (Distorted–wave Born Approximation — DWBA) approaches [30], for example. We have adopted the approach of Harvey et al. [31] for our ray–tracing code. We assume a random, homogeneous, and isotropic mirror surface and a Gaussian surface height distribution.

If a parallel beam strikes a rough surface, a part of the intensity is reflected specularly, while the other part reflects diffusely and hence creates a kind of halo around the specular reflection peak.

If the intensity $I$ is described as a function of the angle of incidence $\theta_0$ and angle of diffraction $\theta$, the scattered intensity depends on both of them. On the other hand, if described in terms of $\beta_0 = \cos\theta_0$ and $\beta = \cos\theta$, the scattered intensity expressed in terms of $\beta - \beta_0$ is almost identical for a large interval of $\beta_0$ (see Figure 3.1).

Thus, the scattering as a function of $\beta - \beta_0$ can be expressed as a linear process with the transfer function:

$$H_s(\hat{x}, \hat{y}) = \exp\left(-(4\pi\hat{\sigma}_s)^2 \left[1 - C\left(\frac{\hat{x}}{\hat{l}}, \frac{\hat{y}}{\hat{l}}\right)/\sigma_s^2\right]\right) \tag{3.1}$$

where $\hat{x}$ means the $x/\lambda$. $\hat{x}$ and $\hat{y}$ are the coordinates on the surface, $\hat{l}$ is the length of the surface, $C$ is the autocovariance function of the surface, and $\sigma_s$ is the RMS roughness of the surface.

Transfer function can be rewritten as

$$H_s(\hat{x}, \hat{y}) = A + BQ(\hat{x}, \hat{y}) \tag{3.2}$$

where

$$A = \exp\left[-(4\pi\hat{\sigma}_s)^2\right] \tag{3.3}$$

$$B = 1 - A \tag{3.4}$$

$$Q(\hat{x},\hat{y}) = \frac{\exp\left[(4\pi\hat{\sigma}_s)^2 C\left(\frac{\hat{x}}{\hat{l}},\frac{\hat{y}}{\hat{l}}\right)/\sigma_s^2\right]}{\exp(4\pi\hat{\sigma}_s)^2 - 1} \tag{3.5}$$

This can be interpreted as follows: the incoming ray is reflected specularly with the probability $A$ and diffusely into the halo with the probability $B$.

The angle spread function $S(\alpha,\beta)$, i.e. how the point source is imaged depending on the cosine of the angles, can be expressed as:

$$S(\alpha,\beta) = F(A + BQ(\hat{x},\hat{y})) = A\delta(\alpha_0,\beta_0) + BF(Q(\hat{x},\hat{y})) \tag{3.6}$$

where $F$ denotes the Fourier transform and $\delta$ is the Dirac delta function.

Some modifications are necessary for the grazing incidence reflection. Equations (3.4)-(3.5) have to be rewritten:

$$A = \exp -(4\pi\hat{\sigma}_s \sin\theta_0)^2 \tag{3.7}$$

$$B = 1 - A \tag{3.8}$$

$$Q(\hat{x},\hat{y}) = \frac{\exp\left[(4\pi\hat{\sigma}_s \sin\theta_0)^2 C\left(\frac{\hat{x}}{\hat{l}},\frac{\hat{y}}{\hat{l}\sin\theta_0}\right)/\sigma_s^2\right]}{\exp(4\pi\hat{\sigma}_s \sin\theta_0)^2 - 1} \tag{3.9}$$

Then, for a scattering simulation, a good knowledge of surface autocovariance function $C$ is needed.

Although the code is well capable of such a simulation and an example is plotted in Figure 3.2, the measurement of the PSD is relatively difficult and we often use the simulation without this feature. It still fits the real situation quite well for all our cases.

### 3.2.2 Final Software Properties

The developed code uses the ray approximation. No diffraction, absorption, and/or wave effects are incorporated. Only the reflectivity and scattering due to the rough surface are calculated as described in sections 2.2.1 and 3.2.1. Although this is a big simplification, it matches the reality quite well because of the typical wavelengths of $\sim 1$ nm and the overall dimensions of the optics.

Currently, we have a set of universal C++ routines for computing the reflectivity, for finding the path of the ray through the optics, to store and to treat various kinds

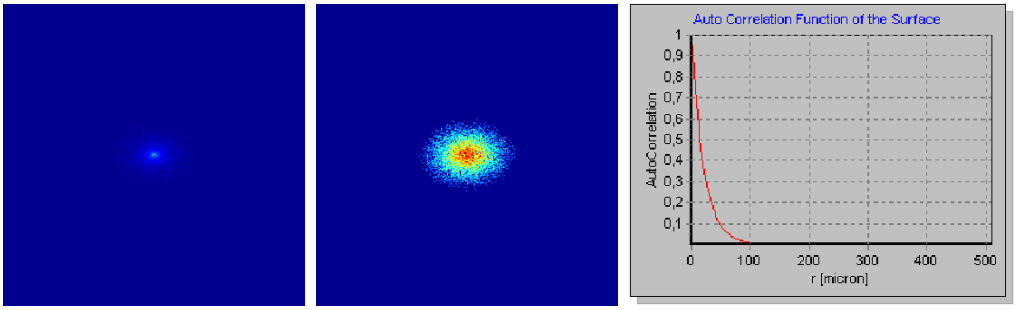


**Figure 3.2:** *An example of the light reflected and scattered of the a rough surface with a given autocovariance function and inclined by* 45 *deg relative to the incoming beam. The reflection and scattering of the surface which have microroughness small compared to the wavelength is plotted on the left, while the simulation of the reflection of the surface having microroughness comparable with the wavelength is plotted in the middle. The autocovariance function of both surfaces is plotted on the right. We can clearly see the asymmetry created by the beam inclination.*

of reflecting surfaces, and to detect the photons by a virtual detector. These routines can be used in a laboratory X–Ray optics simulator as well as in a more specialized piece of software which simulates the astronomical scanning observations.

Currently, we can use the following sources:

- point source in infinity
- point source in a defined distance emitting into a solid angle between two cones sharing the common axis and center
- circular source with a given diameter in a defined distance emitting into a solid angle between two cones sharing the common axis and center
- source of any shape defined by an intensity map in infinity

So far, we have prepared an extension of general abstract classes to hold reflecting surfaces of the following types:

- a rectangle
- an annulus
- a one–dimensionally bent quadratic surface
- an axially symmetric cubic spline surface
- an axially symmetric quadratic surface

Other specialized surfaces are also possible thanks to the modularity of the design, but they have not been implemented yet. Inspite of this fact, we can simulate observations made by all Wolter type telescopes, Kirkpatrick–Baez telescopes, Lobster Eye telescopes, any possible Hybrid Lobster Eye telescope, aspherical axially symmetric optics, and much more even with these several types of surfaces.

The code is able to calculate the reflectivity at the interface of any reflecting surface as described in Section 2.2.1, although supposing zero polarisation. If a measurement of a real surface reflectivity is accessible, like in case of the multi–layers, the code can use this measured reflectivity. Moreover, if the surface material is given with a well measured surface power spectrum density function, the scattered photons are also modeled according to Section 3.2.1.

Additionally, any once created optics can be visualized, saved as a file, and used in any piece of software using our routines. The file format is a plain XML, hence it can be edited manually, in principle, in any text editor. This is especially powerful if these files are prepared with some advanced mathematical software, like Matlab, for instance, to build up some special and complicated optics.

We can obtain images in various scalings and/or color mapping for better visualization as the output of our simulations. All the results can be stored as simple text files (arrays of numbers) and are accessible by any other tool for further processing. We usually use Matlab for further processing of the simulated data.

# Chapter 4

# Designs

We are going to describe several X–Ray optics designs, which we were working on during our studies. Basically, these are the variations and modifications of the Lobster Eye optics, or the so called Multi–Foil optics. We also present completely different designs, which we studied as spin–off technologies of our ray–tracing code development and the Multi–Foil optics studies.

## 4.1 Multi–Foil X–Ray Condenser

We are going to show here one of the actual Multi–Foil optics applications, namely the soft X–Ray condenser. We will describe the process from initial discussions and requirements on the optics for a given experiment, the design process, the manufacturing, and finally the tests of the optics.

### 4.1.1 "Multi–Foil"

Generalizing the concept of the Lobster Eye from Section 4.2, the Hybrid Lobster Eye from Section 4.3, and the Kirkpatrick–Baez optics lead us to the definition of the so called "Multi–Foil" optics [32].

The term "Multi–Foil optics" has been used by the Czech group working on the Lobster Eye optics since the last decade and seems to be successfully spreading over the X–Ray manufacturing community. However, it has not been rigorously defined yet. We use this term to describe the Lobster–like optics which we are typically dealing with. In general, such an optics looks like the one plotted in Figure 4.1. We use the definition of the Multi–Foil optics to match the following properties:

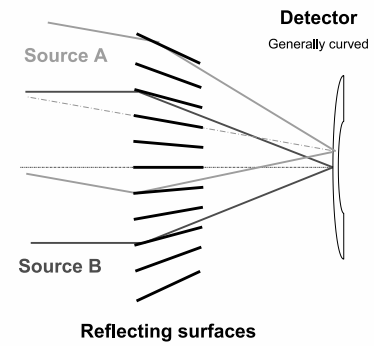


**Figure 4.1:** *The section through the typical Multi–Foil optics design. A number of thin aligned reflecting surfaces is visible. The surface shape can be simply planar, more advanced are parabolic, hyperbolic, or elliptic shapes, but they can have any aspherical shape, in principle.*

- thin reflecting surfaces if compared to the optics dimensions (at least 10× smaller than any other dimension)
- a large number of reflecting surfaces (few tens at least)
- various shapes of reflecting surfaces, generally one dimensionally curved
- typically two orthogonal sets of reflecting surfaces
- various coatings (metal, multi–layers) of the surfaces

We can think of a large number of different optics and/or designs as the manifestations of the Multi–Foil optics. These include:

**Lobster Eye,** which consist of two orthogonal sets of planar mirrors, which are slightly tilted to focus properly

**Hybrid Lobster Eye,** which consists of one set of planar mirrors and one orthogonal set of shaped mirrors, typically shaped into parabolas

**Kirkpatrick–Baez system,** which consists of two orthogonal sets of mirrors shaped into parabolas or ellipses

**Soller Slits,** which are in principle two orthogonal sets of parallel planar surfaces working as a collimator

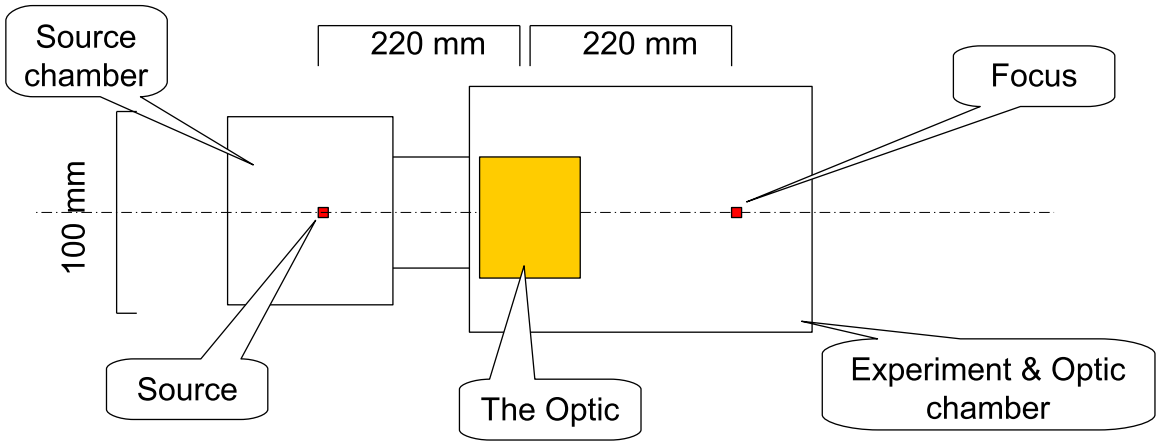


**Figure 4.2:** *A schematic view of the experiment, where the condenser should be used. Soft X–Rays from the source with the diameter* $< 0.5$ *mm should be gathered in a single point in the experiment chamber, where they are used for X–Ray lithography.*

### 4.1.2 Requirements

The initial request for the condenser came from the discussion between the scientists in the Institute of Optoelectronics, Military University of Technology, Warsaw, and the Czech Group working on the Multi Foil Optics. The aim was to use the condenser for collecting photons from the source located at the source chamber into a point in the experiment chamber, where it is used for EUV lithography [33]. A schematic view of the experimental layout is shown in Figure 4.2.

There were several requirements for the condenser:

- working energy range $E \sim 80 - 120$ eV
- focal length $f \sim$440 mm to fit into the already built vacuum chamber
- source diameter $\sim 100 - 500$ $\mu$m
- focal spot diameter $\sim 500 - 1000$ $\mu$m
- restriction for the front area in order to fit into the already built vacuum chamber, $\sim 80$ mm

There naturally exists a number of possible solutions of this problem. Each of the potential solutions has its own advantages as well as disadvantages. Generally, there are two antagonistic requirements. First is a large FOV and a large collecting solid angle to get the best possible effectivity of the condensing system. Large FOV

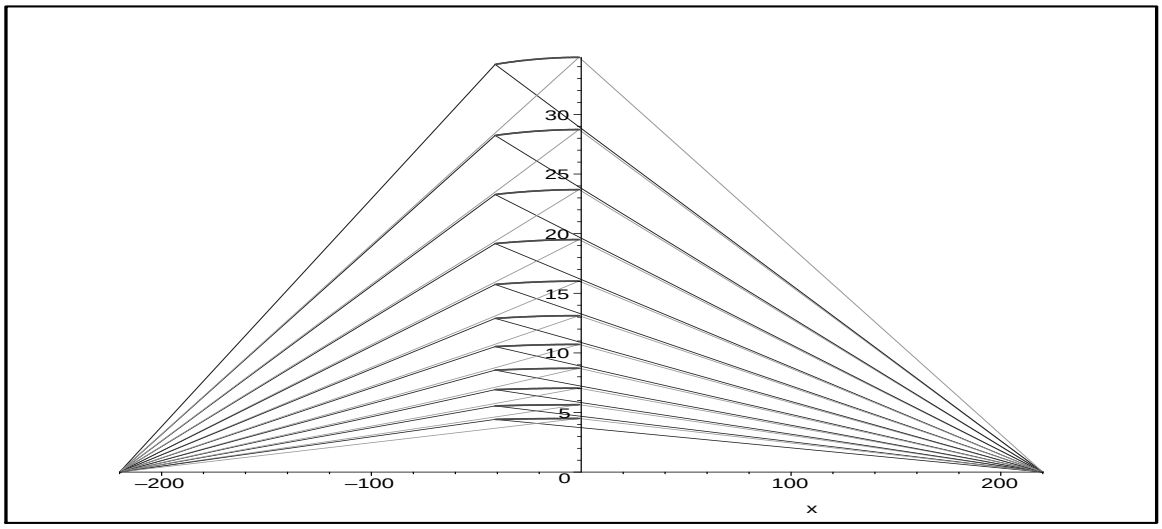


**Figure 4.3:** *One half of the section of the final condenser design. We see rays from the source on the left to the mirrors (rounded and almost horizontally placed curves in the middle) and further to the focal point on the right. All the plotted dimensions are in millimeters. Note the changing distance between the mirrors, which was chosen to make the whole surface of each mirror illuminated. The necessary amount of mirrors is minimized under these circumstances, hence the construction is more simple and cheaper.*

is fortunately enabled here by the low photon energies, at which the reflectivity is quite high up to relatively large grazing angles. Second is the restriction for the focal spot size. It is more difficult to control the distortions and imperfections for larger optics size.

Nevertheless, the conditions above represent a clear definition of the problem to be solved. Additionally, it states the conditions for the the final evaluation and decision whether we have succeeded or not.

### 4.1.3 Design

The first concept was to use the Lobster Eye in Schmidt [2] arrangement to meet the requirements. However, it showed to be impractical after first calculations and simulations, because very short reflecting surfaces had to be used. Otherwise it was not possible to meet the required focal spot size with a given source diameter and to simultaneously utilize the incoming radiation optimally.

As we learned in these initial calculations, we need curved mirrors in order to increase the focusing power of the Lobster Eye. As long as we deal with the single–

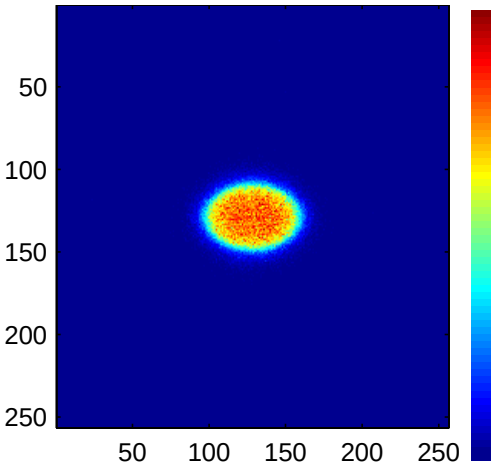


**Figure 4.4:** *The ray–tracing simulation of a* 0.5 *mm source for the final design. The measured FWHM of the peak is* 0.45 *mm and* 0.65 *mm respectively. This means that distortions due to the design itself are relatively small and we have a sufficient confidence level to handle the distortions of the material and imperfections of the fabrication. The axes are in pixels, the pixel size is* 10 $\mu m$.

point–to–single–point focusing system, we can neglect the effect of severe image distortions for off–axis sources, because our source will always be on the optical axis. We need the system to focus from point to point, therefore the mirror shape should be elliptical. To optimally cover the FOV of the system in this case, each mirror has to have not only different curvature, but has to be also in different distance from its neighbour. Mirrors can not be equally spaced, in other words.

After several iterations, where we mostly changed the mirror length, trying to have the mirrors as long as possible to reduce their number, we got the final design consisting of 4 cm long ellipsoidal mirrors. Half of the section is shown in Figure 4.3.

In fact, the final design is a type of the bifacial Kirkpatrick–Baez system focusing from point to point. Term "bifacial" means that reflecting mirrors are on both sides of the optical axis unlike in case of the typical KB system, where the optics is asymmetric.

We performed a number of ray–tracing simulations of the selected design, as well as of each of the particular designs during the iterations. The ray–tracing simulation of the final design for a flat circular photon source with diameter 0.5 mm is plotted in Figure 4.4.

The optics has different magnifications in two perpendicular directions. This is because the reflection occurs in different distances from the source for different directions and the asymmetry is thus induced. Measuring the width of the simulated peak gave us a solid confidence that building the condenser is feasible.

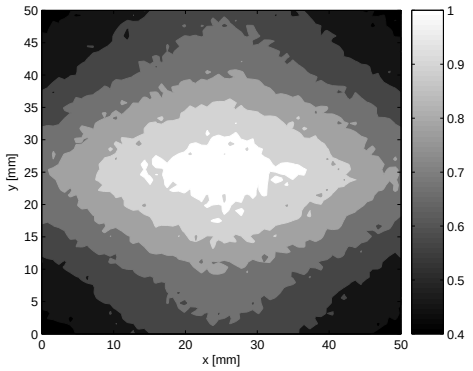


**Figure 4.5:** *The intensity decay of the uniform source caused by the optics design. We have simulated a flat source much larger than* 100 *mm in order to get this picture.*

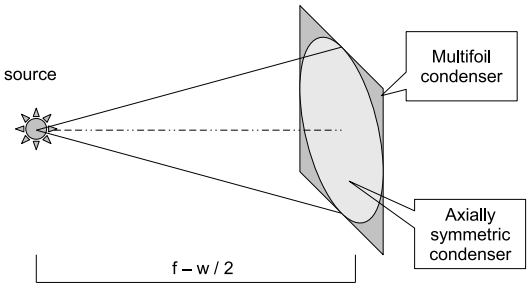


**Figure 4.6:** *The comparison of relative dimensions of the Multi–foil optics (rectangular), which has the point–to–point distance $w$ and focal length $f$, with the largest axially symmetric optics, which have the same outer dimensions.*

The decay of the intensity with the distance from the optical axis can be viewed in Figure 4.5, where an extremely extended uniform source has been simulated. We can see that a FWHM FOV (the intensity falls to 1/2 at the edges of the FOV) is $\simeq 5 \times 5$ cm$^2$, i.e. $\simeq 13 \times 13$ deg$^2$.

The natural question is how many photons are gathered inside the central peak and how many are in the cross structure, which is typical for the MFO/LE design (see Section 4.2.3). The cross structure is strongly reduced because of the curved and optimised mirrors, but is still present. In fact, the ratio between all the photons in the whole cross without the central peak and the photons inside the peak is $\simeq 0.2\%$. The length of the cross bar is $\sim 10$ mm.

We have also compared the solid angle from which we are going to gather the photons in case of the MFO condenser and the maximal solid angle which can be reached with an axially symmetric condenser. A schematic view is plotted in Figure 4.6. The simulation indicates, that the solid angle which is covered by the MFO condenser is $\sim 0.09$ sr. This number includes neglecting the gaps between the mirrors and tells how many photons are reflected at least once. The solid angle which can be reached by the nested shells of an axially symmetric condenser is $\sim 0.18$ sr at maximum. In fact, the number would be smaller because only a finite length of the mirror can be used, or, equivalently, only a limited number of shells is feasible. Therefore, the ratio between the MFO condenser and the ideal condenser with the same outer dimensions is 0.5, but the realistic ratio is somewhere between 0.5 and 1.0.

### 4.1.4 Manufacturing

We have calculated exact parameters of each of the reflecting mirrors and given the numbers as an input to our colleagues in the Reflex, Ltd. Reflex is a small hi–tech company in Prague, Czech Republic, and develops and builds scientific grade X–Ray optics and instruments. The manufacturing itself was performed right there.

Although some technologies used during the manufacturing are proprietary, we are going to mention some of the problems encountered during the manufacturing.

The Reflex company is experienced in the classical Lobster Eye technology, and a number of laboratory samples was already manufactured there. Unfortunately, all the previously created devices of the comparable size and complexity were using only flat mirrors, which is not the case of the condenser. Hence, the technology of shaping the mirrors with a sufficient quality and price had to be developed.

There were people in Reflex who had a great experience with the thermal shaping of glass mirrors [32] at that time. The technology can be described as:

- create a form (mandrel) of a desired shape
- put the thin glass into the form
- increase the temperature of the system according to the precise temperature profile
- after the cooling remove the shaped glass
- you can repeat the process for the next mirror with the same form (mandrel)

The mirrors keep their proper shape after the shaping process, and the internal stress is minimized. Therefore, the probability of glass cracks is substantially reduced even under extreme conditions, such as strong vibrations.

There are several key points of this technology. First, the material and structure of the mandrel. The material has to be thermally and chemically resistant, i.e. the thermal expansivity has to be small, material degradation during a number of cycles of heating and cooling has to be minimal, and it must not chemically interfere with the shaped material (glass). Additionally, it has to be able to be shaped with a high accuracy, the structure of the form material must not destroy the extremely good roughness of the shaped material, but it still has to provide a simple way to remove the shaped glass after the cooling down. Second, a proper temperature profile has to be applied during the forming in order to make the forming process itself possible and to reduce the internal stress. Both of these two key problems have already been solved and the shaping has been successfully used.

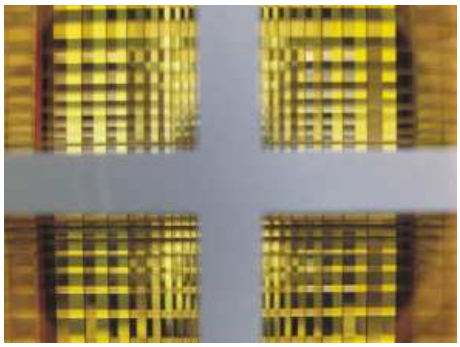

**Figure 4.7:** *Front view of the real condenser. Mirrors with varying distance from each other are clearly depicted. The distance increases for larger off–axis distance. The gray central cross is part of the optics holding structure. It additionally shields the central part of the optics, where no reflection is possible and light from there only worsen the output of the system.*

Although the technology has promising results, it has a great disadvantage for the condenser — the price. As we have mentioned before, each mirror of the condenser has a different shape. If the thermal forming technology is used, it would need a number of different forms, one for each mirror. And this showed to be expensive and impractical in our particular case.

Reflex, Ltd., together with us, have developed a different technology to overcome the problems with the number of needed forms, which suites the condenser design quite well. Although the technological details are confidential, we can describe the key properties of the technology:

- the technology produces modules of the Multi–Foil optics with a desired number of mirrors
- it is simple and/or cheap to create a large number of differently shaped mirrors in one module
- the accuracy of shaping is lower if compared to the thermal shaping, but it can be increased if further development and experiments are accomplished
- the internal stress in the mirrors is still present, it is enlarged in fact
- relatively robust holder for the mirrors has to be used

Finally, the optics based on this new technology was successfully manufactured based on mirrors $8.0 \times 4.0 \times 0.3$ mm$^3$ large. The front view of the optics is plotted in Figure 4.7.

### 4.1.5 Tests

#### Optical Tests

First tests were performed using the visible light in Reflex, Ltd. The optics was illuminated by a 500 $\mu$m light source and the result was detected by a CCD camera with $320 \times 200$ pixels, $14.3 \times 14.3$ $\mu$m$^2$ each. One of the detected images is shown in Figure 4.8. The FWHM of the detected peak is $\sim 1.1 \times 0.7$ mm, which is consistent with the required values.

On the other hand, FWHM values are up to $\sim$ 70% larger than the simulated ones. This is partially due to an imperfect positioning of the source and the detector into the focal points. However, it is mostly caused by misalignments of the reflecting surfaces and mirror profile errors. These are present because of the technological process of shaping.

In fact, the effect would be relatively more significant if a PSF (i.e. an image of a point source) was displayed. The focal spot enlargement is caused mainly by the optics imperfections in this case, not by the source size. For an extended source, on the other hand, the enlargement of the focal spot due to the condenser imperfections is comparable or less than the expansion of the focal spot due to the large source diameter.

There exist several additional reasons for the focal spot enlargement in our laboratory experiment, and all of them are due to measurement in visible light:

- A diffraction on a number of thin reflecting foils is present, which does not occur in case of X–Rays because of extremely short wavelengths.
- Glass foils work as optical fibers for visible light, because light enters the thin foil through the front surface and passes through it, which does not occur in case of X–Rays because they are absorbed in the material after a few microns.
- Multiple reflections between reflecting surfaces themselves are present, which can not be neglected in case of the non–planar geometry and distorted surfaces. Again, it does not occur in case of X–Rays, because the total reflectivity after a few reflections is negligible.

According to our experience, any kind of the Multi–Foil X–Ray optics, which was already manufactured and tested in both visible light and in X–Rays, exhibits a substantially worse peak blurring in the visible light if compared to the measurements in X–Rays. Hence, if the measurement in visible light is consistent with original requirements, we can expect that it fulfills the requirements with even a larger confidence in X–Rays.

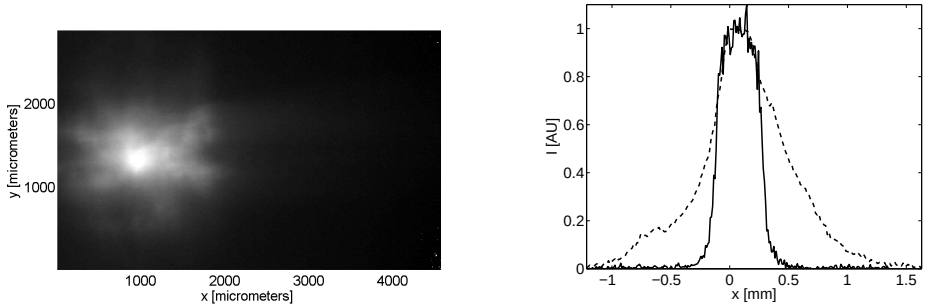


**Figure 4.8:** *Results of optical tests made in Reflex, Ltd., Prague. The focal spot from the* 0.5 *mm source is plotted on the left, while the vertical section is plotted on the right. In fact, we have compared the simulation in the soft X–Rays (solid line) and the vertical profile of the measured focal spot in the visible light (dashed line). Broadening of the real peak relative to the simulation is discussed in the text.*

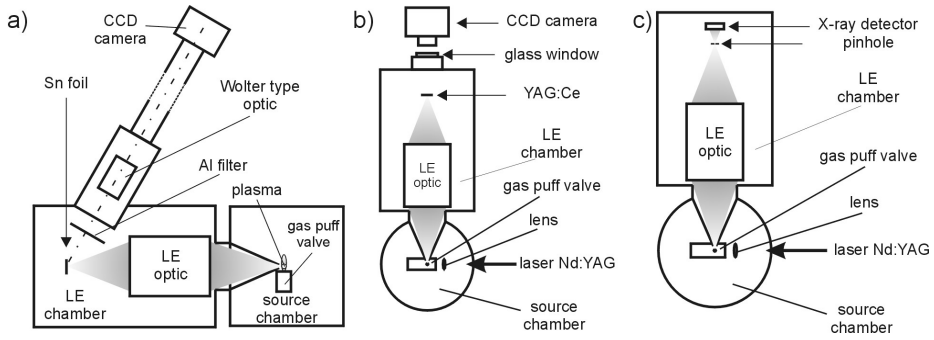


**Figure 4.9:** *Schematic views of experimental arrangements for the intensity measurements in the focal spot: a) EUV imaging with the Wolter type optics, b) luminescence of YAG:Ce crystal, c) scanning with the calibrated pinhole and AXUV 100Zr/C detector.*

### X–Ray Tests

We have supposed during the design that the source has a Gaussian profile with $FWHM = 0.5$ mm. The true source size has to be determined in further experiments, however. For now, we are going to suppose that the Gaussian profile with given FWHM is a correct approximation.

We have used several methods for measuring the focal spot profile. A schematic view of these three different experimental setups is plotted in Figure 4.9.

First, we have imaged the focal spot using an imaging Wolter type X–Ray optics. Focal spot was created on a Sn target. X–Rays emitted under an angle of 60 deg with respect to the condenser optical axis passed through the Aluminum filter and were further focused by the Wolter optics and detected by a back illuminated CCD

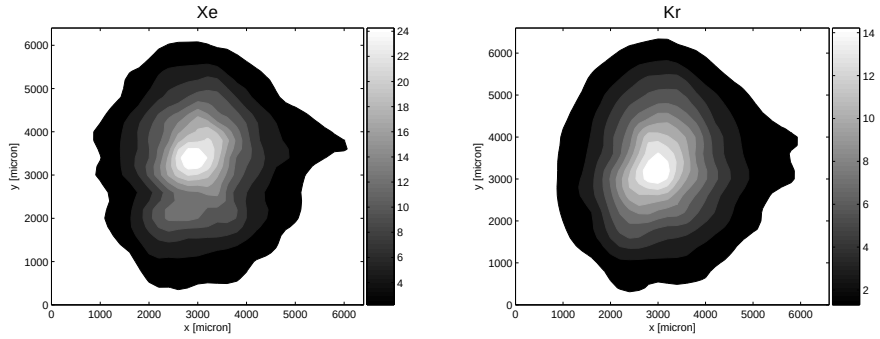


**Figure 4.10:** *The results of absolute measurements of EUV intensity distributions in the focal plane obtained with the use of the calibrated pinhole coupled to the AXUV 100Zr/C detector. Measurements were done at Military University of Technology, Warsaw, by K. Jakubczak.*

camera. The detected image is plotted in Figure 4.11. The image is not corrected for the geometrical inclination and also any possible change of emitting power with the inclination angle was not taken into account.

Second, the profile of the focal spot was mapped using a moving pinhole for two different gases inside the source chamber, Xe and Kr, as plotted in Figure 4.10. The pinhole was placed into a particular position and the flux was measured. Once we have measured a sufficient number of distinct pinhole positions, the interpolation was used to create the profile. Because of the nature of the probing process, each point in the resulting image is based on a completely different set of shots. Thus, an averaging of a large number of shots exactly as in case of the measurements with Wolter optics (Figure 4.11) was incorporated. However, the detection was done in the direction parallel with the optical axis of the condenser.

The condenser tends to focus a circular source into a slightly asymmetric one, as seen in Figure 4.4. We can compare the asymmetry of the simulation of the circular source with the measured data. The ratio between small and large axis for a simulated 0.5 mm source is $\sim 0.67$. The measurement in Figure 4.8 gives the ratio $\sim 0.7$. This means that the source has either a symmetric profile, or the asymmetry is relatively large and it can switch the longer semiaxis from one direction to the other one, what is less probable. However, this assumes that the condenser optical transfer function resembles the simulated one at least in the shape, if not in the overall size. The circular source shape is very probable case here, because an extremely large number of shots had to be used to generate the focal spot map, and this statistically induces that the source shape is near the circular Gaussian profile even if the shape of a single shot is completely different.

The last measurement was created in order to be able to measure the change of

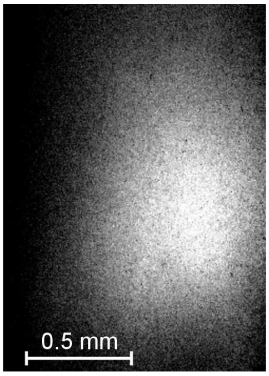


**Figure 4.11:** *Image of the focal spot obtained by the Wolter X–Ray optics after 200 shots. The FWHM of the peak is* 0.6 *mm and* 0.8 *mm respectively.*

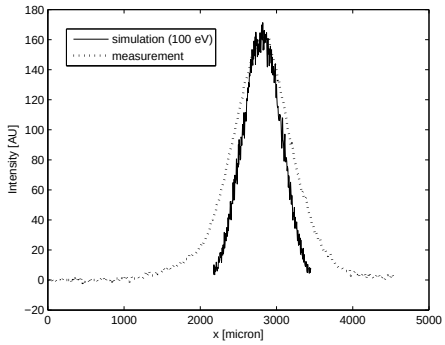


**Figure 4.12:** *The simulation of the Gaussian source with* $FWHM = 0.5$ *mm (solid line) and the measurement in final experimental arrangement. The measurement is the integration of* $\sim 20$ *shots.*

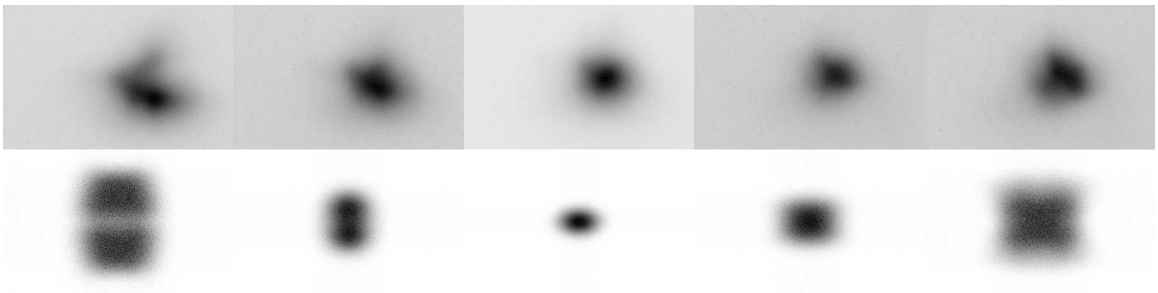

**Figure 4.13:** *Measurements of the source after* $\sim 20$ *shots (upper row) and the simulation (lower row) for different distances from the focus. The distances are (left to right)* $-4$ *mm,* $-2$ *mm,* 0 *mm,* $+2$ *mm, and* $+4$ *mm. Negative value means position the more close to the condenser. Images were taken using YAG:Ce crystal. The intensity is normalized. The camera had* $320 \times 200$ *pixels,* $14.3 \times 14.3$ $\mu m^2$ *each.*

the focal spot with the distance from the optimal focal distance. EUV radiation was striking a thin 20 $\mu$m YAG:Ce crystal. A visible light emitted from the crystal under its irradiation by EUV was registered by a CCD camera, which was mounted outside the experimental chamber behind a glass window. To avoid influence the visible light emitted from the EUV source a 200 nm thick Aluminum filter was placed in front of the crystal. The crystal was mounted on a translate stage enabling to move it along the axis of the condenser.

The profile of a measured focal spot is plotted in Figure 4.12. We compare the measurement with the simulation of the Gaussian source with $FWHM = 0.5$ m. The si-

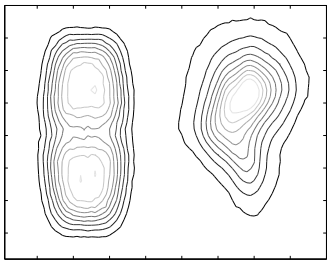

**Figure 4.14:** *A detailed comparison of the simulation (left) and the measurement (right) for focal spot shifted 4 mm towards the condenser.*

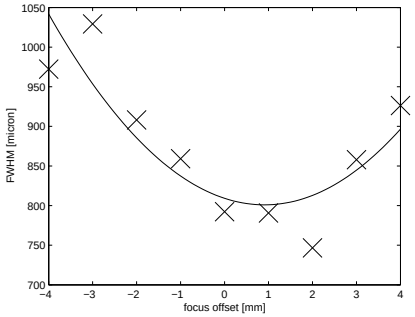


**Figure 4.15:** *Dependance of the FWHM on the focus offset. The FWHM is calculated as the diameter of the circle with area equal to the appropriate section through the peak.*

mulation fits the real spot surprisingly well.

The radiation from the source had to be decreased substantially and a number of shots (20 typically) had to be performed to obtain the images. More strong EUV radiation lead to crystal saturation and probably to the lasing effect in the crystal. This effect is going to be the case of further study.

The change of the focal spot with shifting the detector forward or backward is displayed in Figure 4.13. We have estimated the FWHM of the measured peak for each of the focal spot offsets and plotted the result in Figure 4.15. It shows that the optimal focus is shifted by 1 mm further from the condenser from its current position.

Image 4.13 shows also the simulation of a Gaussian source focal spot at different offsets. The simulation resembles the measurement only at small shifts, i.e. below $\pm 2$ mm. More distant and blurred simulated focal spots tend to be much larger than the measured ones. However, a more close look to the comparison of the large shifts as plotted in Figure 4.14 shows that the overall size of the spots is comparable. The real spot, however, is not flat, but it is asymmetrically peaked because of imperfections of mirror shape and alignment. This means that some mirrors create focus in slightly different focal distances. Note that both displayed sources are normalized to unit maximal intensity. This is a strong indication that the optical transfer function (or the PSF) of the condenser has a more complex profile and that the imperfections in system manufacturing are strong and have to be further studied.

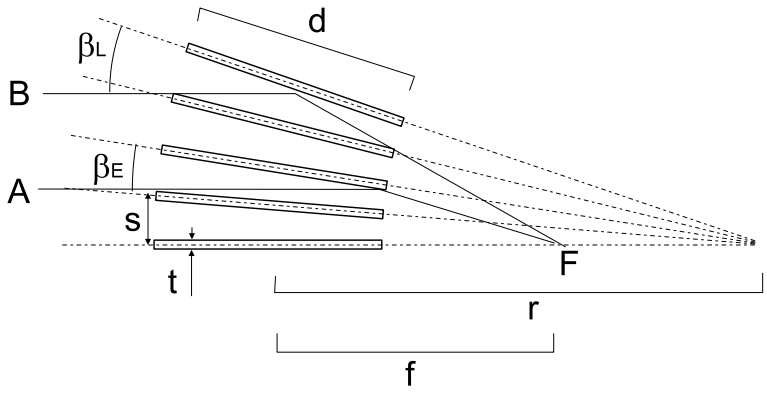


**Figure 4.16:** *A schematic view of the Lobster Eye. Reflecting surfaces are aligned side by side along the cylinder with radius $r$ while the focal spot $F$ is created at $f = r/2$.*

### 4.1.6 Summary

We have designed the soft X–Ray condenser according to the specific experimental requirements. The design and simulations were done using a code that we developed. The optics was then manufactured, using newly developed methods for shaping of a number of mirrors. Finally, the optics was tested in the visible light and in X–Rays. The results have proven the quality of the design and the manufacturing. It also demonstrates the usability of developed code. The condenser is now successfully used and has already been presented in various places [34].

## 4.2 Standard Lobster Eye

### 4.2.1 Motivation

A typical existing X–Ray optics is an axially symmetric and a so called narrow field of view (FOV) instrument. Indirect imaging systems such as the coded mask [35] have been the only way to create a wide FOV X–Ray imaging system for decades. Unfortunately, any indirect imaging system has a substantially worse sensitivity if compared to the focusing instrument.

### 4.2.2 Design

Lobster Eye design based either on the Schmidt [2] or the Angel [1] arrangement is a wide field X–Ray optics. It consists of two orthogonal sets of reflecting surfaces,

each of which focuses in one direction. The profile of such an optics is plotted in Figure 4.16. We can see that the reflecting surfaces are aligned side by side on the cylinder with radius $r$. Parallel beams (rays A and B) are focused onto the cylindrical surface with radius $f = r/2$.

Rays A and B in Figure 4.16 have special meanings for this kind of optics:

**Ray A** reflects from the most distant reflecting surface which can be fully illuminated by rays from the source in infinity on the optical axis. The surface should be optimised to have as good reflectivity as possible around this angle.

**Ray B** is the most distant ray, which can reach the focal spot after one reflection in this one–dimensional case. Any more distant ray will reflect once from the inner side of the mirror and at least once from the outer side of the preceding one. Hence no further mirrors will contribute to the focal spot of the source on the optical axis, because of the limited X–Ray reflectivity.

All rays which are more distant than ray B would be lost because of too large number of reflections which they undergo. Rays between A and B use the LE reflecting surfaces efficiently and there are no rays passing through the system without befing reflected. Rays closer than A illuminate the whole mirrors, however the total front area is quite small and rays can pass through the system without any reflection.

There is a simple rule for initial optics design [36]. For a given photon energy, let us define $\beta_L = \alpha_C$, where $\alpha_C$ is the critical angle for a given energy and surface material and/or quality. The $\beta_L$ is the angle between the incoming ray and the mirror which is illuminated just up to one half of its length (as seen in Figure 4.16). This ensures that all mirrors which can focus into the focal spot because of the geometry really reflect. We can construct the constraints for the LE mirror dimensions:

$$f = r/2 \tag{4.1}$$

$$\beta_L \simeq 2\beta_E \tag{4.2}$$

$$\beta_E = \frac{a-t}{d} \tag{4.3}$$

Additionally, we can use $s - t$ as the first rough estimate for the focal spot size, which gives us the last constraint for the initial design of the Lobster Eye. The design has to be further optimised using the ray–tracing code.

We have developed the model of a Schmidt LE using the above–mentioned conditions and further ray–tracing optimisation for the following input parameters:

- focal length $f = 375$ mm

- angular resolution $< 4$ arc min
- gold–layered mirrors with micro–roughness $\sim 1$ nm
- 100 $\mu$m thick mirrors which is because of the technological limitations
- 300 $\mu$m spacing between mirrors because of the technological limitations

These input parameters were ruled by actual technological limitations (mirror dimensions, layers) and parameters of the instruments for the Lobster-ISS project [24] (focal length and angular resolution).

After some ray–tracing simulations of different mirror lengths and widths across a range of energies $0.5 - 10.0$ keV, we have chosen the final mirror dimensions:

- width $w = 78$ mm
- length $d = 11.5$ mm

The results of simulations of this optics will be discussed in the following sections. Although the simulations were performed for a particular optics, the results are more or less general for any other example of the Standard Lobster LE.

### 4.2.3 Optical Characteristics

#### PSF in General

The Point Spread Function (PSF), or the Optical Transfer Function (OTF), of the Lobster Eye has a specific shape. An example of an on–axis point source is plotted in Figure 4.17.

Generally, it consists of three distinct parts:

**The Central Peak** is the small central spot with the highest intensity. All photons gathered in the central peak are reflected once from the horizontal set of mirrors and once from the vertical set.

**The Cross** is created by photons reflected only once, either from the horizontal mirrors (the horizontal part of the cross) or from the vertical mirrors (the vertical part of the cross). The cross is not solid but "dashed", which is due to the shielding effect of the complementary set of mirrors, i.e. vertical mirrors shield the horizontal cross created by horizontal mirrors, and vice versa.

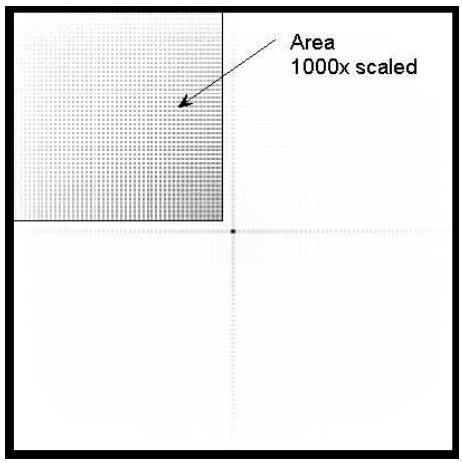


**Figure 4.17:** *The PSF (Point Spread Function) of the on–axis source emitting* 1 *keV photons. The image has* $256 \times 256$ *pixels,* $0.1 \times 0.1$ $mm^2$ *each. The intensity is in sqrt scaling.*

**The Area** is the rest of the detector area without the central peak and the cross. Photons gathered there are mostly those which pass through the optics without any reflection. Hence, a squared pattern would be visible if central peak was not so bright.

We have performed a number of simulations in order to understand the mutual relations of these three parts of the typical PSF. Relative intensities of these three parts are visible in Figure 4.17. Always, the intensity of the central peak is much larger than the intensity in the cross and this is again much larger than intensity in the rest of the image.

With the increasing photon energy, these relative intensities decrease, but the inequalities still hold.

On the other hand, the total numbers of photons gathered in different areas are important for image processing, noise estimations, and quality checks, which will be discussed further in this work.

Detected photon counts inside the three different areas as a function of energy are plotted in Figure 4.18. The counts are normalized to the incoming count rate. We see that the total amount of photons gathered inside the central peak and the cross structure is larger than the amount of photons gathered outside the cross/peak structure for soft X–Rays (below $\simeq$ 2 keV) in this particular LE design. However, the total amount of photons inside the peak is lower than the number of photons inside the cross for all energies. Because the cross has a much larger area if compared to the peak, the peak is much brighter than the cross. The amount of photons outside

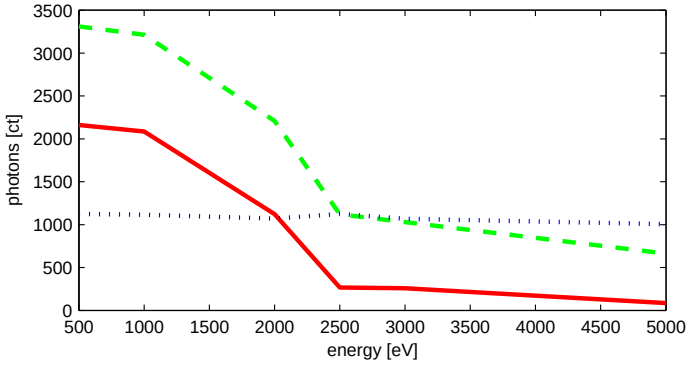


**Figure 4.18:** *The amount of photons gathered inside the central peak (solid line), inside the cross structure without the peak (dashed line), and inside the rest of the detector area (dotted line). It is clearly visible that the amount of photons gathered without any reflection (dotted line) is approximately constant with photon energy, while the amount of photons gathered inside the peak or the cross decreases due to decreasing reflectivity. Please note that the amount of photons gathered inside the cross is always larger than the amount gathered in the peak. However, the peak is located in a much smaller area, hence the intensity is adequately higher. The detector in this example had* $512 \times 512$ *pixels,* $0.1 \times 0.1$ $mm^2$ *each.*

the cross/peak structure is independent on the photon energy. This is natural if we realize that no reflections are taken into account..

In Figure 4.19, the amount of photons in each part of the PSF is normalized to the total amount of photons gathered on the whole detector. We can see, that only $10 - 30\%$ of detected photons are located inside the focal spot and this number is strongly dependent on the photon energy. On the other hand, $40 - 50\%$ of the detected photons belong to the cross, and energy variations are relatively small. This is because only one reflection is incorporated and thus the decrease in reflectivity leads just to the linear intensity decrease, not the quadratic ones as in case of the focal spot. The ratio of photons outside the cross/peak structure raises from 20% to 60% with increasing energy.

Generally speaking, the results of our simulations tell us that for higher photon energies the focus is less bright and the image is more significantly affected by background from the cross and the rest of the image. The precise numbers depends on the energy for which the optics was optimised. Therefore, if we try to built the optics for some particular energy, we can obtain much better results for this energy than those presented in this example.

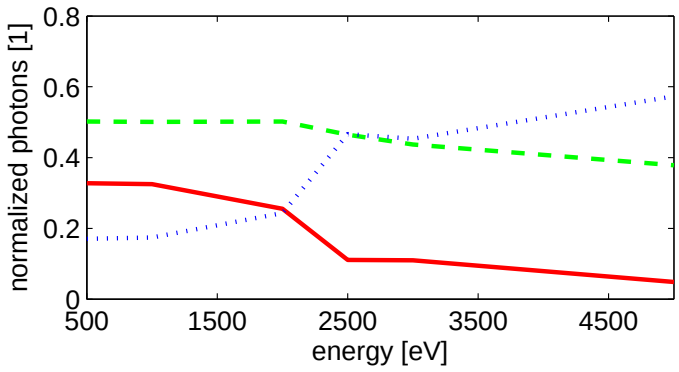


**Figure 4.19:** *The same data as in Figure 4.18, but normalized to the total amount of photons gathered across the whole detector, unlike Figure 4.18, where it is normalized to the amount of photons incoming the front area of the optics). We can see that the number of photons gathered inside the cross (dashed line) is relatively stable, while the number of photons inside the peak (solid line) decreases, as expected. The number of photons in the rest of the detector (dotted line) raises dramatically.*

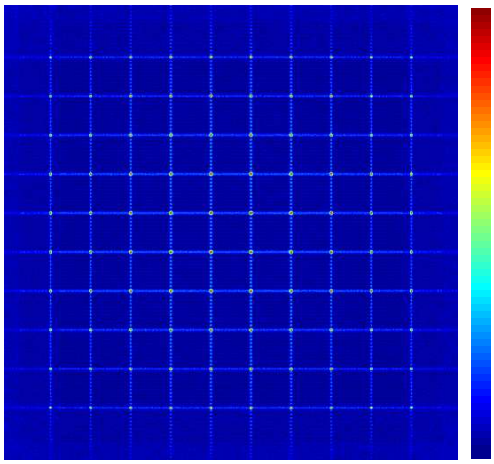

**Figure 4.20:** *Result of* $10 \times 10$ *identical point sources shifted across the FOV. We can see that each point source has its own cross structure and that the relative intensity decreases with the distance from the optical axis. The intensity is in sqrt scaling.*

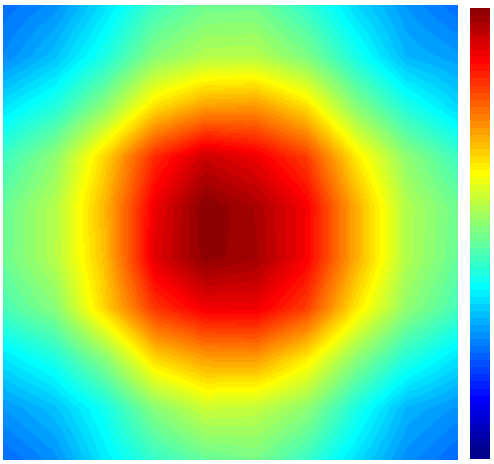

**Figure 4.21:** *Decrease of the relative central peak intensity with the distance from the optical axis. The decrease is given mostly by finite optics dimensions, because only a small part of the optics is active for sources near the edge of the FOV. This image was obtained by processing the data from Figure 4.20.*

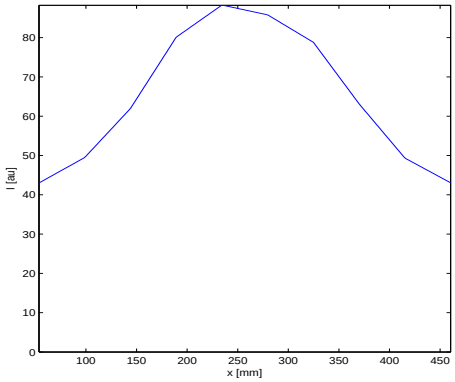


**Figure 4.22:** *The profile of Figure 4.21. We see that the FOV and detector size was chosen correctly, because the source intensity drops to* 1/2 *at the edges of the FOV.*

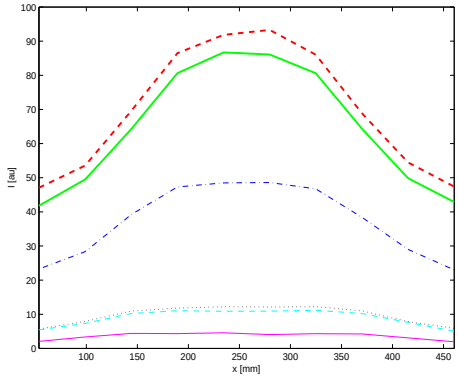


**Figure 4.23:** *The profile of relative change of the source intensity across the detector for different energies. The energies are* 500 *ev (thin solid line),* 1 *keV (thin dashed line),* 2 *keV (thin dotted line),* 2.5 *keV (thin dashed–dotted line),* 3 *keV (thick solid line), and* 5 *keV (thick dashed line).*

### PSF Spatial Variations

As mentioned above, LE is a wide field X–Ray optics. Thus, we have to study the change of the PSF with the changing central peak position relative to the optical axis. The study of such an effect gets its importance especially for astronomical applications of the LE. However, it has not been published so far even by the groups dealing with the astronomical LE [24], although intensive and complicated simulations and tests have already been undertaken.

In principle, LE can be built truly shift invariant. This is possible if the mirrors are arranged onto a sphere and the detector has a spherical shape too. In reality, an asymmetry is present in the optics design and the limitation for the FOV is induced.

We have simulated an array of $10 \times 10$ of identical sources uniformly distributed over the FOV $\sim 6 \times 6$ deg$^2$ and analysed the result. All detected sources together are plotted in Figure 4.20. The sources are distributed uniformly across the detector, as was expected, each having its own cross and central peak. Although it is not clearly visible from Figure 4.20, the shape of the PSF changes slightly with the position on the detector. The peak is in the middle of the cross for sources near the optical axis, while the cross becomes asymmetric for sources further from it.

The asymmetry depends on the overall optics design, but under some extreme, but still realistic and valid, conditions the central peak can be completely outside the cross structure, i.e. the cross bars do not even cross. The reason can be viewed

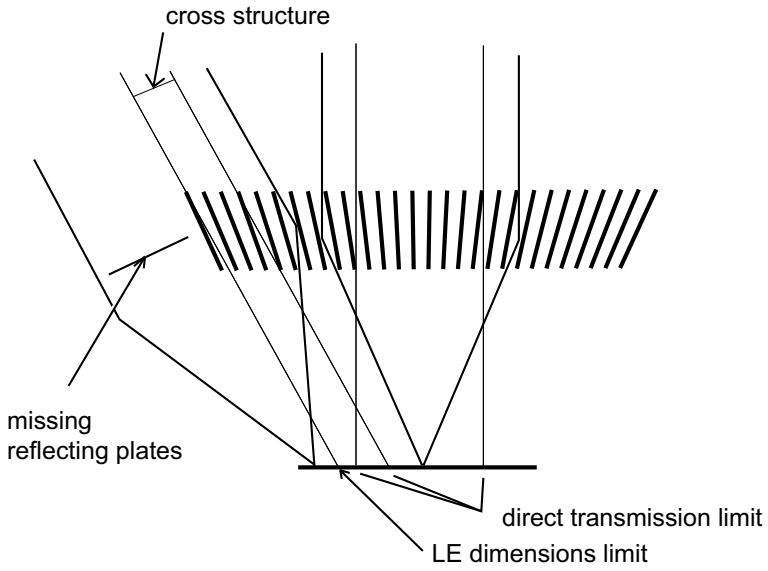


**Figure 4.24:** *A schematic view of the LE for on–axis and off–axis sources. The image introduces the direct transmission limit, which is the largest distance into which the light can pass through the optics without beeing totaly reflected by the complementary set of mirrors. This limit is given by a slight mutual tilt of the mirrors. There is a limit due to the dimensions of the optics as well.*

in Figure 4.24. The length of the cross bar is governed by the complementary mirror set. The light can pass through the system on both sides of the central peak for the source near the optical axis, while in case of the off–axis source we can see that it can be shielded in such a way that the peak is outside the "permitted" bar. These changes have to be taken into account in further image processing attempts. The change of the shape of the central peak is rather small and it is typically smaller than the deformations induced by the manufacturing imperfections.

There is a substantial change of central peak intensity due to vignettation. The simulated intensity map for the detector is plotted in Figure 4.21 and the profile of this simulation is plotted in Figure 4.22. The intensity drops down with the distance from the optical axis to $\sim 1/2$ at the edges of the detector. In fact, this is exactly the reason why we have chosen this detector size. Thus, the detector covers the so called FWHM FOV, i.e. the detector is large enough to cover the area where the central peak intensity is above one half of the maximum.

The change of intensity is given mainly by the finite optics size. Only a few mirrors are active for the sources near the edge of the optics, the rest of the beam, which can be reflected in principle, would be outside the optics, as can be seen in Figure 4.24.

Relative intensities of central peaks in counts per second and the decrease of the in-

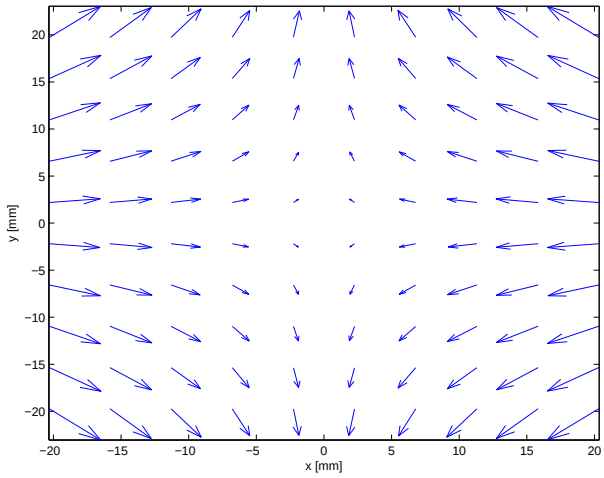


**Figure 4.25:** *Systematic shift between the measured source positions and the true positions. The asymmetry is given by different positions of mirrors reflecting in different directions, relative to the focus. The size of arrows is artificially increased to make them clearly visible.*

tensity with the distance from the optical axis for different energies are plotted in Figure 4.23. The FWHM FOV for higher energies is somewhat larger. This is because the optics was optimised for small energies, hence for larger energies only lower number of mirrors around the line of sight are active and thus the line of sight can be moved further from the optical axis without affecting the number of active mirrors.

### Systematic Position Shift

As mentioned above, the change of the shape of the central peak is rather small and can be neglected in some cases. On the other hand, for certain applications, like the astrometry using X–Ray telescopes, precise quantification of this effect together with other possible effects has to be performed.

In order to quantify the quality of the LE design for astrometry measurements, i.e. the precise measurements of the source positions, we have processed the data obtained from the simulation presented in Figure 4.20. We have measured the positions of each single peak and compared it to the expected ideal ones. We have found a systematic shift plotted in Figure 4.25, which was not reported in any of other LE related papers.

The angular histogram of shift directions is plotted in Figure 4.27. Although the directions are relatively uniformly distributed in the histogram, especially if compared to the Hybrid Lobster Eye (see Section 4.3), the direction of the shift is strongly dependent on the position on the detector. The shift is inward horizontally and out-

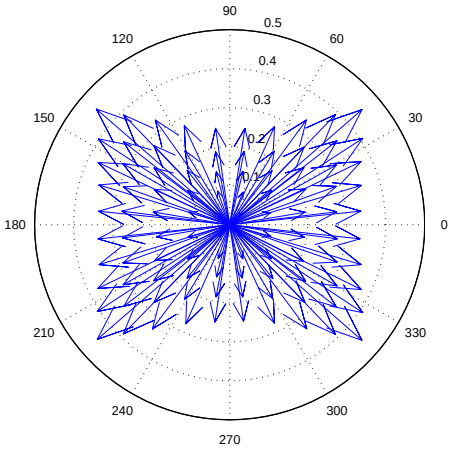


**Figure 4.26:** *Corrections from Figure 4.25 shifted into the center to emphasize the true length of arrows. The radial dimension is in millimeters.*

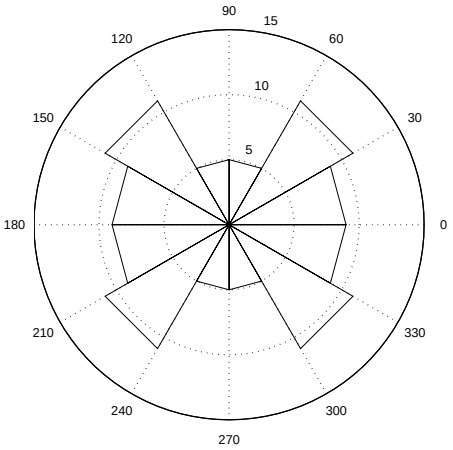


**Figure 4.27:** *Histogram of directions of corrections from Figure 4.25.*

ward vertically. This is because mirrors reflecting horizontally are in different distance from the focal spot than those reflecting vertically. If the mirrors were in the same distance, which is technologically extremely difficult, the shifts would be more symmetric.

True lengths of shift arrows are plotted in Figure 4.26. The lengths are up to 0.4 mm, which is equivalent to 4 pixels. This is enormously high value for astrometry type of observations.

We have also simulated a number of cases with the shift correction applied and performed the same analysis as before. The shift was reduced to a small fraction of a pixel, which is acceptable.

### 4.2.4 Scanning Simulations

#### Simulation & Reconstruction Principle

We have performed a number of scanning simulations, where the optics was virtually attached to an orbiting satellite.

In case of the scanning observations, the optics and the detector hold together while moving around and detecting photons. There are three additional important parameters of the system, specifically the rotational axis, around which the whole system is moving, and the angular speed of rotation, and the angle between the optical

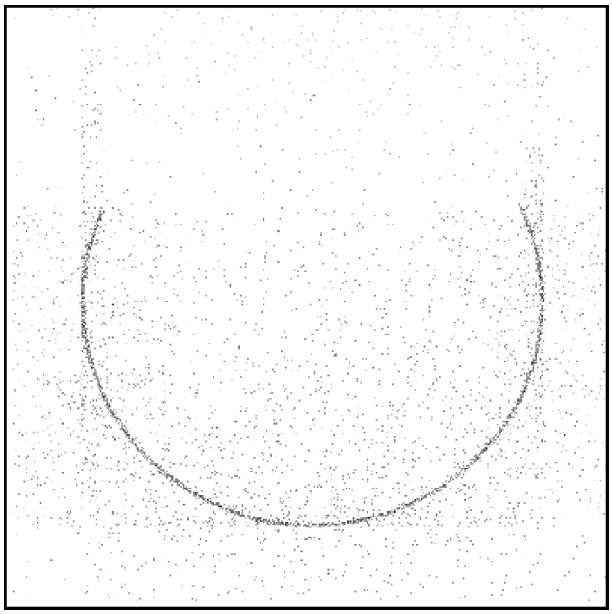

**Figure 4.28:** *An example of a simple long exposition in case of the scanning observation. The rotational axis is parallel to the optical axis, therefore the off–axis source is spread out into an arc. The figure has* $400 \times 400$ *pixels,* $100 \times 100$ $\mu m^2$ *each. The intensity is in sqrt scaling.*

axis and the rotational axis.

If the instrument is used in the same way as in case of pointed observations, we can obtain the results similar to the image plotted in Figure 4.28. In this case, the rotational axis is parallel to the optical axis, and therefore the off–axis source will produce an arc.

Now, our task is to reconstruct Figure 4.28 into the form of a single point–like source. We have done this using several assumptions:

- arrival time of each photon is exactly known — we expect that the detector works as a photon counting device. The arrival time of each photon will be measurable with some precision. Let us suppose that the time can be measured with a precision high enough that the source will move much less than one pixel during the uncertainty interval (a "pixel limit").
- the position of each photon at the detector is known with one pixel precision
- the source does not change during the observation time, from we reconstruct the data
- the orientation of the whole system (optics and detector) relative to the sky

is known at each time with a precision much higher than the "pixel limit"

The process of reconstruction can be split into the following steps:

1. Get a photon position at the detector and an arrival time.
2. Calculate an estimated position in the sky, relative to the optics and the detector reference frame, from which the photon is coming. In order to do that, we have a position at the detector for each incoming photon. However, we can not know, whether the photon belongs to the peak or to the cross of the PSF. In case of the cross, it is almost impossible to calculate the real position of the source, since we do not know which part of the cross is the right one. Hence, to be able to estimate the position at the sky, we will assume that each photon belongs to the peak. We will see the consequences of these assumptions in the following images.
3. Correct the photon position according to shift corrections explained in Figure 4.25.
4. Transform the estimate of the relative sky position into the absolute sky position in a given sky coordinate system. This is the point where we use the knowledge of the relative orientation of the instrument at a given time.
5. Project the photon onto the virtual detector in a desired position.

To emphasize the importance of the step 3 of the mentioned algorithm, which would be missing if no kind of our PSF variations analysis was done, we have reconstructed data from Figure 4.28 according to the mentioned algorithm with the step 3 skipped. The result is plotted in Figure 4.29. The structure of the peak is circle–like and is not suitable for additional processing. We expect the point source to be reconstructed as a single peak with some halo, which originates from the cross of the PSF known from the pointed observations.

The reconstruction is much better if the correction (step 3) is properly applied as can be clearly seen in Figure 4.30. The correction was applied in all our further scanning simulations as a standard and inseparable part of the reconstruction process.

### Detector Time Resolution Influence

As we mentioned above, we need to measure the arrival time of each single photon, i.e. the detector should work as a position–sensitive Photon Counting Device (PCD). Such a detector is often implemented as a fast read–out CCD camera. Photons are detected continuously for a short time (fraction of a second) yet the CCD is read

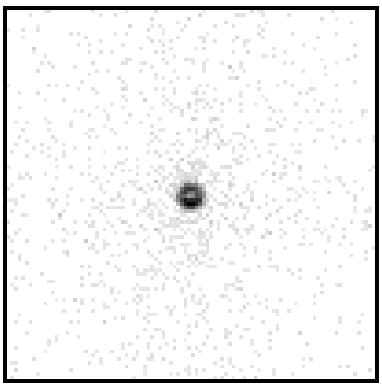

**Figure 4.29:** *An example of reconstruction of the scanning observation from Figure 4.28. A detail of the central peak is visible. Intensities are in sqrt scaling.*

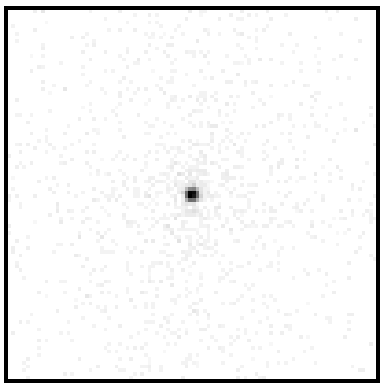

**Figure 4.30:** *The same as Figure 4.28, except that the correction for astrometric shift was applied. The improvement of the peak quality is clearly visible.*

out even faster afterwards ($\sim 100$ $\mu$s). We get a film strip of photon positions with the frame rate similar to the CCD readout frame rate.

The following simulation is done to provide the constraints on the detector time resolution for the realistic All–Sky monitor. Most authors suppose the usage of their favourite and well mastered detector [24, 37], but do not provide the analysis of the true demands on the detector.

We are going to suppose that the time of the photon arrival can not be measured exactly, but only with a limited precision. This is especially the case of photons detected in a fast read–out CCD, where the interval between the read–outs can be typically $0.1 - 1.0$ s. If the photon arrives during this interval, the only thing we can measure is the beginning and the end of the interval. Thus, the arrival time precision will be also $0.1 - 1.0$ s in this case. In our simulation, we have replaced the photon arrival time by the center of the uncertainity interval.

The effect will be naturally the highest when the rotational axis is perpendicular to the optical axis. The optical axis will be moving through the sky at the highest speed in this case, and therefore the uncertainty in the arrival time measurement will result in the largest angular error.

The angle between the optical and rotational axes is 90° for our simulation. The angular velocity of rotation was chosen to match a 90 min orbit, which is the typical orbital period for the Low Earth Orbit (LEO), i.e. $\sim 200 - 400$ km.

The result of the simulation is plotted in Figure 4.31. The leftmost part shows the result for the perfect time resolution. For 0.1 s intervals, the peak is almost

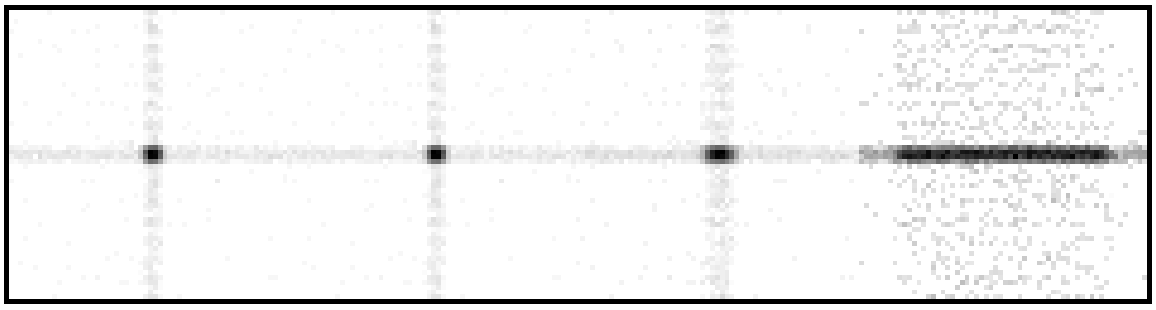

**Figure 4.31:** *Effect of the limited time resolution. Four images with the time resolution* 0.0 *s,* 0.1 *s,* 1.0 *s, and* 10.0 *s (left to right). Each image has* $60 \times 60$ *pixels,* $100 \times 100$ $\mu m^2$ *each. Note that the cross remains almost unchanged for the direction perpendicular to both the optical axis (perpendicular to the paper) and rotational axis (up–down direction). Sqrt intensity scaling.*

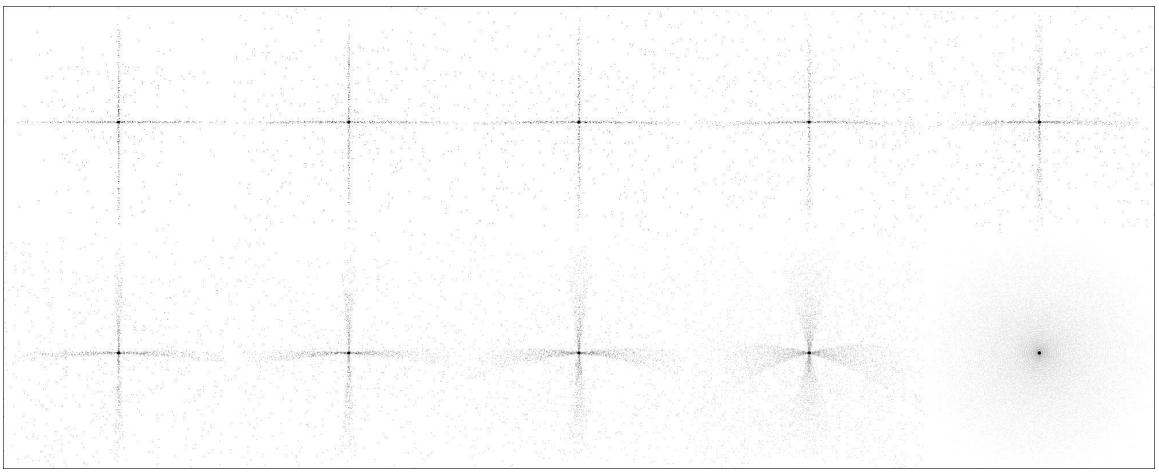

**Figure 4.32:** *Examples of the PSF at different off–orbit distances, all the sources were on–axis. The detecting time was different for each source. It was inside the FOV of the detector for a different time, depending on the off–orbit angle. The off–orbit angles are* 0°, 10°, 20°, 30°, 40°, 50°, 60°, 70°, 80°, 90° *(left top to right bottom). The intensity is in sqrt scaling.*

the same as in case of the perfect time resolution. Some blurring is visible for 1.0 s intervals, yet the system may still produce useful data. On the other hand, in case of 10.0 s intervals, the peak is blurred substantially, and only limited information can be obtained.

### Off–Orbit Distance Influence

Now, the shape of a single PSF is different compared to the pointed observations. Crossing bars may no longer be visible, while a halo around the central peak is often present. This halo is created from the photons of the cross which are transformed into a different position during the rotation. We are not able to distinguish between photons reflected into the peak and into the cross. The exact shape of the PSF is heavily dependent on the angular distance between the orbital plane and the source.

Each PSF has been integrated as long as the source is visible during one revolution in our simulation, in order to reveal the dependence of the PSF shape on the off–orbit distance. This means that the integration time for in–orbit sources will be much smaller than for those at poles of the orbit, where the sources are visible during the whole revolution.

The result of the simulation for on–axis sources is plotted in Figure 4.32. We can see that the typical structure of the PSF consisting of the central peak and the cross holds for in–orbit observations, while the cross is blurred into a halo for observations near the pole of the orbit. The shape for the positions between these two extreme cases resembles the Helvetian cross.

### Influence of the Exposure Time

In our previous simulations, we were gathering as many photons from the source during the revolution as possible. The amount of photons which can be gathered for equally bright sources depends on the off–orbit distance of the source. It is the smallest for sources near the orbit, while it can reach up to the whole orbital period for sources near the pole.

However, there is a possibility that the photons from a source are gathered only for a fraction of the total exposure time. The reasons can be an extreme variability of the source or only a short existence of the source as the most extreme example. This is exactly the case of some astronomical sources, like Gamma Ray Bursts [13], which last from several seconds to several hundred seconds, X–Ray Binaries [38, 39], or SNe [11].

The changes should be observable primarily in the cross structure or the halo around the central peak, because the central peak is always reconstructed into a single peak. The changes will also be visible mainly in larger off–orbit distances, because the blurring of the cross is affected just by the rotation of the instrument. For in–orbit sources, the blurring is negligible, hence the change of the PSF with the fraction of the detecting time is small.

The effect can be at best explained for the sources near the pole of the orbit.

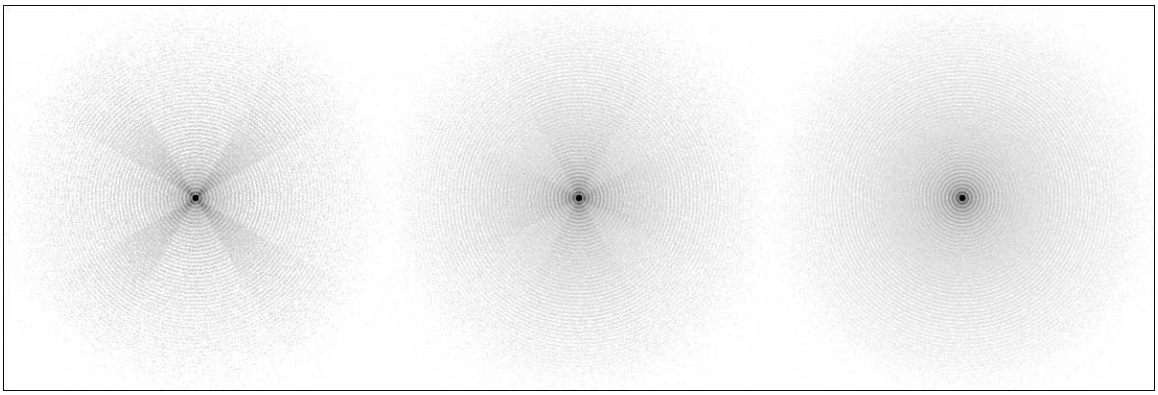

**Figure 4.33:** *Examples of the PSF near the pole of the orbit for three different integration times. The integration times are* 1/3, 2/3, *and* 3/3 *fraction of the orbital period. The intensities are in sqrt scaling, the central peak is artificially overexposed to highlight the surrounding halo.*

We have simulated the source exactly in the pole of the orbit with a 90 min orbital period and with exposure times 1/3, 2/3, and 3/3 of the orbital period. The results are plotted in Figure 4.33. We see that the shape of the halo around the main peak is really dependent on the exposure time. The blurring naturally increases with the exposure time and the Helvetian cross changes into an axially symmetric halo for the exposing time equal to the orbital period.

Hence, if trying to specify the PSF for the image reconstructing methods, we need to know not only the off–orbit distance, but also the overall data gathering time. We can model the proper PSF using such information exactly as presented in Figure 4.33.

Yet, still, the source can be extremely variable even during its existence and the proper PSF can be modeled only if the intensity profile during the observation is known. Unfortunately, to determine the activity time and the intensity profile before the PSF modeling is difficult and can be basically derived from the observations only if the PSF is known. Thus, we have to estimate the total activity time for short sources or use some iterative approach. The first guess for activity time and intensity profile is obtained supposing the PSF for steady source, the output is taken for generating a better estimate of the PSF and the procedure is repeated several times.

### PSFs Over the Detector

We have also simulated a number of PSFs in different positions. The angle between the optical and rotational axes is now $\sim$ 5.7 deg, which gives us relatively large distortions which are better visible. All the PSFs are plotted in Figures 4.34 and 4.35.

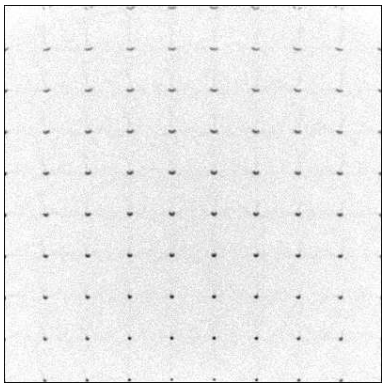

**Figure 4.34:** *An example of a number of PSFs in the scanning mode without the shift correction. The intensity is in sqrt scaling. All sources have an equal true intensity. The angle between optical and rotational axes is* $\sim 5.7$ *deg.*

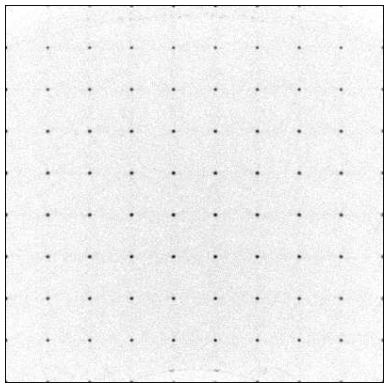

**Figure 4.35:** *The same as Figure 4.34 except that the shift correction has been applied. Much better uniformity of the sources is achieved. All sources have now axially symmetric shape.*

The exposure time is larger than the visibility time of any of the sources.

An importance of the astrometric shift correction is clearly visible in these figures. Much better uniformity of the sources across the detector can be achieved, either in the PSF shape or in the source intensity, which decreases for larger off–axis distances, as expected.

### 4.2.5 Summary

The Standard Lobster Eye seems to be a promising tool especially for the soft X–Ray Scanning All–Sky Monitor. The advantages of the Standard Lobster Eye for this system can be summarized as:

- relatively simple to built
- wide FOV of a single optics
- long integration time during a single orbit compared to the other MFO designs
- sufficient angular resolution is well achievable

Thanks to these properties, we can built a low–cost focusing All–Sky Monitor with a good angular resolution and sensitivity.

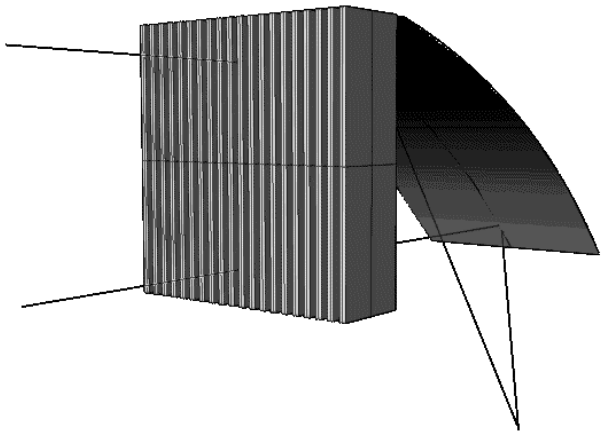

**Figure 4.36:** *The sketch of the Hybrid Lobster Eye wit two plotted rays. Only one parabolic mirror is schematically plotted here. In fact, a number of reflecting surfaces have to be used.*

On the other hand, the Standard Lobster Eye may not be perfectly suited for some laboratory applications, where the finer angular resolution or other specific constraints on the size or the energy response are required. Although it can still be used in principle, some further modifications of the Standard LE discussed in later sections should be considered.

## 4.3 Hybrid Lobster Eye

### 4.3.1 Motivation

The optics described in Section 4.2 is a wide field optics, but it is relatively complicated to achieve a better angular resolution with the given technological limitations of mirror thickness and spacing.

One of possible solutions to this problem is induced by the typical use case of the Standard Lobster Eye as an All Sky Monitor (ASM) for X–Ray astronomy. The Lobster Eye will be used onboard the satellite and will scan the sky. If a certain point of the sky is outside the FOV of the optics at the moment, it will be inside the FOV some time later because of scanning. Hence, in principle, we can accept a smaller FOV in the scanning direction, if we can get some advantage as a tradeoff, such as a better angular resolution. The desired optics would have a wide FOV and moderate angular resolution in one direction, and a smaller FOV and better angular resolution in another one.

We have to use curved mirrors to achieve the better angular resolution with con-

straints on mirror dimensions. There is a relatively simple way to the final idea combining all these facts. A combination of the standard one–dimensional Lobster Eye in one direction and the Kirkpatrick–Baez [22] parabolic mirror set in the other direction would fulfil all the requirements. The idea originally emerged from discussions with Mr. Inneman from Reflex, Ltd., and is further developed and discussed here.

One can imagine that the final optics would be similar to the one plotted in Figure 4.36.

### 4.3.2 Design

To be able to compare this kind of optics to the Standard Lobster Eye, we have chosen analogous requirements on our next design:

- focal length defined as the distance between the focus and the center of the optics $f = 375$ mm
- LE mirror dimensions $78 \times 11.5 \times 0.1$ mm$^3$, with 0.3 mm gap between the surfaces
- thickness of parabolic mirrors $t = 0.3$ mm
- minimal gap between parabolic mirrors $s = 0.5$ mm
- maximal angle of reflection on parabolic mirrors $\theta_{lim} = 23$ mrad
- gold coated mirrors

The Lobster Eye part of this optics is then identical to the standard Lobster Eye presented in Section 4.2 with the only exception that the width of the mirrors is only $w = 32$ mm.

We have designed a number of samples of optics fulfilling the requirements. They differ mainly by the length $d$ of the parabolic mirrors. The proper choice of the length $d$ was given by the simulation plotted in Figure 4.37. We can see that the best results are obtained for short mirror lengths. The off–axis sources are then imaged as the sharpest spots on the detector and are generally the most uniform. In the following simulations and tests we have used the optics with 10 mm long parabolic mirrors.

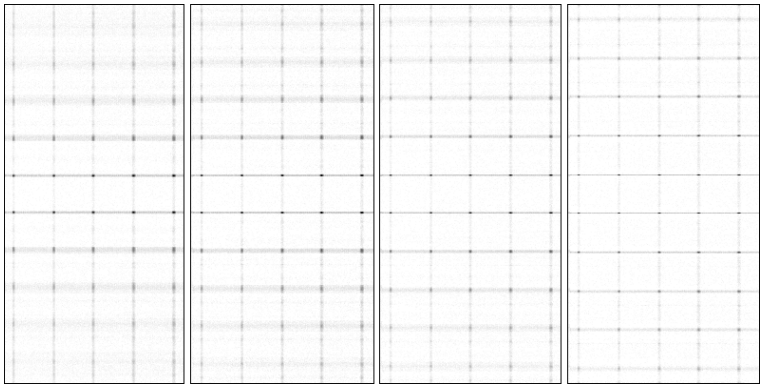

**Figure 4.37:** *Simulation of the array of point sources observed with the Hybrid LE with different parabolic mirror dimensions. The length of the parabolic mirrors is* 40 *mm,* 30 *mm,* 20 *mm, and* 10 *mm, respectively (left to right). Parabolic mirrors focus in the vertical direction. Only a part of the original* $400 \times 400$ *px detector is plotted, namely* $200 \times 400$ *pixels. Each pixel has* $20 \times 100$ $\mu m^2$*. The intensity is in sqrt scaling and each image is scaled separately. Please note that off–axis peaks are significantly blurred for larger mirror lengths. The effect is especially visible at the top row of peaks.*

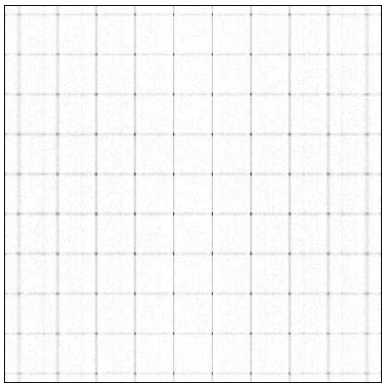

**Figure 4.38:** *A detailed view of the* 10 *mm long parabolic mirror Hybrid Lobster Eye simulation. Dimensions of the detector are* $8 \times 40$ *mm,* $400 \times 400$ *pixels, each pixel has* $20 \times 100$ $\mu m^2$*. All pixels are plotted as squares, although they are rectangular in fact. This makes the details of peaks better visible.*

### 4.3.3 Optical Characteristics

#### PSF in General

First, let us describe the PSF of an on–axis point source. It is similar to the one of the Standard Lobster Eye in vertical direction in our images. On the other hand, parabolic mirrors are optimised to make very small gaps between one another and thus reducing the probability that the photon passes through the optics without being reflected from the parabolic mirrors. Thus, horizontal part of the cross is substantially reduced. The central peak itself has an elliptic shape with the smaller axis in the direction where the beam is focused using the parabolic mirrors. Actually, this is exactly what we wanted to achieve, i.e. better angular resolution in one direction.

However, there is a significant problem with the off–axis sources. We have plotted a more detailed view of the PSF changes across the FOV in Figure 4.38. Although PSFs comply the requirement for the better angular resolution for on–axis sources, they do not do so for off–axis sources. The increase of the PSF FWHM is especially steep with the off–axis distance in the horizontal direction, i.e. in the direction where the parabolic mirrors are working. Initially small axis of the elliptic profile of the central peak becomes soon much larger than the second one if moving away from the optical axis (see Figure 4.43).

#### Central Peak Intensities

We have also simulated the drop of the central peak intensity with the distance from the optical axis. The result is plotted in Figure 4.39.

It is clear from the image that the intensity drops primarily in one direction. The decrease is fast and implies only a 0.6 deg FOV in this direction. It is also evident, that the central peak intensity decreases with increasing photon energy, exactly as in case of the Standard Lobster Eye. The fact can be simply documented in Figure 4.40, where the horizontal sections of Figure 4.39 are plotted.

#### Systematic Position Shift

We have also studied the effect of the systematic position shift of the central peaks in analogy with the Standard Lobster Eye. A set of point sources with known true positions was simulated to get a single image of each source. The positions of the sources were measured by locating the maximum, and refined by averaging using the known window. The measured positions were compared to the true positions and the results are presented in Figure 4.41.

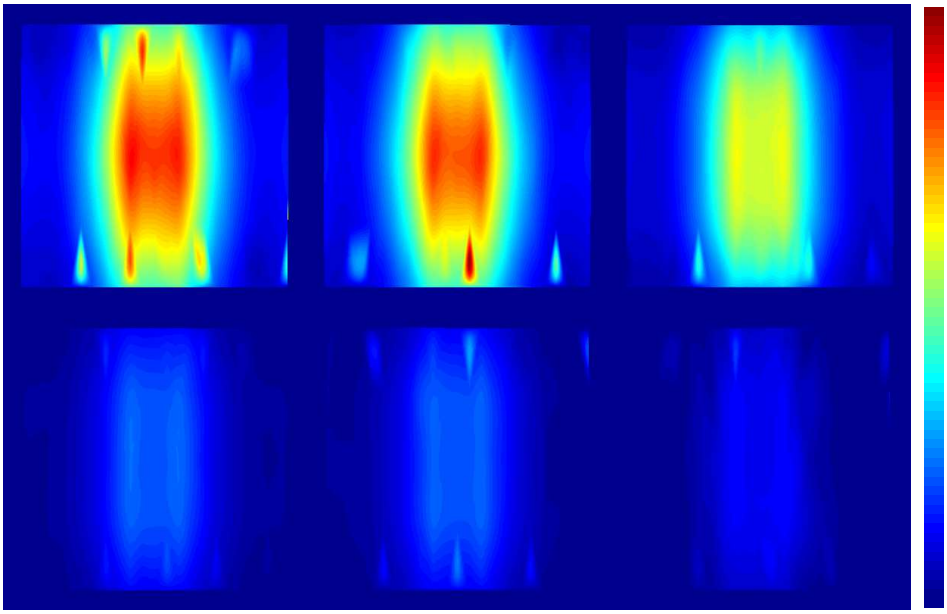

**Figure 4.39:** *The approximation of the central peak intensities across the detector. Images are for* $0.5, 1.0, 2.0, 2.5, 3.0, 5.0$ *keV photons, from top left horizontally to bottom right. Images are* 8 *mm wide and* 40 *mm high. Much more tightness of parabolic mirrors (focusing horizontally) if compared to the Standard LE (focusing vertically) is visible because the intensity falls much faster horizontally. Droplet–like spots of high intensity are just the artifacts of the simulation.*

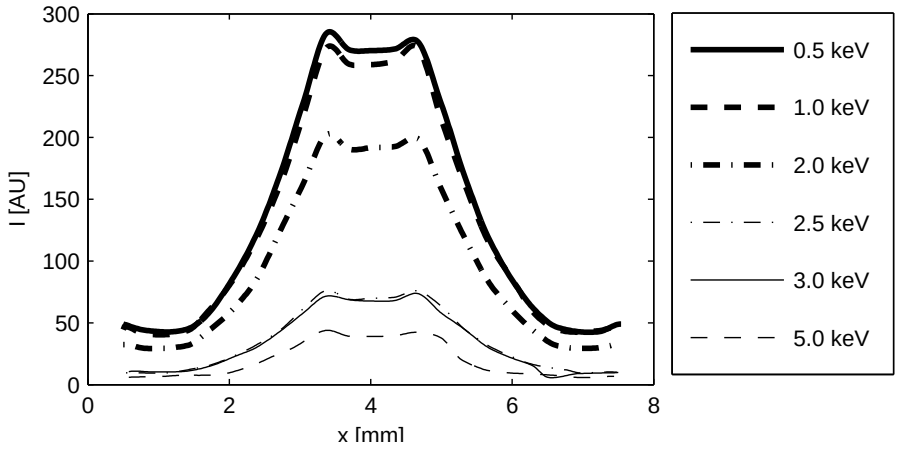


**Figure 4.40:** *Horizontal intensity profile (i.e. in the direction where parabolas focus) for different photon energies:* 0.5 *keV — thick solid line,* 1.0 *keV — thick dashed line,* 2.0 *keV — thick dash–dotted line,* 2.5 *keV — thin dash–dotted line,* 3.0 *keV — thin solid line, and* 5 *keV — thin dashed line.*

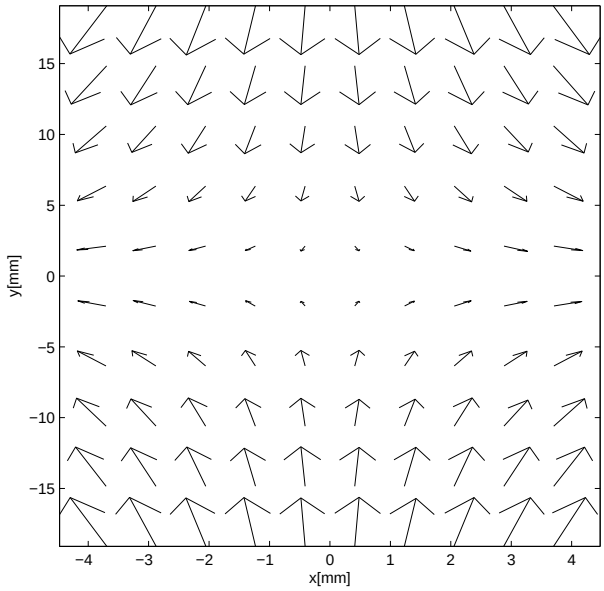


**Figure 4.41:** *The shift of the source position for an array of* $10 \times 10$ *sources. The direction of the shift is prevaling in the direction where the Standard Lobster Eye focuses (see Figure 4.42). This is mainly given by a much larger FOV in this direction.*

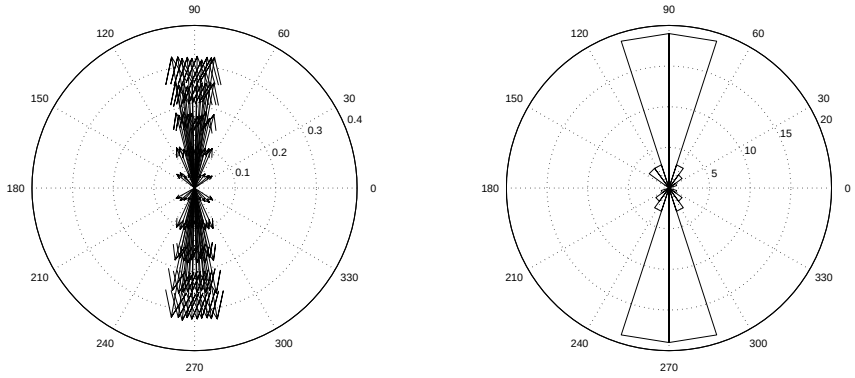


**Figure 4.42:** *True sizes of systematic shifts (left) and shift direction histogram (right)obtained by processing the data plotted in Figure 4.41. The lengths of the shifts on the left image are in millimeters.*

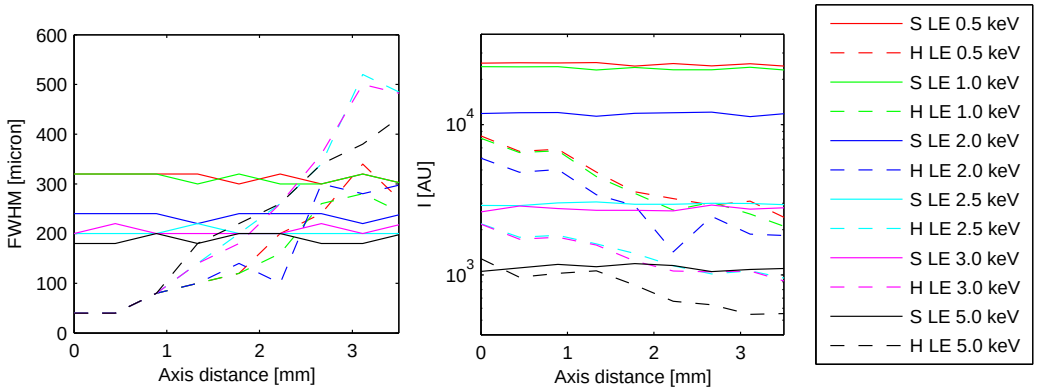


**Figure 4.43:** *Comparison of the central peak FWHM (left image) and the central peak intensities (right image) at different energies for the Standard Lobster Eye (solid line, "S LE" abbreviation) and the Hybrid Lobster eye (dashed line, "H LE" abbreviation). Different colors define different energies:* 0.5 *keV – red,* 1.0 *keV – green,* 2.0 *keV – blue,* 2.5 *keV – cyan,* 3.0 *keV – magenta, and* 5.0 *keV – black. Intensities and central peak FWHM are much more stable for the Standard LE. Central peak intensities are always at least one order of magnitude lower for the Hybrid LE, while for small axis distances the Hybrid LE has a better angular resolution.*

The shift can reach up to $\sim$ 0.3 mm, i.e. 3 pixels, in the vertical direction. In the horizontal direction, it reaches up to $\sim$ 0.05 mm, but because of the smaller pixel size in this direction, it is equal to $\sim$ 3 pixels again.

It is necessary to apply these corrections for further processing of scanning simulations.

### 4.3.4 Comparison with the Standard LE

#### Pointed Observations

The question is whether the Hybrid Lobster Eye really exhibits a substantial increase of its angular resolution if compared to the Standard Lobster Eye, or at least to find out the use cases where it can be efficient.

We have taken our Hybrid Lobster Eye and analogically constructed Standard Lobster Eye and performed the simulation for a number of identical sources. Because the horizontal direction is evidently more restrictive, we have compared the central peaks just in this direction. The results of FWHM peak widths and intensities are plotted in Figure 4.43.

The FWHM peak width and the intensity for the Standard LE is stable at small angular distances from the optical axis, exactly as can be expected from simulations

presented in Section 4.2. Both the FWHM peak width and the intensity of the Hybrid LE change substantially, however.

Let us first discuss the FWHM of the central peak. It is clear that the FWHM of the central peak of the Hybrid LE is 4-6 times better for sources near the optical axis when compared to the Standard LE, but it raises steeply with the distance from the optical axis at all energies. Thus, the FWHM becomes comparable to the Standard LE at $2 - 3$ mm distance from the optical axis for all energies and becomes even larger for larger distances. Hence, the only increase in performance is achieved near the optical axis.

On the other hand, the central peak intensities decrease with energy for both the Standard and the Hybrid LE. The peak intensity for on–axis sources in case of the Hybrid LE is significantly lower. The decrease ranges from several percent up to 70% for higher energies. Moreover, the intensity for the Hybrid LE falls rapidly with the off–axis distance, and the decrease goes down to $\sim$ 90% for low energies and at the edge of the detector. In fact, the difference between those two designs is smaller for higher energies.

### Scanning Observations

Although the comparison of the Standard and the Hybrid LE for pointed observations is important and clear, we need to investigate the properties of the optics in case of the scanning observations, because these were the main reason for designing the Hybrid LE.

We have simulated scanning observations of a single source at different energies for both the Hybrid and the Standard LE. The result is plotted in Figure 4.44. Scanning was simulated on the Low Earth Orbit (LEO) with a revolution period 90 min, and the source was located in the orbital plane. The total exposure time was 60 s before and after the culmination in the sky, i.e. 120 s total.

The detector was large enough to be optimal for the standard LE, but had a pixel size of 5 $\mu$m to be able to compare potentially narrow source images of the Hybrid LE. Hence, the detector had 8000 pixels in the scanning direction.

It is clear from Figure 4.44 that the peak width in the scanning direction is substantially smaller for the Hybrid LE even for the scanning observations. On the contrary, it is also clear that the peak intensity is lower by the order of magnitude in case of the Hybrid LE. The difference in intensity is even larger than in case of the pointed observations.

The explanation is simple. Photons in the peak are gathered during the whole exposure time, thus the position of the central peak moves across the detector. Because

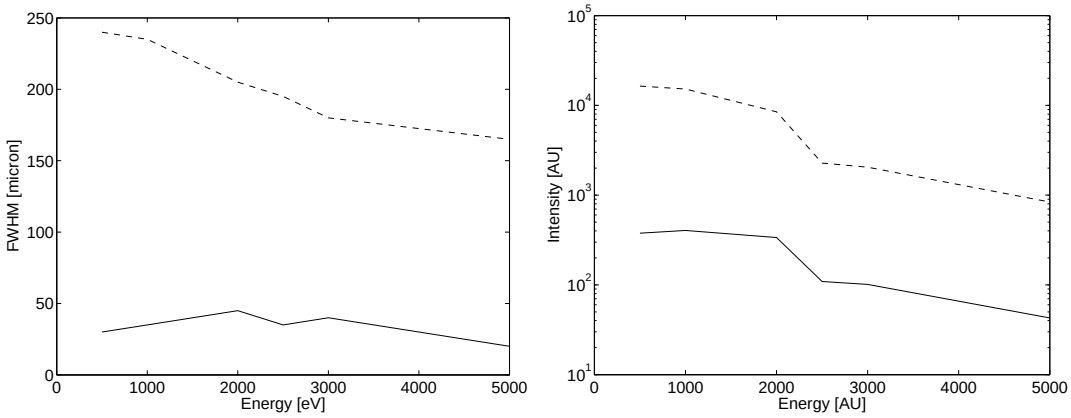


**Figure 4.44:** *Comparison of the simulated FWHM (left) and the intensity dependance on energy (right) for the Standard LE (dashed line) and the Hybrid LE (solid line). The simulation was done for a single source in the plane of the* 90 *min orbit. Total exposition time was* 120 *sec and the shift correction was applied for each of reconstructions.*

the intensity falls rapidly with the distance from the optical axis for the Hybrid LE, most photons are gathered in a short time when the source culminates (near the optical axis). Because of this fact, the peak FWHM remains good, but the intensity falls even faster than in case of the pointed observations. The Standard LE gathers photons for much longer time and the efficiency is relatively stable.

### 4.3.5 Summary

The results of this section show that the Hybrid Lobster Eye can work as intended, i.e. it increases the angular resolution in one direction while still having wide FOV in another. However, the blurring increases rapidly with the off–axis distance in the direction where are focusing the parabolic mirrors. Consequently, it is reasonable to think about such an optics for pointed observations if the source and/or image is expected to be highly asymmetric.

The effect of blurring is reduced for scanning observations, hence the increase in angular resolution is well achievable. But, the decrease of gathered photons resulting in much worse limiting flux is so significant, that, together with manufacturing difficulties, this optics is useless for X–Ray astronomy. The design has already been presented in conferences [40].

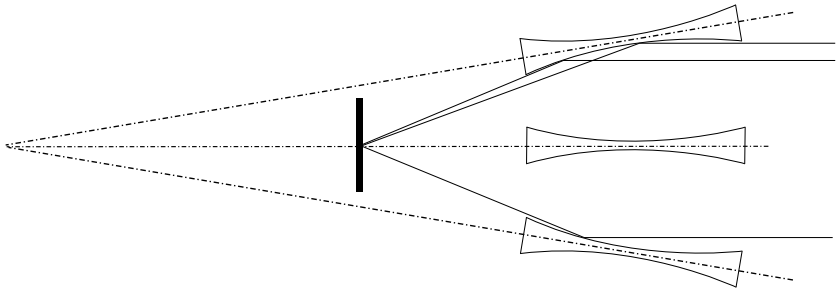

**Figure 4.45:** *A schematic view of the Gently Focusing Lobster Eye. Two parallel rays reflecting from the same surface focus into almost the same point thanks to the shaping of the surface. The optimal shape has to be calculated by optimizing across the whole FOV and the off–axis distances.*

## 4.4 Gently Focusing Lobster Eye

### 4.4.1 Motivation

Although the Hybrid Lobster Eye presented in Section 4.3 exhibits an increase in angular resolution, it has significant drawbacks which are problematic for some applications, such as the astronomical X–Ray All Sky Monitor. In fact, the most severe drawback is the substantial decrease in the central peak intensity emerging from a much smaller FOV in the scanning direction when compared to the Standard Lobster Eye. The source simply remains visible for a shorter time.

The question arises if there is some kind of geometry which improves the angular resolution like the Hybrid Lobster Eye while keeping the wide FOV of the Standard Lobster Eye. The answer is yes, of course. The idea is to shape the reflecting surfaces of the mirrors of the Standard Lobster Eye to force them to focus the rays on their own, not just as a system, and, hence, to enhance the focusing properties of the LE itself. Unfortunately, the shape of surfaces would have to be different for different off–axis distances in order to achieve an ideal focus. But then we encounter similar problems like with the Hybrid Lobster Eye. Instead of that, we have tried to solve the problem by applying the same shape to all mirrors (see Figure 4.45) and optimizing the parameters.

### 4.4.2 Design & Optimization

To be able to compare the design to other Lobster–like designs, we took similar initial conditions:

- focal length $f = 375$ mm

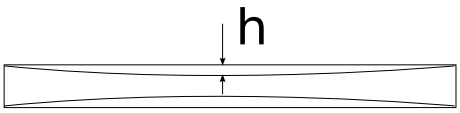


**Figure 4.46:** *A detailed view of a single mirror of the Gently Focusing LE. In our case, the rectangle is* $11.5 \times 0.1$ $mm^2$ *large. We find by the optimization that the radius of curvature of both the upper and the lower reflecting surface is* $\sim 90.8$ $m$*, and thus the maximal difference* $h$ *of the flat and curved surface is* $\sim 0.2$ $\mu m$*. This is well comparable with the natural distortions of the glass itself, as well as the distortions due to the manufacturing process.*

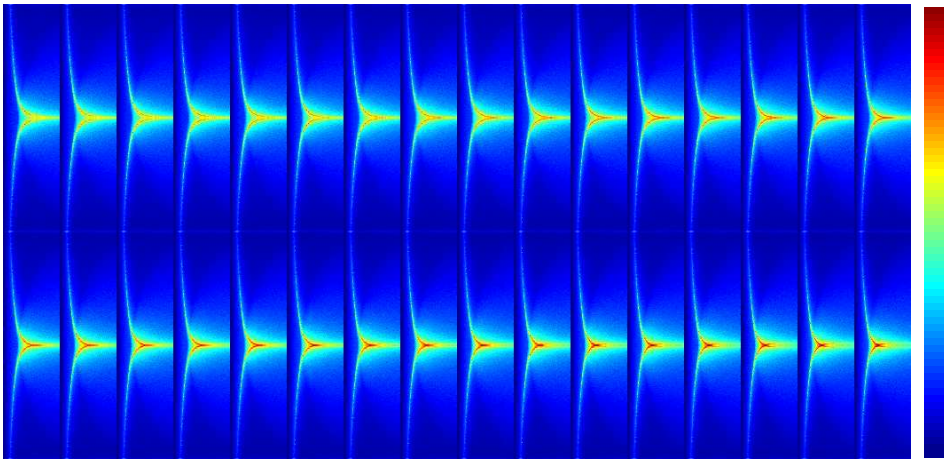

**Figure 4.47:** *An overview of the optimization process. This image consists of 32 distinct images, each for a different curvature radius* $r$*. Each of these 32 images represents intensity image in sqrt scaling. Each column represents a focal spot section. The focal spot radial shift is changing horizontally. Each slice has two distinct peaks for a small focus shift (left side of the image), which are moving closer to each other with the increasing focus shift. The radius curvature varies from* 2 $m$ *to* 100 $m$ *and the focus shift varies from* 0 $\mu m$ *to* 160$\mu m$*. The detector has 256* 1 $\mu m$ *large pixels.*

- base mirror dimensions $78.0 \times 11.5 \times 0.1$ mm$^3$
- mirror spacing 0.3 mm
- gold coated mirrors

Now, there is the task to find the optimal radius of curvature of modified mirrors, as presented in Figure 4.46. In fact, there are two parameters which have to be optimized. First, there is the radius of curvature, as mentioned before. But, second, a tiny shift of the focal surface backward or forward has an important role because of the finite thickness of mirrors and relatively good focusing properties of the slightly shaped mirrors. Small movement of the detector backward or forward results in large blurring of the focal spot, which can destroy the improvement obtained by the shaping.

To make the optimization relatively simple, we will focus on the one–dimensional Lobster Eye at first, i.e. only one of the two orthogonal mirror sets is used.

The optimization itself was done by creating a number of focal spot slices for different radii of curvature $r$ and focal surface shifts $q$. The result is plotted in Figure 4.47. Finding the pixel with the highest intensity value identifies the optimal combination of $r$ and $q$. The photons are collected in the smallest area, hence the intensity is the highest in such a pixel.

Final optimal values for our case are:

- curvature radius $r \simeq 90.8$ m
- focal surface shift $q = 67.5\mu$ m

### 4.4.3 Optical Characteristics

#### One–Dimensional Ideal Case

Let us suppose for a while that the optimized optics can be really built. Therefore we neglect the difficulties with forming of the mirrors into the proper shape as well as the imperfections of the mirrors and the mirror alignment process.

We have performed the simulation of such an optimized and idealized 1D Gently Focusing Lobster Eye and results are plotted in Figure 4.48. Plotted profiles represent the Standard Lobster Eye with the same initial parameters and for the optimized Gently Focusing one. We see an increase of the central peak intensity of the order of 300% as well as a big increase in angular resolution by the factor of $10 - 20\times$.

Because the optics is created by identical mirrors periodically spaced along the cylinder, the same results can be expected across the whole FOV. However, there is an assumption that the detector is appropriately shaped into a cylinder as well. Otherwise, increase in the angular resolution would be diminished by the defocusing for off–axis sources. In fact, the optics would look like the Standard LE for an external observer, because the mirror shaping is small and it is almost invisible at first sight.

Intensity at the edges of the FOV will be decreased as in case of the Standard LE because of finite optics dimensions as described in Section 4.2.

#### Two Dimensional Ideal Case

We tried to make an analogous simulation for a full 2D focusing system as well, where two orthogonal sets of reflecting surfaces were used.

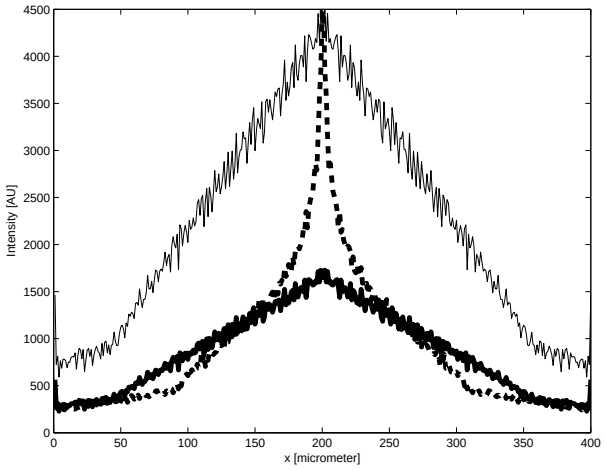


**Figure 4.48:** *Profile of the focus for the one–dimensional Lobster Eye (solid line) and the Gently Focusing LE (dashed line). Thin solid line is the normal Lobster Eye scaled in order to have the same peak height as the Gently Focusing one. Both lobster eyes have the same outer dimensions, yet the Gently Focusing LE has slightly shaped reflecting surfaces with the radius of curvature* $\sim 90$ *m. The classical LE was simulated as the gently focusing LE with the deformation radius* $\sim 10$ *km, i.e. almost flat.*

At first, we decided to utilize the fact, that the optics is relatively shift invariant, i.e. the shape of the central peak does not change substantially across the FOV, as was shown in Section 4.2. Additionally, we only needed to show the probable focal spot appearance. Under these conditions, the focal spot can be simulated as a multiplication of two focus profiles of the 1D Gently Focusing LE in perpendicular directions. The result is plotted in Figure 4.49.

### Two Dimensional Ray–Tracing

We have encountered some numerical problems with our ray–tracing code for the true 3D simulation at first. Handling large numbers (curvature radius, $\sim 10^2$ m) together with small numbers (mirror thickness, $\sim 10^{-4}$ m lead to rounding errors and undesirable effects.

We have slightly modified our ray–tracing code and specified the shape of the Gently Focusing LE more precisely for the fully 3D simulation. Unfortunately, the focal surface shift was found to be different from the already found value $q = 67.5$ $\mu$m for the 1D LE. We used the optimal radius of curvature for all mirrors and tried to find the optimal shift in the 3D case. After a number of iterations we obtained the result plotted in Figure 4.50 for $q = 2.86$ mm.

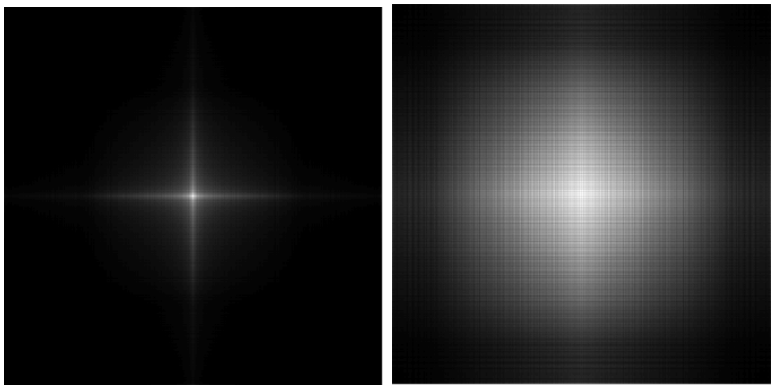

**Figure 4.49:** *An approximation of the focal spot of the optimized 2D Gently Focusing LE (left) and the Classical LE with the same properties (right). The detector is* $400 \times 400$ *pixels large, each pixel having* $1 \times 1$ $\mu m^2$*. The substantial increase in angular resolution in this idealized case is clearly visible. The approximation was obtained as a product of two perpendicular 1D focal spot profiles.*

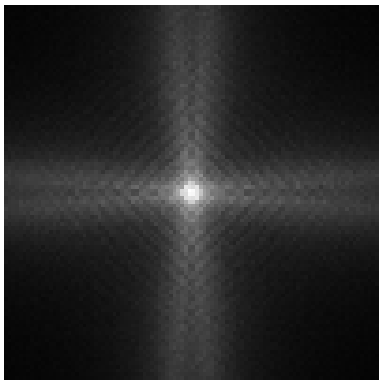

**Figure 4.50:** *The real 3D simulation of the Gently Focusing LE. The image has* $100 \times 100$ *pixels,* $4 \times 4$ $\mu m^2$ *each. Please compare it to Figure 4.49. All images have the same area as the one plotted in this figure.*

The FWHM of the simulated image is substantially worse than in the idealized case displayed in Figure 4.49, but it is still much better than the focusing power of the Standard LE. Thus, the design was proven to be able to achieve better results in the real 2D focusing optics.

Although the shift differs substantially from the 1D version and may be the object of further study, the simulation definitely shows that the concept is feasible even for the full 3D optics. However, further ray–tracing development and adjustment has to be performed to reduce the computational errors even more. Also, a full 3D optimisation technique has to be further developed and enhanced.

### 4.4.4 Manufacturing Challenges

Unfortunately, severe manufacturing problems due to the focusing features of the optics have to be solved. Let us suppose that our mirror is the one in Figure 4.46. The curvature radius of the mirror is $\sim 90$ m. The maximal deviation $h$ of the ideally planar mirror from the ideally shaped mirror can be evaluated to $\sim 0.2$ $\mu$m. However, this value is comparable to the typical natural distortions of the currently used material, i.e. glass.

This means, of course, that ideal conditions will not ever be reached and such a perfect focusing is not feasible. But there is a good chance that even current technologies can produce a Gently Focusing Lobster Eye of larger dimensions, because $h$ raises linearly with optics dimensions.

We can also search for other materials and shaping processes, which may lead to an optics based on the Gently Focusing Optics with properties far from the ideal ones but still substantially better than the standard Lobster Eye.

### 4.4.5 Summary

We have designed and simulated the optics which retains the wide FOV of the Standard LE, while increasing the angular resolution substantially. The design works theoretically very well. It would be especially useful as the All–Sky Monitor for X–Ray astronomy.

Unfortunately, the design needs its mirrors to be shaped in a specific way and, besides, the shape variations are very small. This is a great technological challenge and seems not to be feasible at the moment. Further technological development and new approaches in mirror production and extremely precise shaping are necessary.

## 4.5 Giant Inflatable Lens

We participated in the discussions devoted to creating the next great European X–Ray spectroscopy mission called XEUS [41], which should use a 10 m large X–Ray optics. The manufacturing and design problems with the XEUS mission led us a theoretical work on even the larger space based optics with a more simple design. We have come with a large aperture narrow–field X–Ray optics based on axially symmetric gas–filled rotating cylinder. The system modifies the wave front and focuses, yet at extremely large focal lengths.

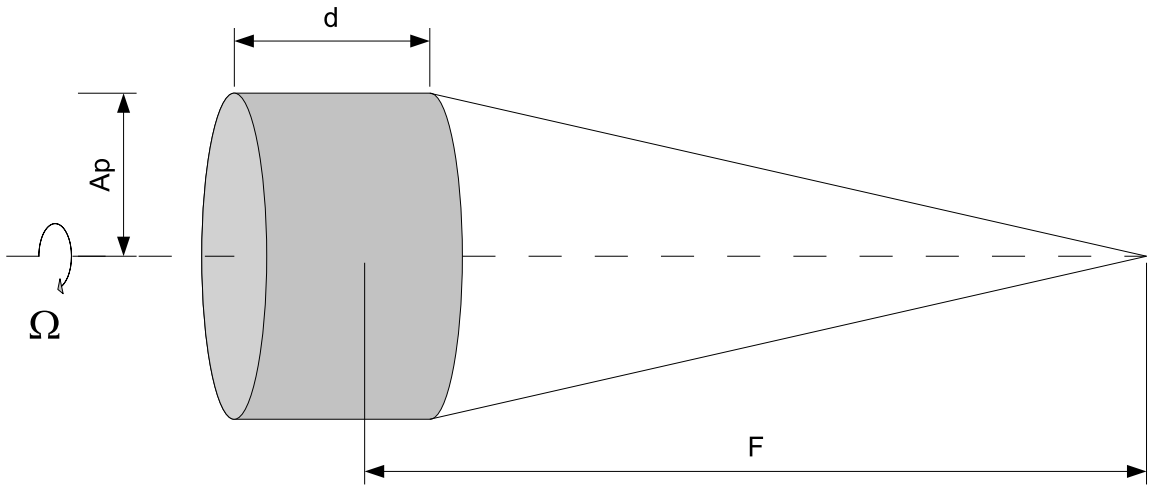


**Figure 4.51:** *A simplified view of the considered gas optics. Large spinning cylinder is filled with gas and focuses X–Rays into a distant focus.*

### 4.5.1 Deriving Equations in Idealized Case

The system looks like the one in Figure 4.51. The cylinder has a diameter $2A_p$, length $d$, rotates at an angular velocity $\Omega$, is filled with the gas with molecular mass $M_A$ (mass of a single molecule) and a temperature $T$. The cylinder has perfectly rigid walls of zero thickness in our idealised case and the gas has the same temperature in the whole volume. No other forces, like the gravity for instance, are present in the model.

In this ideal case, we suppose that the gas is perfectly co–rotating with the cylinder. The equation of motion for a Newtonian liquid is:

$$\frac{\partial \vec{v}}{\partial t} + (\vec{v} \cdot \nabla)\, \vec{v} = -\frac{1}{\rho}\nabla p + \vec{G} \tag{4.4}$$

where $G$ is the volume force density, $p$ is the pressure, $\rho$ is the liquid density and $\vec{v}$ is the speed vector of the liquid. Equation (4.4) can be simplified in the cylindric coordinate system and thanks to the axial symmetry and stationarity:

$$0 = -\frac{1}{\rho(r)}\frac{\partial p(r)}{\partial r} + \Omega^2 r \tag{4.5}$$

To get a consistent set of equations, we need to connect the density and the pressure. The equation in our case of the ideal gas has the very well known form:

$$pV = RNT \tag{4.6}$$

Equations (4.5) and (4.6) together give us the equation for the gas density profile:

$$0 = -\frac{kT\frac{d}{dr}\rho\left(r\right)}{M_{atom}\rho\left(r\right)} + \Omega^2 r \tag{4.7}$$

where $k$ is the Boltzman constant, $T$ is the temperature, $\Omega$ is the angular rotational velocity of the cylinder, and $M_A$ is the mass of a single atom.

The solution to equation (4.7) is:

$$\rho\left(r\right) = C\, e^{\frac{\Omega^2 r^2 M_{atom}}{2kT}} \tag{4.8}$$

Constant $C$ in equation (4.8) can be bounded with the overall amount of gas inside the cylinder:

$$\int_0^R 2\pi r C d e^{\frac{1}{2}\frac{\Omega^2 r^2 M_{atom}}{kT}} dr = M_{gas} \tag{4.9}$$

where $d$ is the length of the cylinder and $M_{\text{gas}}$ is the weight of the gas inside the cylinder. Hence:

$$C = \frac{1}{2}\frac{M_{gas} M_{atom} \Omega^2}{\pi d k T\left(e^{\frac{1}{2}\frac{\Omega^2 A_p^2 M_{atom}}{kT}} - 1\right)} \tag{4.10}$$

The resulting equation for $\rho(r)$ is:

$$\rho\left(r\right) = \frac{1}{2}\frac{M_{gas}\, M_{atom}\, \Omega^2 e^{\frac{\Omega^2 r^2 M_{atom}}{2kT}}}{\pi d k T\left(e^{\frac{1}{2}\frac{\Omega^2 A_p^2 M_{atom}}{kT}} - 1\right)} \tag{4.11}$$

The optical path $s$ through the optics volume changes with $r$ as:

$$s(r) = nd = \left(1 - \frac{1}{4}\frac{M_{gas}\, \Omega^2 r_0 \lambda^2 f_1 e^{\frac{1}{2}\frac{\Omega^2 r^2 M_{atom}}{kT}}}{\pi^2 d k T\left(e^{\frac{1}{2}\frac{\Omega^2 M_{atom}}{kT}} - 1\right)}\right) d \tag{4.12}$$

where $n$ is the refractive index obtained from equation (2.3).

It is important to note here that equation (4.12) can be rewritten into the Taylor series for $r$ in $r = 0$ m up to the second order (after some trivial substitutions):

$$s(r) = 1 - a_1 e^{a_2 r^2} \sim (1 - a_1) + a_1 a_2^2 r^2 + O(r^4) \tag{4.13}$$

which means that the system behaves as a classical lens with a quadratic profile if such a description is valid. The validity will be briefly discussed in Section 4.5.2.

Now we can concretise equation (2.2). In our case:

$$T(r) = e^{-2\,dr_0\,\lambda\,f_2\,\rho_n(r)} \tag{4.14}$$

and because $\rho_n(r) = \frac{\rho(r)}{M_{atom}}$, we can write:

$$T(r) = e^{-2\,\frac{dr_0\,\lambda\,f_2\,\rho(r)}{M_{atom}}} \tag{4.15}$$

### 4.5.2 Fermat Principle Approximation

It is our task now to calculate the estimate for the focal length of such a system. According to the Fermat principle, each ray going from the source into the focal point has the same optical length. We take two rays, the first is identical to the rotational axis and the second is passing through the cylinder at the radius $r$. Additionally, we assume that $r \ll F$ where $F$ is the focal length. Hence:

$$\sqrt{r^2 + F^2} + s(r) = s(0) + F \tag{4.16}$$

$$F\left(1 + \frac{r^2}{2F^2}\right) + s(r) = s(0) + F \tag{4.17}$$

$$\frac{r^2}{2F^2} + s(r) = s(0) \tag{4.18}$$

Solution of (4.12) combined with (4.18) gives us:

$$F = 2\frac{r^2\pi^2 kT\left(e^{\frac{1}{2}\frac{\Omega^2 A_p^2 M_{atom}}{kT}} - 1\right)}{M_{gas}\Omega^2 r_0 \lambda^2 f_1\left(e^{\frac{1}{2}\frac{\Omega^2 r^2 M_{atom}}{kT}} - 1\right)} \tag{4.19}$$

A Taylor series expansion of equation (4.19) can be done if condition $A_p^2 \ll \frac{kT}{\Omega^2 M_{atom}}$ holds. The validity of this condition has to be verified during each step of the Giant Inflatable Lens design process. The second order approximation for the focal length is:

$$F \simeq 2\frac{\pi^2 kT A_p^2}{\Omega^2 M_{gas} r_0 \lambda^2 f_1} \tag{4.20}$$

A simple example for $T = 120$ K, $\Omega = 20$ s$^{-1}$, $R = 20$ m, $M_{\text{gas}} = 80000$ kg, $d = 50$ m, Helium and 10 keV produces $F \simeq 1.17 \times 10^6$ km. This example is just a demonstration. The densities and/or pressure inside the cylinder are extremely large to be realistic, but it shows us the typical dimensions of the focal length, i.e. it is in millions of kilometers.

### 4.5.3 Fourier Approximation

The shape of the focus for the idealized case can be calculated using the Fraunhofer diffraction, however for a more detailed calculation see Section 4.5.4:

$$\psi(X,Y) = \frac{e^{i(\frac{2\pi R}{\lambda}-\Omega t)}}{R} \int\limits_{\text{aperture}} \epsilon(x,y) e^{-2\pi i(xX+yY)} dx\, dy \tag{4.21}$$

We will rewrite the whole integral in cylindrical coordinates $r$, $\theta$, and $z$, because the whole system has to be axially symmetric. Coordinates will be transformed as $[X,Y] \rightarrow [\zeta,\iota]$ and $[x,y] \rightarrow [r,\theta]$. Equation (4.21) becomes:

$$\psi(\zeta,\iota) = \frac{e^{i(\frac{2\pi R}{\lambda}-\Omega t)}}{R} \int_0^{A_p}\int_0^{2\pi} \epsilon(r) e^{\frac{-2\pi i}{\lambda R}(\zeta\cos(\iota) r\cos(\theta)+\zeta\sin(\iota) r\sin(\theta))} r d\theta dr \tag{4.22}$$

Without any loss of generality, we can assume that $\iota = \pi$ and equation (4.22) becomes:

$$\psi(\zeta) = \psi(\zeta,0) = \frac{e^{i(\frac{2\pi R}{\lambda}-\Omega t)}}{R} \int_0^{A_p}\int_0^{2\pi} \epsilon(r) e^{\frac{2\pi i}{\lambda R}(\zeta r\cos(\theta))} r d\theta dr \tag{4.23}$$

Now we can split the angular part from the radial part of the integration:

$$\psi(\zeta) = \frac{e^{i(\frac{2\pi R}{\lambda}-\Omega t)}}{R} \int_0^{A_p} \epsilon(r) r \left( \int_0^{2\pi} e^{\frac{2\pi i}{\lambda R}(\zeta r\cos(\theta))} d\theta \right) dr \tag{4.24}$$

Here the very well known feature of the Bessel functions, especially:

$$J_n(u) = \frac{i^{-n}}{2\pi} \int_0^{2\pi} e^{i(n\nu + u\cos(\nu))} d\nu \tag{4.25}$$

is used and the above equation can be rewritten as:

$$\psi(\zeta) = \frac{e^{i(\frac{2\pi R}{\lambda}-\Omega t)}}{R} \int_0^{A_p} \epsilon(r) r J_0\left(\frac{2\pi r\zeta}{\lambda R}\right) dr \tag{4.26}$$

We are now going to define expression $\epsilon(r)$ as:

$$\epsilon(r) = AT(r) e^{\frac{2\pi i s(r)}{\lambda}} \tag{4.27}$$

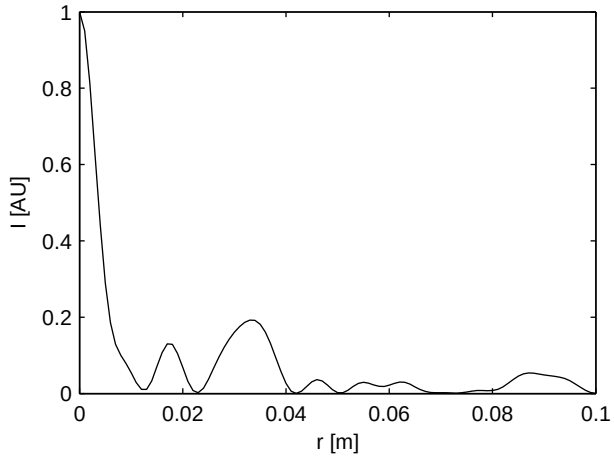


**Figure 4.52:** *The calculated profile of the focal spot based on the Fourier approximation of the idealized case. X–axis represents distance from the optical axis in meters, while Y–axis is in arbitrary units.*

This means that the uniform coherent incoming flux is attenuated inside the optics and phase–shifted according to the actual density value. Here $A$ is an arbitrary constant, $T(r)$ is the transmissivity obtained from the equation (4.15), and $s(r)$ is the optical path through the system obtained from the equation (4.12).

The profile of the focal spot calculated from the Fourier approximation for the simple example from the previous section, where $T = 120$ K, $\Omega = 20$ s$^{-1}$, $A_p = 10$ m, $M_{\mathrm{gas}} = 80000$ kg, $d = 50$ m, Helium is used, 10 keV photons, and $F \simeq 1.17 \times 10^6$ km is plotted in Figure 4.52

The numerical solution of integral (4.26) for the above mentioned parameters can not be done using any of classical numerical integration methods. Because the integrand is rapidly varying, the integration based on numerical solution of differential equations has to be used.

### 4.5.4 Rough Interface Implications

First of severe problems of this theoretical optics is the effect of non-ideal front walls. Let us first discuss a little the effect of wall roughness instead of the wall shape.

#### Fourier Optics

Let us suppose a geometry displayed in Figure 4.51. A planar aperture is at the origin of the coordinate system and is perpendicular to the z axis. An element of the aper-

ture has coordinates $[x, y, 0]$. We would like to calculate the properties of the radiation at the point with coordinates $[X, Y, Z]$, where the distance of the point from the coordinate origin is $R$ and the distance of the aperture element from the observing point is $r$.

The vector of electrical intensity of one particular polarisation on the planar aperture can be described using the complex function $\epsilon(x, y)$. We denote the vector of the observed electrical intensity as $\psi(X, Y)$.

Therefore we can write:

$$\psi(X,Y) = \int\limits_{\text{aperture}} \frac{\epsilon(x,y)}{r} e^{i(kr-\omega t)} dx\ dy \tag{4.28}$$

The term $r$ in the previous equation can be rewritten as (supposing $x^2+y^2 \ll R^2$):

$$r = \sqrt{(x-X)^2 + (y-Y)^2 + Z^2} \simeq R - \frac{xX + yY}{R} \tag{4.29}$$

Substitute for r in exponent using equation (4.29) and $r \simeq R$ in denominator in (4.28):

$$\psi(X,Y) = \int\limits_{\text{aperture}} \frac{\epsilon(x,y)}{R} e^{i(kR - \frac{k}{R}(xX+yY)-\omega t)} dx\ dy \tag{4.30}$$

For further calculations let us suppose the following transform:

$$\begin{aligned} u &= \tfrac{X}{\lambda R} \\ v &= \tfrac{Y}{\lambda R} \\ k &= \tfrac{2\pi}{\lambda} \end{aligned} \tag{4.31}$$

Equation (4.30) can be rewritten as:

$$\psi(u,v) = \frac{e^{i(\frac{2\pi R}{\lambda} - \omega t)}}{R} \int\limits_{\text{aperture}} \epsilon(x,y) e^{-2\pi i(xu+yv)} dx\ dy \tag{4.32}$$

Equation (4.32) is a simple Fourier transform of the function $\epsilon(x, y)$, because it can be simply defined equal to zero outside the aperture. The intensity of the light can be calculated as $|\psi(X, Y)|^2$ then.

$|\epsilon(x, y)|^2$ describes the intensity of the light in a given part of the aperture, while $\arg(\epsilon(x, y))$ describes the phase of the light. If the light is coherent before entering the optical system, then $\arg(\epsilon(x, y))$ describes the phase shift of the light caused by the optical system.

### Effect of the Rough Interface

Let us suppose that:

$$\epsilon(x,y) = A(x,y)e^{2\pi i(W(x,y)+w(x,y))} \tag{4.33}$$

where $A(x,y)$ is a real function describing the intensity of light, $W(x,y)$ describes the systematic phase shift of the light through the optical system as calculated in previous section and $w(x,y)$ describes the random phase shift. We know the probability density $\rho_w(x,y,w)$ for $w(x,y)$.

Additionally, let us suppose that $\rho_w(x,y,w)$ is identical across the whole aperture (hence $\rho_w(x,y,w) = \rho_w(w)$) and averaging $w(x,y)$ across the whole aperture gives us the same result as averaging with the use of the probability density.

Now, we are going to average $\psi(X,Y)$ with respect to $w(x,y)$:

$$\langle\psi(X,Y)\rangle = \left\langle \frac{e^{i(\frac{2\pi R}{\lambda}-\omega t)}}{R} \int\limits_{\text{aperture}} A(x,y)e^{2\pi i(W(x,y)+w(x,y))}e^{-2\pi i(xu+yv)}dx\ dy \right\rangle_{w(x,y)} \tag{4.34}$$

Here we make an important step, where the averaging across the aperture changes into averaging with the use of the probability density:

$$\langle\psi(X,Y)\rangle = \int\limits_{-\infty}^{\infty} \rho_w(w)dw \frac{e^{i(\frac{2\pi R}{\lambda}-\omega t)}}{R} \int\limits_{aperture} A(x,y)e^{2\pi i(W(x,y)+w(x,y))}e^{-2\pi i(xu+yv)}dx\ dy \tag{4.35}$$

Switching the integrals:

$$\langle\psi(X,Y)\rangle = \frac{e^{i(\frac{2\pi R}{\lambda}-\omega t)}}{R} \int\limits_{aperture} A(x,y)e^{2\pi i(W(x,y))}e^{-2\pi i(xu+yv)} \int\limits_{-\infty}^{\infty} \rho_w(w)e^{2\pi iw}dw\ dx\ dy \tag{4.36}$$

Now we have to choose the proper probability density function $\rho_w(w)$. The choice of the normal distribution is a good first guess:

$$\rho_w(w) = \frac{1}{\sigma\sqrt{\pi}}e^{-\frac{w^2}{\sigma^2}} \tag{4.37}$$

$$\langle\psi(X,Y)\rangle = e^{-\sigma^2\pi^2}\frac{e^{i(\frac{2\pi R}{\lambda}-\omega t)}}{R} \int\limits_{aperture} A(x,y)e^{2\pi i(W(x,y))}e^{-2\pi i(xu+yv)}dx\ dy \tag{4.38}$$

Equation (4.38) tells us that the light intensity decreases because of the rough interface by the factor:

$$e^{-2\sigma^2\pi^2} \tag{4.39}$$

if compared to the perfectly smooth surface.

If $w(x, y)$ is due to the rough surface, it is connected to the variations of the surface profile $\delta(x, y)$ as:

$$w(x, y) = \frac{\delta(x, y)n}{\lambda} \tag{4.40}$$

and equation (4.37) has to be rewritten so that $\sigma \rightarrow \frac{\sigma_\delta n}{\lambda}$, supposing $\sigma_\delta$ refers to the normal distribution of surface profile:

$$\rho_w(w) = \frac{\lambda}{\sigma_\delta n\sqrt{\pi}} e^{-\frac{w^2\lambda^2}{\sigma_\delta^2 n^2}} \tag{4.41}$$

Expression (4.39) is rewritten as:

$$e^{-2\frac{\sigma_\delta^2 n^2\pi^2}{\lambda^2}} \tag{4.42}$$

It means that the intensity at the focus should decrease by factor (4.42).

We have also tried to calculate the effect using the Monte–Carlo simulation, but the differences in phase for close points were too large to enable a successful calculation. However, this calculation is exactly what needs to be performed as the next step in order to get the shape as well as the intensity decrease properly.

### 4.5.5 Finite Wall Thickness

The second main problem is that the gas inside the cylinder will have an extremely large pressure if compared to the surrounding vacuum. An example of the pressure profile for the above simulated case is plotted in Figure 4.53. We were trying to calculate the profile of the front wall supposing the ordinary strong material with reasonable thickness.

We have used several simplifications in this first step. First, we have supposed that the material can be described linearly using the Hook law. Second, we have supposed that the shape change is adequately small to have only a small impact on the gas pressure. This assumption is consistent with the fact that the shape changes have to be smaller than the overall optics dimensions. Too large shape changes would destroy the whole optics, anyway.

We have simulated two cases:

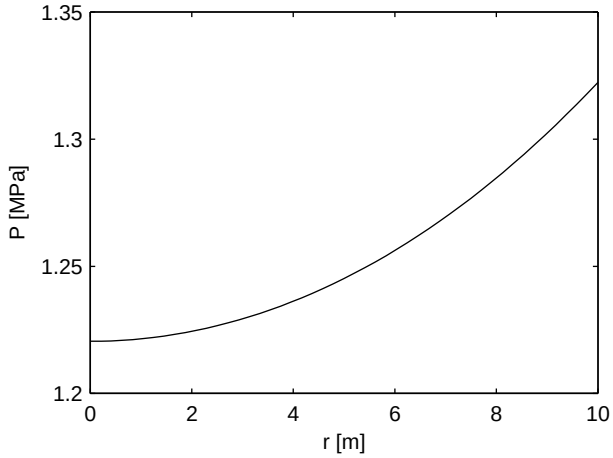


**Figure 4.53:** *An example of the pressure profile inside the rotating cylinder for parameters given in the text.*

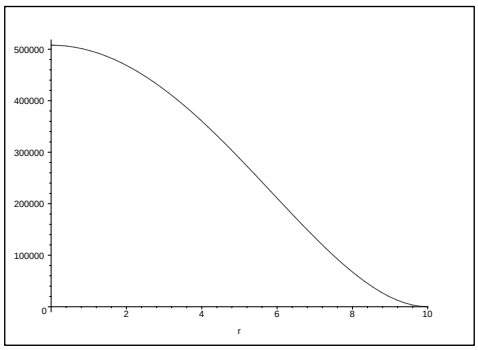


**Figure 4.54:** *The profile of the front wall attached to the cylinder at the circumference with the tangent perpendicular to the optical axis. All axes are in meters.*

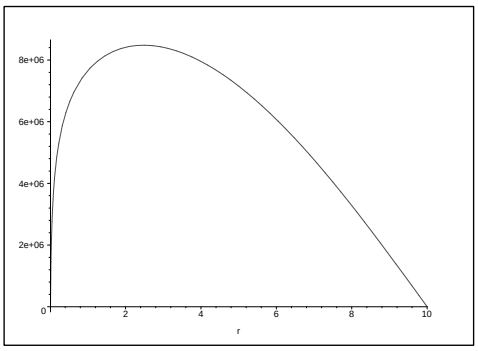


**Figure 4.55:** *The profile of the front wall attached to the cylinder at the circumference and in the centre and no other condition. All axes are in meters.*

- the front wall is attached to the cylinder only at the circumference
- the front wall is attached to the cylinder at the circumference and in the center

We have calculated both approaches for the optics parameters given in the preceding sections and for 1 mm thick wall made of a steel, i.e.:

**Young modulus:** $E \simeq 241$ GPa

**Poisson's ratio:** $\nu \simeq 0.9$

The calculation was based on the linear deformation theory [42] and the results are plotted in Figure 4.54 and Figure 4.55. Unfortunately, the calculated deformation is far beyond the linearity conditions as seen from the images. Moreover, the magnitude of deformation is even much larger in case of the better attachment. This is because of a slightly different attachment at the circumference and mainly due to the extremely large deformation where the laws used for the computation do not hold anymore.

The problem can be solved in several ways:

**Materials with larger Young modulus:** Other materials with a larger value of the Young modulus should be used, however, there are only a few materials with Young modulus larger then the currently used even only several times, not by several orders of magnitude, as is required.

**Thicker wall:** Thicker walls can be used, the wall would be much simpler to build and hold, but much more radiation would be absorbed in the walls, even more than in the whole volume of the gas. The problem of absorption is reduced for higher photon energies, because the transmissivity increases.

**Lowering the pressure:** We can lower the pressure by making the optics longer, while keeping the amount of the gas inside. This is really a working approach, unfortunately, the total weight of the optics is enlarged because of the larger cylinder.

**More complicated attachment:** We can imagine the wall attachment system holding the wall not only of the circumference and in the center, but at a number of points across the surface.

### 4.5.6 Use Case

The potential targets of the optics are ruled by its properties:

- extremely high angular resolution at the order of $10^{-3}$ mas, which is an increase by the order of $10^6$ if compared to current X–Ray telescopes
- extremely large focal length, at the order of $10^9$ m
- extremely large lens speed, hence only the bright sources can be observed
- extremely small FOV, the exact size is dependent mainly on the detector size because of the extremely large focal length

The properties imply that the optics has to be separated into two distinct spacecrafts, exactly as in case of the XEUS [41] mission. However, the distance is much larger and pointing the telescope onto any kind of the source is extremely difficult. It is impossible to move the telescope operatively as the demands arise because of the variability of the X–Ray sky. Instead of that, the telescope would be focused onto already very well known sources in a predefined observation program. The program will be ruled by the changes of relative spacecraft position during their revolution periods. It is impossible to have the system at the Earth orbit because of the focal length. It has to be placed onto the orbit around the Sun instead, into some of the Lagrangian points [8], for instance.

The other problem would be the exact positioning of the optics because of the extremely small FOV. Positions of current X–Ray sources are known with the precision of a fraction of an arc second, at best. This value is much larger than any feasible FOV of this kind of optics. Moreover, we can not move the detector and/or optics from point to point to search the whole error box, the ratio between the current error boxes and the FOV is simply too large. Hence, the position has to be refined by some other supporting instruments, either in the X–Ray band, in the Visible band, or in Radio wavelengths, where the fine angular resolution is currently achieved using the interferometry. This supposes that the sources are also visible in such wavelengths.

Thus, the optics can be used for an in-depth study of spatially small, yet extremely luminous, X–Ray sources like the X–Ray Binaries or the Active Galactic Nuclei. Such sources have the advantage of relatively well known positions with the possibility of refining them with other methods and they are extremely bright for long periods of optics pointing, even though the variability is also high. These sources are very interesting because the spatially resolving measurements of the very surrounding of the Black Holes and Neutron Stars can be performed for the first time.

### 4.5.7 Summary

The optics can be a theoretic alternative to the currently studied X–Ray interferometry missions [43], because it has a similar angular resolution, yet a much larger effective area. The design is more robust for optics technological misalignments and imperfections.

The idea of the optics seems to be feasible, yet further computation of the effect of the rough surface have to be undertaken. The material and/or construction of the optics walls has to be also further investigated.

# Chapter 5

# Image Restoration

## 5.1 Restoration Basics

### 5.1.1 Imaging Systems

#### Basic Imaging System Description

An imaging system, like a telescope, a camera, a microscope, or even a simple human eye, can be often described by the very well known formula:

$$I(x,y) = (O(a,b) * P(a,b))\,(x,y) + N(x,y) \tag{5.1}$$

where $I(x,y)$ are the detected data, $O(a,b)$ is the true image as would be detected under ideal conditions, $P(a,b)$ is the Point Spread Function, which characterises the imaging instrument, and $N(x,y)$ is the additive noise.

Equation (5.1) describes a Linear Shift Invariant Imaging system with additive noise. It means that:

1. if the original source is $\alpha\times$ brighter, the detected image is also $\alpha\times$ brighter
2. if the source at position A produces the detected image at position A', then the same source moved to position B produces exactly the same image, but shifted to position B', with no intensity and/or shape change
3. the noise distribution of the detected image is independent of the detected intensity

In fact, this equation can be derived from the wave optics principles supposing that incoming radiation is incoherent. For more details on coherent radiation at optical systems please read [44].

The non–linearity of the imaging system comes mostly from the non–linearity of the detector used in the imaging system. First, most detectors have lower intensity thresholds, below which no signal is detected, and upper intensity limits, above which all signals are treated as almost the same regardless on the true intensity. Second, the dependence of the signal (typically the current) on the intensity between the upper and lower intensity limits is linear only as the first approximation. A comprehensive review of the upper and/or the lower limits and the linearity considerations for a number of detectors can be found in [45]. The effect of optics used in the imaging system can often be neglected, as long as the non–linear optics [46] can be ruled out.

Unlike in the Linearity case, the Shift Invariance is strongly dependent on the optics used in the imaging system, while the detector properties are much less important. A whole bunch of optical aberrations affecting the PSF is described in any optics textbook. Some of them are important for classical optics using lenses or normal incidence mirrors, some of them are more important for grazing incidence mirrors as in case of the X–Ray optics.

For typical images, the noise can be considered as independent of the measured intensity. This is the case of the Gaussian noise, for example, which is dominantly present in optical measurements. On the other hand, in case of X–Ray astronomical images, where the number of detected photons is much lower, the noise is rather Poissonian. Hence, the noise is not independent on detected intensity. The standard error (RMS) raises as $\sim \sqrt{n}$, where $n$ is the number of detected photons.

### Advanced Imaging System Description

Equation (5.1) can be simply rewritten into the integral form:

$$I(x,y) = \int_{a,b} O(a,b)P(x-a,y-b)da\ db + N(x,y) \tag{5.2}$$

To handle the shift changes and non–linearity, we have to rewrite equation (5.3) as:

$$I(x,y) = \int_{a,b} O(a,b)P(a,b,x-a,y-b)da\ db + N(x,y) \tag{5.3}$$

where the integration kernel $P$ is now dependent not only on the difference of the new and old coordinates, but it is a general function of new and old coordinates. The kernel describes the correct intensity and/or the shape of the PSF which has the center shifted into the position $x, y$. The source intensity at coordinates $a, b$ is scattered across the detector just proportionally to the correctly shifted PSF.

The noise treatment depends on the particular method for image restoration as will be discussed further.

### 5.1.2 Image Restoration Problem

Let us first suppose that we have an imaging system which can be described by equation (5.1). The task is to get the best estimate of the original image $O$ based on the knowledge of the detected image $I$, the Point Spread Function $P$, and perhaps some information about the noise $N$.

If no noise is present, equation (5.1) leads to:

$$O = F^{-1}\left[\frac{F[I]}{F[P]}\right] \tag{5.4}$$

where $F$ denotes the Fourier transform. Unfortunately, this is an absolutely unrealistic case, this simply never happens. In fact, the noise is the most important thing in Image Restoration process.

In general, equation (5.1) is often an ill–posed problem, which means that there is no unique solution to the problem.

The most general way how to understand the problem is to use the Bayesian approach [47]. The general concept of Bayesian approach is as following: Let $f$ be the ideal image, as would be observed under ideal conditions, and $g$ is the really observed image. The inference about the true $f$ is based on the probability of the true image to be $f$ supposing we measure $g$, i.e. $P(f|g)$:

$$P(f|g) = \frac{P(g|f)P(f)}{P(g)} \propto P(g|f)P(f) \tag{5.5}$$

In order to evaluate equation (5.5), we need to calculate $P(f)$ and $P(g|f)$.

$P(f)$ is the "prior" information about the observed scene, the probability distribution of the original image. In other words, it tells us how probable is the particular $f$ from a given set of all possible true images. This is where we incorporate the knowledge of what we are looking at. A number of already developed restoration techniques vary only in the choose of the particular $P(f)$. Lucy–Richardson deconvolution, for example, can be obtained if the $P(f) = const$, which means that all possible manifestations of the true image are equally probable.

$P(g|f)$ gives us the probability of measuring the image $g$ supposing that $f$ is the correct one. This term is strongly affected by the noise. Depending on the expected noise distribution, the $f - g$ can have a Gaussian distribution, or $g$ can have a Poissonian distribution with the mean $f$, for instance. Any other distribution is possible depending on the nature of the detected image and/or phenomenon.

An example of a particular method emerging from equation (5.5) is to find the model which maximizes it, i.e. minimize the $-\log P(g|f) - \log P(f)$. The first term gives

a measure of the likelihood of the image $g$ and the model $f$, while the second term gives the regularization condition. The second term can be expressed in analogy with the statistical physics as $P(f) \propto -\alpha U(f)$ where $U(f)$ is the overall energy of the model. So, in this example called MAP (maximum a posteriori), we maximize the likelihood of the model while trying to keep the energy of the image sufficiently low.

We are going to describe several promising deconvolution techniques, namely the Lucy–Richardson method together with its wavelet modification, and the CLEAN method and its wavelet form. On the other hand, we are going to neglect some other promising methods, like the Maximum Entropy Method (MEM), because they do not fit our typical measurements. The MEM does not preserve the flux, for example, thus it is relatively useless for astronomy.

## 5.2 Multiresolution

### 5.2.1 Multiresolution Principles

The Multiresolution Image Analysis [48] in general is a way of decomposing the image into several "scales" and treating each scale separately.

The decomposition into scales is similar to decomposing the image by several band–pass filters. Therefore large and slowly changing objects are caught in different scales if compared to fast changing and small objects. However, the exact mathematical definition is different. An example is schematically plotted in Figure 5.1.

The multiresolution analysis is based on the wavelet transform, or on the Discrete Wavelet Transform in case of the discrete image data. Mathematically rigorous definitions and explanations of the wavelet transform can be found in [49].

For the basic explanation, let us first suppose that we have a continuous 1D signal $f(x)$. The continuous wavelet transform (CWT) of the signal $f(x)$ is defined as $W(a,b)$:

$$W(a,b) = \frac{1}{\sqrt{a}} \int_{-\infty}^{+\infty} f(x)\psi^* \left( \frac{x-b}{a} \right) dx \tag{5.6}$$

where $\psi^*$ is the analysing wavelet, $a$ is the scale parameter and $b$ is the position parameter.

The inverse transform is:

$$f(x) = \frac{1}{C_\chi} \int_0^{+\infty} \int_{-\infty}^{+\infty} \frac{1}{\sqrt{a}} W(a,b)\chi \left( \frac{x-b}{a} \right) \frac{da\ db}{a^2} \tag{5.7}$$

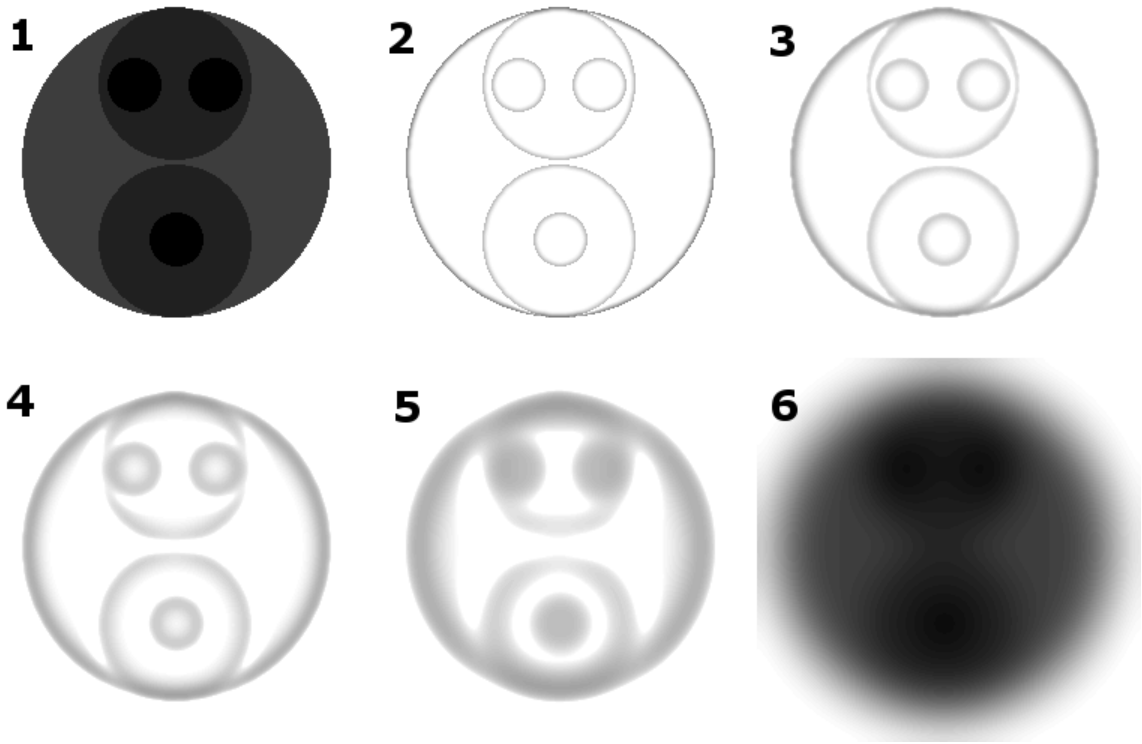


**Figure 5.1:** *An example of a multiresolution decomposition of image 1. The image is iteratively filtered by a low pass filter and the difference between the previous iteration and the current image is plotted (images 2–5). Image 6 is the most smoothed image, a residuum. The sum of images 2–6 gives back image 1. Small objects, i.e. spatially fast changes of intensity, are detected in small resolutions, like these plotted in images 2 or 3. We can see that they are the sharpest ones. On the other hand, extended objects are detected in other resolutions, like these plotted in images 4 or 5, or even in the smoothed residuum.*

where:

$$C_\chi = \int_0^{+\infty} \frac{\hat{\psi}^*(\nu)\hat{\chi}(\nu)}{\nu} d\nu \tag{5.8}$$

where $\hat{\psi}^*(\nu)$ and $\hat{\chi}(\nu)$ stand for the Fourier transform. Generally, $\psi = \chi$, but other choices are also possible.

The CWT have the following properties:

- linearity, i.e. $f(x) = \alpha g(x) + \beta h(x) \longrightarrow W_f(a,b) = \alpha W_g(a,b) + \beta W_h(a,b)$
- covariance with respect to translation, i.e.
  $f_0(x) = f(x - x_0) \longrightarrow W_{f_0}(a,b) = W_f(a, b - x_0)$

- covariance with respect to dilation, i.e.
  $f_s(x) = f(sx) \longrightarrow W_{f_s}(a,b) = \frac{1}{s^{1/2}} W_f(sa, sb)$

The wavelet function $\psi$ is chosen to comply with the preceding properties. There exist a lot of possible wavelet functions, each with a different shape and particular properties.

The Discrete Wavelet Transform has to be used in case of discrete signals, such as a sampled 1D signal or a bitmap image. We need to set $a = 2^j$ in equation (5.6), where $j$ is the level of decomposition. We will construct a ladder of approximation spaces from the function $f(x)$:

$$\cdots \subset V_3 \subset V_2 \subset V_1 \subset V_0 \ldots \tag{5.9}$$

such that if $f(x) \in V_j$ then $f(2x) \in V_{j+1}$. Function $f(x)$ is projected onto the $V_j$ in each of decomposition steps. The projection is defined by coefficients $c_j(k)$ given as scalar products of the function with the dilated and translated scaling function $\phi$:

$$c_j(k) = \left\langle f(x), 2^{-j}\phi(2^{-j}x - k) \right\rangle \tag{5.10}$$

The scaling function has to comply with:

$$\frac{1}{2}\phi(\frac{x}{2}) = \sum_n h(n)\phi(x-n) \tag{5.11}$$

where $h(n)$ is some progression. Equation (5.10) can be rewritten as

$$c_{j+1}(k) = \sum_n h(n-2k)c_j(n) \tag{5.12}$$

After the decomposition, $c_j$ holds more and more smoothed image with increasing $j$. We are often interested only in the remaining information after each step, which can be obtained from the orthogonal subspace $W_{j+1}$ of $V_{j+1}$ in $V_j$. Hence we define a discrete wavelet coefficient:

$$w_{j+1}(k) = c_j(k) - c^*_{j+1}(k) \tag{5.13}$$

Equation (5.13) defines a wavelet function $\psi$, which can be connected with the scaling function using:

$$\frac{1}{2}\psi(\frac{x}{2}) = \sum_n h(n)\phi(x-n) \tag{5.14}$$

In other words, DWT consists of iterative low–pass filtering of the input image, while the DWT coefficients are the difference between two successive iterations.

A given scaling function is connected with a particular wavelet function and with a particular low–pass filter. We need only the low–pass filter for the calculations at most cases. The DWT coefficients are then calculated as the differences between the image and the smoothed version of the image.

Because the image is smoothed in each step, it is possible to decrease the number of samples after each iteration without loss of information. This process is called decimation.

### 5.2.2 À-Trous Wavelet

An example of the so called À-Trous wavelet decomposition into 4 scales and the residual smoothed image is plotted in Figure 5.1. This kind of a wavelet is relatively simple and is often used for the image processing in Astronomy. It is not suitable for image compression, because the decomposition uses no decimation. Coefficients $c_j$ and $w_j$ are derived:

$$c_j(k) = \sum_l h(l) c_{j-1}(k + 2^{j-1} l) \tag{5.15}$$

$$w_j(k) = \sum_l g(l) c_{j-1}(k + 2^{j-1} l) \tag{5.16}$$

The Cubic Spline is often used as the scaling function:

$$\phi(x) = \frac{1}{12} \left( |x-2|^3 - 4|x-1|^3 + 6|x|^3 - 4|x+1|^3 + |x+2|^3 \right) \tag{5.17}$$

The corresponding low–pass filter is $h(l) = [1/16\ 1/4\ 3/8\ 1/4\ 1/16]$. Please note that the actual low–pass filter is zero padded to make distance between two nonzero elements $2^{j-1}$ according to (5.15). The corresponding wavelet function $\psi$ is plotted in Figure 5.2.

The restoration of the original image is then simple:

$$c_0(k) = c_{n_p}(k) + \sum_{j=1}^{n_p} w_j(k) \tag{5.18}$$

In other words, it is simply the sum of all wavelet coefficients at a given position and the smoothed residuum.

### 5.2.3 Multiresolution Support

The process of removing the noise while preserving the significant data is the key objective in most of the processing methods.

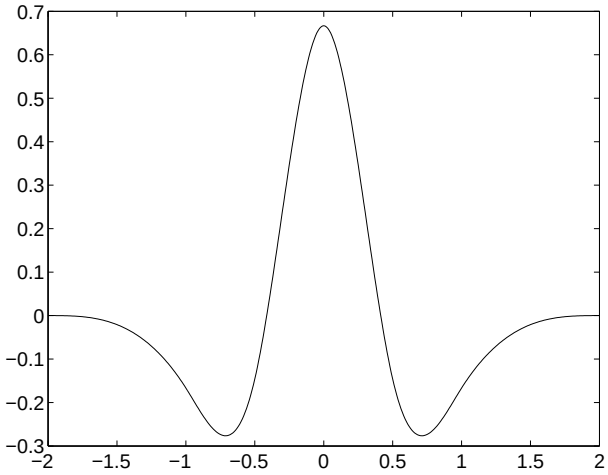


**Figure 5.2:** *The wavelet function $\psi$ corresponding to the À-Trous wavelet based on the cubic spline scaling function (5.17).*

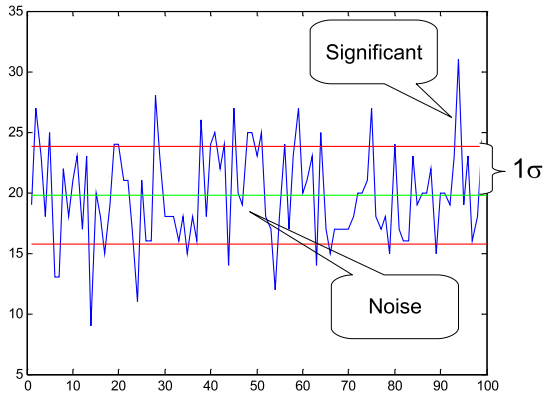


**Figure 5.3:** *An example of data with the Gaussian noise with the average value* 20 *(green line) and* 1 $\sigma$ *(*95 %*) thresholds (red lines).*

Removing noise from the noisy data in a classical way can be seen in Figure 5.3. The noise is expected to have a Gaussian distribution. Hence, we calculate the parameters of the Gaussian distribution and any data between the given sigma threshold (1 $\sigma$, for example) are treated as to be due to the noise, and we can neglect them, and the other ones are significant values.

Similarly, for different distribution and a given probability, we can construct analogical thresholds between which the values of the wavelet coefficients are found if they

are due to the noise.

Hence, we can define the support $s_{i,j}$ for data $d_{i,j}$ with the mean equal to 0 as:

$$s_{i,j} = \begin{cases} 0 & \text{value at i,j is due to noise} \\ 1 & \text{value at i,j is significant} \end{cases} \tag{5.19}$$

Now, the product $d_{i,j}s_{i,j}$ is the "image" consisting only from significant data, all other data are set to zero. Hence, such a product is a "denoised" image, supposing that the image has a zero mean.

The natural question is how to define or calculate such a support in case of the image decomposed by any of the wavelet transforms into several resolutions. It means, if we know the expected noise distribution, how to define the thresholds in each of the resolutions? The process is described in [48] and the resulting support is called the Multiresolution Support. Methods how to calculate the Multiresolution Support in case of the Gaussian Noise, the Poissonian Noise with a large number of photons, and the Poissonian Noise with a low number of detected photons are described there. These techniques were used to create the Multiresolution Support in all of the Multiresolution based image processing methods discussed later.

Briefly, for each resolution and for wavelet coefficient position in the resolution plane the Multiresolution Support specifies whether the coefficient is due to significant data or just due to the noise. Therefore, if $r$ is the resolution index, $i$ and $j$ are coordinates in the given resolution plane, and $w^r_{i,j}$ are the wavelet coefficients in given resolution plane, the Multiresolution Support can be defined as:

$$s^r_{i,j} = \begin{cases} 0 & w^r_{i,j} \text{ is due to the noise} \\ 1 & w^r_{i,j} \text{ is due to significant data} \end{cases} \tag{5.20}$$

The thresholds for the Gaussian distribution and a given confidence level can be calculated using the following algorithm:

1. generate an array with size $\sim 1024 \times 1024$ pixels and values according to the Gaussian distribution with a zero mean and $\sigma = 1$
2. decompose the array into a number of resolutions using exactly the same wavelet as for further image processing
3. calculate the dispersion at each resolution and thus obtain a set of $\sigma_j$
4. for a given image, estimate the noise dispersion of the original image $\sigma_{\text{orig}}$
5. thresholds at a given scale for a given image are $\pm\sigma_j\sigma_{\text{orig}}$

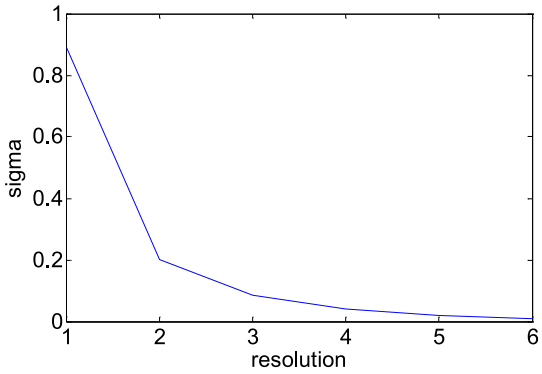


**Figure 5.4:** *An example of the noise dispersion propagation into multiple resolutions. The data were obtained supposing that the original image has a dispersion* $\sigma = 1$.

An example of $\sigma_j$ across the resolutions for the À-Trous wavelet is plotted in Figure 5.4.

The noise is not independent on the incoming flux for low fluxes, where the Poissonian distribution has to be used. In fact, the thresholds for the decision whether a wavelet coefficient is due to the noise or due to a significant structure depend not only on the particular wavelet used for image decomposition, but also on the amount of photons inside the given wavelet support.

In order to calculate the thresholds more universally, we will threshold not the wavelet coefficients themselves, but rather the transformed values:

$$w_j^r(x,y) = \frac{w_j(x,y)}{\sqrt{n}\sigma_\psi} 4^j \tag{5.21}$$

where $w_j(x,y)$ is the actual wavelet coefficient, $n$ is the number of photons inside the support of the wavelet at position $(x,y)$ and scale $j$, and $\sigma_\psi$ is the standard deviation of the wavelet function $\psi$.

Now, if $w_j^r$ is due to the noise, i.e. created by random photons, it should be a random value with the probability density $H_n$, which depends on the number of photons inside the wavelet support. $H_n$ can be calculated as:

$$H_n = \underbrace{H * H * \cdots * H}_{n\times} \tag{5.22}$$

where $*$ denotes the convolution and $H$ is the distribution function of the wavelet function.

We can construct the thresholds for given significance level $\alpha$ (e.g. $\alpha = 95\%$), exactly as in case of the Gaussian distribution. The result of such a calculation,

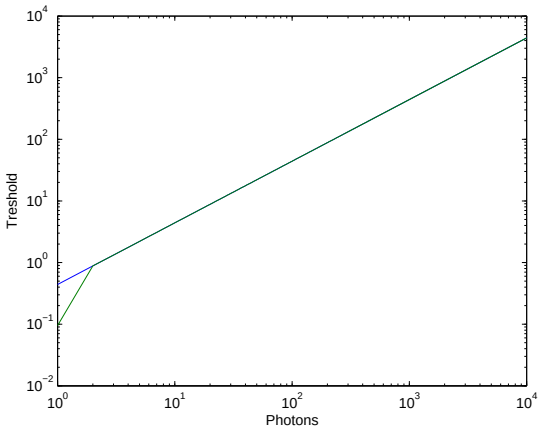


**Figure 5.5:** *Basic Wavelet thresholds for Poissonian distribution, À-Trous wavelet, and significance level $\alpha = 0.95$ %. The plot represents the absolute value of the negative threshold (blue line) and the positive threshold (green line). Thresholds for a given number of photons detected inside the wavelet coefficient support have to be further processed according to the given resolution index.*

which is done in advance and stored in a table for any further computation with a given wavelet and $\alpha$, is plotted in Figure 5.5.

## 5.3 Lucy–Richardson

### 5.3.1 Algorithm

Lucy–Richardson algorithm is an iterative reconstruction method. An imaging system has to be described by equation (5.1) in order to work correctly, i.e. the system is linear and shift invariant with additive noise. At each step, equation (5.1) implies $I^{(n)}(x,y) = (P * O^{(n)})(x,y)$. $O^{(n)}$ is the n-th estimate of the true image. Let us define the residuum:

$$R^{(n)}(x,y) = I(x,y) - I^{(n)}(x,y) \tag{5.23}$$

Lucy–Richardson iterations are [48]:

$$O^{(n+1)}(x,y) = O^{(n)}(x,y)\left[\frac{I^{(n)}(x,y) + R^{(n)}(x,y)}{I^{(n)}(x,y)} * P(-x,-y)\right] \tag{5.24}$$

In fact, the residuum $R$ should be filtered after each step to preserve only the significant structures. We can use any of the standard techniques to obtain the Standard

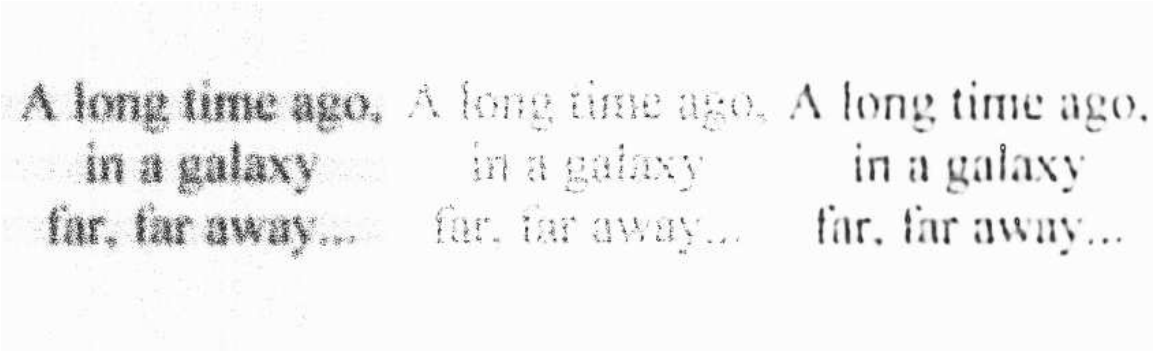


**Figure 5.6:** *An example of ray–tracing of the non–astronomical artificial source in infinity. We use the astronomical LE mentioned in Section 4.2 with the pixel size of* $50 \times 50\ \mu m^2$*. Result of the ray–tracing is on the left. It was processed using the standard Lucy–Richardson method with an automatic noise estimation and no threshold deviation of the result from the image. The result after 20 iterations is in the middle. The result after 20 iterations of the Multiresolution version of the Lucy–Richardson method with automatic noise estimation is plotted on the right image. The simulation is performed relatively deep inside the FOV of the optics, hence we can assume that the system is shift invariant.*

Lucy–Richardson, or we can use filtering based on the Multiresolution Support to obtain the Multiresolution version of the method.

Although we can deal with low photon fluxes, where the intensity obeys the Poissonian distribution, the residuum $R$ is generally an array of real values, hence we have to use the Gaussian Distribution. We have used the $3\sigma$ criterion for the automatic creation of the Multiresolution Support.

### 5.3.2 Non–Astronomical Sources

We have modified our ray–tracing code to handle sources of any shape and arbitrary intensity variations in order to verify the efficiency of various image restoration methods. In fact, the source of any shape has to be placed into infinity, because we would like to be able to compare various method and/or source combinations in case of the Standard astronomical Lobster Eye.

An example of a simulation representing the text across the sky is plotted in Figure 5.6. The simulation was performed deep inside the FOV of the optics, the source edges were relatively far from the FOV edges. Thus, the decrease of intensity and PSF shape changes can be neglected in this particular case. We have chosen the text because it has perfectly defined and complex boundaries and people have a great experience in recognizing it even if it is substantially damaged.

The simulation was done using a relatively small number of photons to make the noise crucial for the image. The noise can be well approximated by the Poissonian distribution. This is exactly the case of low–luminous astronomical X–Ray sources, where the number of photons is small and a long exposure time is often needed.

The simulated measurement was then processed using the Standard and the Multiresolution version of the Lucy–Richardson method. The results are also plotted in Figure 5.6.

In the Standard LR method, which is presented in the figure, we have performed no damping which is often applied when the deviation of the result from the image exceeds some threshold. But the result is similar to the case where the threshold level is equal to $3\times$ the standard deviation of the noise. We have simulated both of these versions.

In the Multiresolution LR method, the significance structures, i.e. the Multiresolution Support, were detected using $3\sigma$ clipping and supposing that wavelet coefficients of the residuum have the Gaussian distribution.

It is clear that the image is substantially enhanced in both the Standard and the Multiresolution case. The letter shape is better recognizable and the background is suppressed. But a more close review of the results show that the Multiresolution LR exhibits a better intensity uniformity and a better edge conservation. The result of the Standard LR is a little fluffy. We have also asked a number of people which of the two reconstructed texts is better readable. All of them answered that the right one, i.e. the Multiresolution one.

We need to verify that the better uniformity and the edge conservation of the Multiresolution LR is retained also for more extended sources, where the uniformity is more crucial point. Thus, we have simulated extended sources and reconstructed them using both methods. The result is plotted in Figure 5.7. The original source consisted of several uniformly bright circles. Indeed, the result after the Standard LR method shows a low intensity uniformity if compared to the Multiresolution LR method. This is especially visible in the largest circle and three smaller circles. The edge of the largest circle is also very fluffy, it is more like the fractal edge instead of being smooth as the original.

Sources in both preceding examples were relatively small if compared to the optics FOV. We would like to show an effect of a PSF intensity and/or shape change near the FOV edges. Thus, we have created a source in the form of a large grid, which was almost as large as the FOV of the imaging system, and performed the ray–tracing simulation and the LR deconvolution of the result. The simulation as well as the deconvolutions are plotted in Figure 5.8.

The decrease of the intensity towards the edges of the image is clearly visible

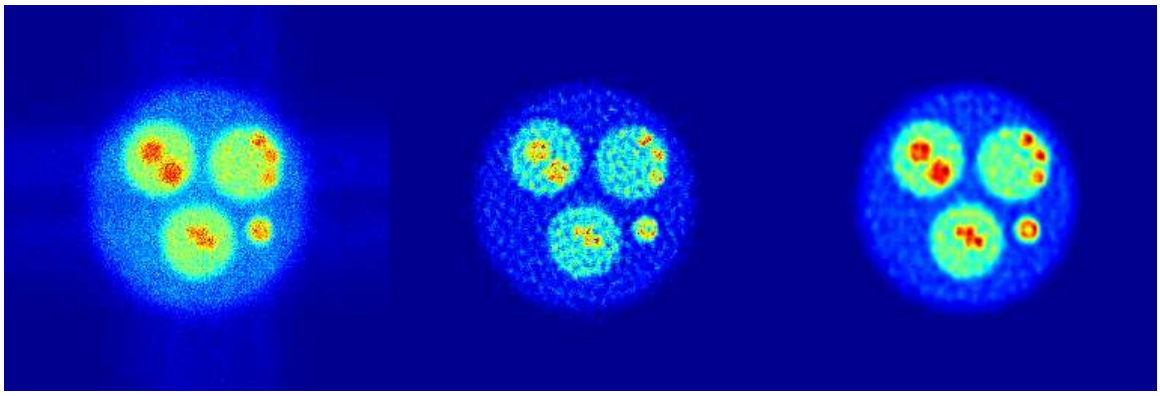

**Figure 5.7:** *The simulation identical to the one presented in Figure 5.6, except that this simulation was intended to test the abilities to reconstruct extended flat sources. Although the noise is intensity dependent (Poissonian) in both cases, it is clear that the Standard LR method produces a kind of fluffy image if dealing with this degree of noise. On the other hand, the Wavelet based LR works significantly better, objects are better delimited and also the homogeneity of originally flat object is better.*

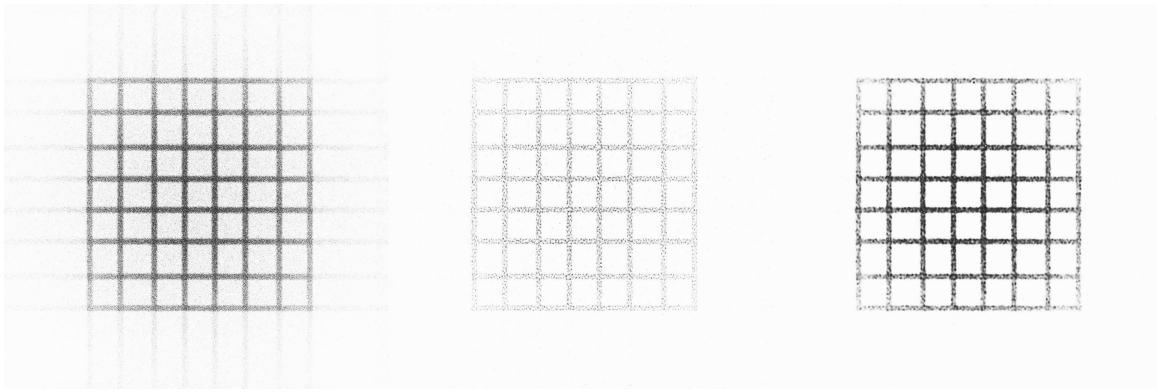

**Figure 5.8:** *This image of ray–tracing (left), the Wavelet based LR (right), and the Standard LR deconvolution (middle) was made to verify the effect of the low shift invariance of the Lobster Eye optics. The source was scaled to be as large as* $\sim 6 \times 6$ *deg*$^2$*, i.e. the FOV of the imaging system. The decrease of intensity with the off–axis distance is present. This decrease is preserved in both the Standard and the Wavelet based LR deconvolution. The Wavelet LR result is much less fluffy and matches the original uniform grid much better, except for the decrease in intensity. In fact, there are still residues of the cross structure outside the grid, but they are not visible in this scaling. They would be even smaller if a better treatment of the low shift invariance was developed as presented in the following sections.*

even before any reconstruction is undertaken. This decrease is exclusively due to the optics characteristic, the original source had a perfectly uniform intensity. We can see the effect of the cross structure in the PSF, which "extends" grid bars towards the image edges and also creates false peaks in central grid vertices.

These extensions are removed in both versions of the LR deconvolution, as can be seen in Figure 5.8. But these extensions are still visible if other than the linear intensity scaling is used.

Although the original source intensity was uniform, the source intensity in case of the Multiresolution LR drops towards the edges. On the other hand, the intensity seems quite uniform in case of the Standard LR. However, a close look at the Standard LR deconvolved image shows that although the peak intensity is relatively stable, there are larger gaps inside the fluffy area of the source near the edges of the image. Hence, the averaged intensity would decrease as well.

Both problems with the fading intensity even in the reconstructed image and with still visible cross–residua are the consequence of not incorporating the effect of changing PSF across the image. The solution of the effect will be further discussed in Section 5.3.4.

### 5.3.3 Astronomical Sources

To verify the effect of the MR LR algorithm applied onto the typical astronomical X–Ray data, we have simulated a number of various point sources with relatively low fluxes, i.e. with large photon noise. A small portion of the resulting $400 \times 400$ pixel image is plotted in Figure 5.9. The smaller view was chosen to make the fine structure of the peaks more clearly visible.

We have performed the reconstruction after the simulation using the Standard and the MR Lucy–Richardson method with automatic noise estimations and thresholding at the level of $3\sigma$. The results are also plotted in Figure 5.9.

We have keep in our mind that the simulation and/or the image were created relatively deep inside the FOV of the optics where the change of PSF is relatively small, yet still exists and can influence the reconstructing process. However, neglecting it is a good first guess and can fulfills the needed accuracy in many cases.

Let us first briefly describe the results. The result of the Standard LR is plotted in the middle. Point sources are clearly visible, yet have various and not point–like shapes. The background noise is still present, although significantly reduced. The noise is present in the form of stand–alone pixels.

The result of the MR LR is plotted on the right. Point sources are also clearly visible as in case of the Standard LR method. On the other hand, most of sources

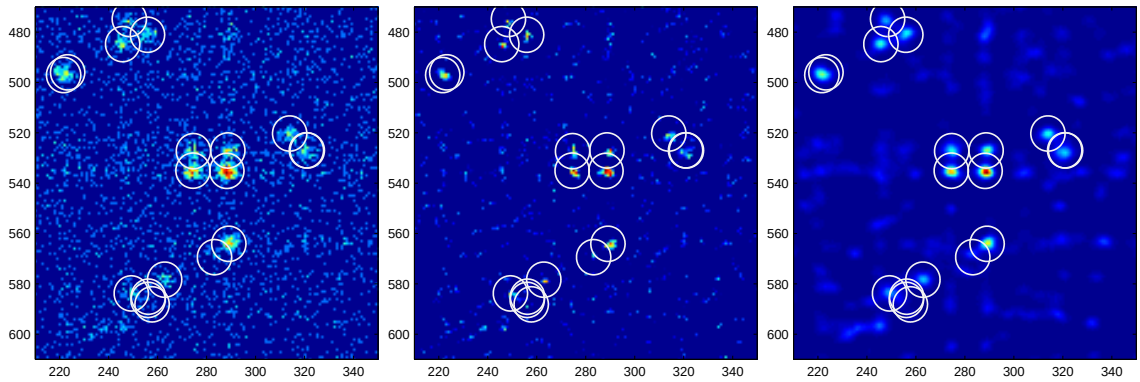


**Figure 5.9:** *A small portion of the realistic sky image, i.e. the initial simulation (left), the standard Lucy–Richardson deconvolution (middle), and the Multiresolution version of the Lucy–Richardson method is plotted. The images are* $140 \times 140$ *pixels, each pixel* $50 \times 50$ $\mu m^2$. *There is a square root intensity scaling used in each of the images to enhance the visibility of low flux highly noised data. We have plotted thin circles around several of original source positions. Although some improvements in both methods can be incorporated, especially in the noise estimation, the sources reconstructed using the MR LR are much better resolved and look more like "stellar" objects as known from the optical astronomy. This shape is better suited for the standard astrometry methods as well as for the standard astronomical PSF fitting methods. Intensities are in sqrt scaling.*

are smoothly shaped and resemble the sources known from the optical astronomy. A number of methods for the source position detection and the source intensity measurement using the PSF fitting is developed in the visible light astronomy supposing such a shape of the sources, i.e. the smooth Gaussian profile. The noise is present rather in form of relatively dark, flat, and extended sources. These are mainly residua of the cross structures of the bright sources at low resolutions. This effect can probably be somewhat reduced if proper change of the PSF shape with the peak position on the detector is incorporated.

We have made a simple aperture photometry for similar data as presented above in order to check if there really exists some enhancement or at least if the method does not produce nonsense. The experiment was done using the following properties:

- There was a number of sources, the brightest 40 of them are well distinguishable from each other, i.e. have different positions. The rest are faint sources and produce only the noisy background.
- The observation was done 10×, each image was reconstructed using the Standard and the Multiresolution Lucy–Richardson method.
- We have performed an automatic peak intensity estimation after the reconstruction using the $9 \times 9$ pixels window with the 2D binomial profile.

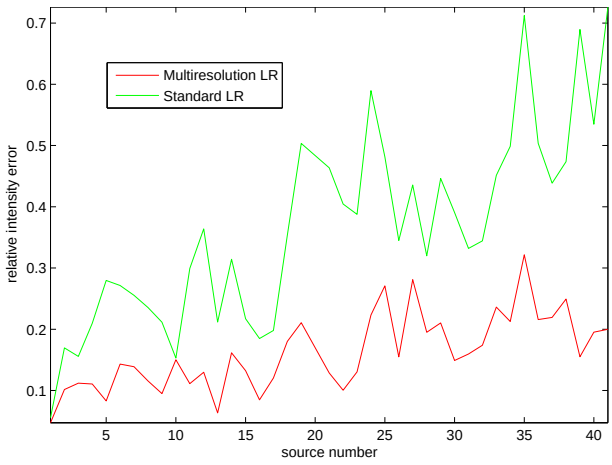


**Figure 5.10:** *The relative error of measuring the source intensity, averaged across 10 distinct experiments. The sources with a larger source index are less bright and suffer from the noise more significant. The estimation of the intensity is less robust for them. Although both methods have the same trend, we can see that the MR LR has systematically better results for the whole sample.*

- Measured intensities were corrected for vignettation.
- The ratio between the measured intensity and the original source intensity was taken as the comparable output.

Output of the measured intensities, which were normalized to the input intensities, should be spread around the unity. The better the reconstruction, the lower the dispersion around unity is measured. We have calculated the relative error of the measured intensity across all 10 experiments for each source. The result is plotted in Figure 5.10. The sources are sorted by descending intensity.

It is clear that for fainter sources the uncertainty in each measurement raises, thus the relative error is larger. However, the image shows that we obtain statistically better intensity estimates using the Multiresolution LR method. In fact, the average intensity error estimated for this particular sample was $\sim 37\%$ in case of the Standard method, while only $\sim 16\%$ in case of the MR LR.

### 5.3.4 Spatially Dependent PSF Deconvolution

Reverting integrals (5.2) or (5.3) leads to calculation of integrals:

$$O * P \equiv \int_{a,b} O(a,b)P(x-a,y-b)da\ db \tag{5.25}$$

and/or:

$$\int_{a,b} O(a,b)P(a,b,x-a,y-b)da\ db \tag{5.26}$$

Expression (5.25) is relatively simple and it can be evaluated using even a straightforward computation in relatively small time. A method to calculate a convolution of two matrices using the Fast Fourier Transform (FFT) can be effectively used, especially for large matrices.

On the other hand, to evaluate expression (5.26) is much more challenging. Let us suppose that we have a $256 \times 256$ px$^2$ image, and hence we should have also $256 \times 256$ distinct PSFs. Expression (5.26) can be rewritten into matrix multiplication, where the input image and the output image are transformed into a row vectors by putting the image rows one after the other. Each input/output vector would have 65536 elements. The transform matrix, i.e. the rewritten general $P(x,y,a,b)$, would be a matrix with dimensions $65536 \times 65536$. Moreover, it is clearly not a sparse matrix, it would have a large percent of nonzero elements and at rather random positions. It is extremely difficult even to store such a matrix in an ordinary computer, let alone to make computations.

Generation of such a matrix would be relatively complicated. Each row would be a PSF of a point source with the center located at a pixel given by the row index. Therefore, we either have to simulate 65536 distinct PSFs, or to simulate a lower number and then to interpolate.

Generally speaking, if the image has $N \times N$ pixels, the amount of memory as well as the complexity grows as $N^4$. Hence, for just twice larger image it is 16 times more difficult to get the result.

In general, there are two concepts to solve this problem:

- Split the image into smaller areas (tiles, subdomains), where the PSF can be considered to be constant.
- Decompose the changing PSF into a linear combination of some basic PSFs and calculate the convolution with varying coefficients of their linear combination. This concept resembles a "Taylor series".

### Image Splitting

The key is to modify the simple equation (5.25) to remain relatively simple, yet to resemble the output of the equation (5.26). In order to do that, let us first split the plane $S$, where the convolution is to be made, into a number of distinct areas $S_i$,

where $i = 1..N$. Further, let us define:

$$O_i(a,b) = \begin{cases} O(a,b) & (a,b) \in S_i \\ 0 & (a,b) \notin S_i \end{cases} \tag{5.27}$$

Thus, it is simple to show that:

$$O(a,b) = \sum_i O_i(a,b) \tag{5.28}$$

Now we can rewrite (5.25) as:

$$O * P = P * O = P * \sum_i O_i = \sum_i P * O_i = \sum_i O_i * P \tag{5.29}$$

In case of a shift invariant system we get nothing new from the equation (5.29). But if P is changing across the detector, we should evaluate $O_i * P$ using rather $P$ which would be observed inside $S_i$. Hence, we should write:

$$\sum_i O_i * P \rightarrow \sum_i O_i * P_i \tag{5.30}$$

where $P_i$ is the average PSF of the sources inside the $S_i$ shifted to the coordinate system center. If the number of distinct areas $N$ is large, we can mimic the behaviour of (5.26). The idea is to split the image into the number sufficiently high to get a smooth and relatively precise result, while keeping $N$ small enough to retain the computational time and memory consumption at acceptable levels.

In our computation, instead of moving the PSF obtained for the source inside $S_i$ into the coordinate system center, we have moved the $S_i$ into the coordinate system center, while keeping the PSF as it is. There is a straightforward advantage, that $S_i$ is often much smaller than the PSF and, hence, the computational demands are much lower than in the opposite case.

We have put the result of such a convolution in Figure 5.11. The original input was the large grid known from Figure 5.8. We have split the image area into $8 \times 8$ distinct parts and simulated the PSF for each part. We have supposed that the PSF shape and/or intensity does not change remarkably across the small image part. Despite the decomposition of the problem into parts, it took $\sim$ 20 min to get the result for $800 \times 800$ px$^2$ data in Matlab on the 1GHz PIII and 512 MB RAM computer using the FFT for convolution.

We can see that the convolution presented in Figure 5.11 resembles the simulation from Figure 5.8 much better, although no noise was added here. The grid fades out towards the image borders, exactly as in the simulated ray–tracing observation of the grid. The effect of the cross structure of the PSF is also clearly visible, although built from a number of different PSFs.

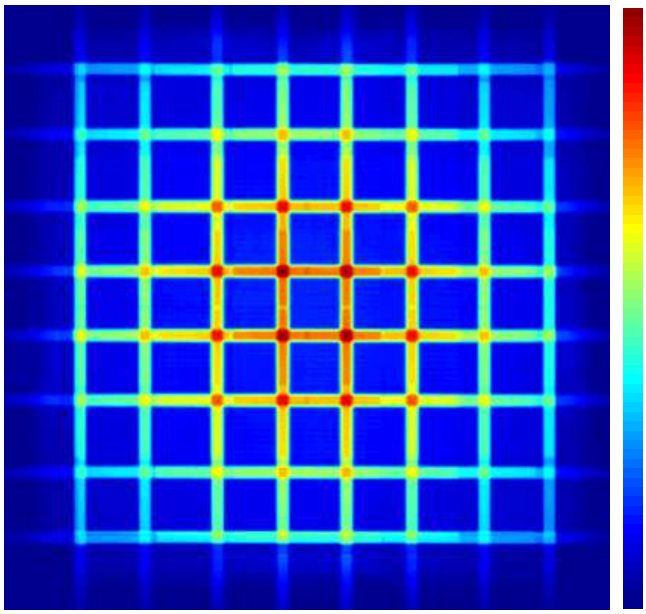

**Figure 5.11:** *An example of the approximation of integral (5.26). The integration was done as a sum of convolutions of* $10 \times 10$ *parts of the original image with the average PSF over the particular part. Such a method was used in order to decrease time/memory demands of the computation.*

### Karhunen Löve Decomposition

The other approach is decomposing a spatially dependent PSF into a sum of spatially independent basic PSFs [50]. This means that we rewrite the spatially dependent PSF $P(u, v, x-u, y-v)$ as:

$$P(a, b, c, d) = \sum_{i=1}^{\infty} a_i(a, b) p_i(c, d) \tag{5.31}$$

where $p_i(c, d)$ is the i-th basic PSF. The $p_i(c, d)$ is spatially stable, i.e. the same across the whole image. The parameter $a_i(a, b)$ is changing across the image. In fact, if we are able to sort the $p_i$'s according to the significance level in which the i-th basic PSF is dominant in any typical decomposition, it is often sufficient to use only several first terms in the summation, instead of the infinite summation.

Let us first suppose that the decomposition presented in equation (5.31) is possible. Integral (5.26) is then rewritten, after the substitution from equation (5.31) and rearranging the terms:

$$\int_{a,b} O(a, b) P(a, b, x-a, y-b) da\, db = \sum_{i=1}^{\infty} \int_{a,b} O(a, b) a_i(a, b) p_i(x-a, y-b) da\, db \tag{5.32}$$

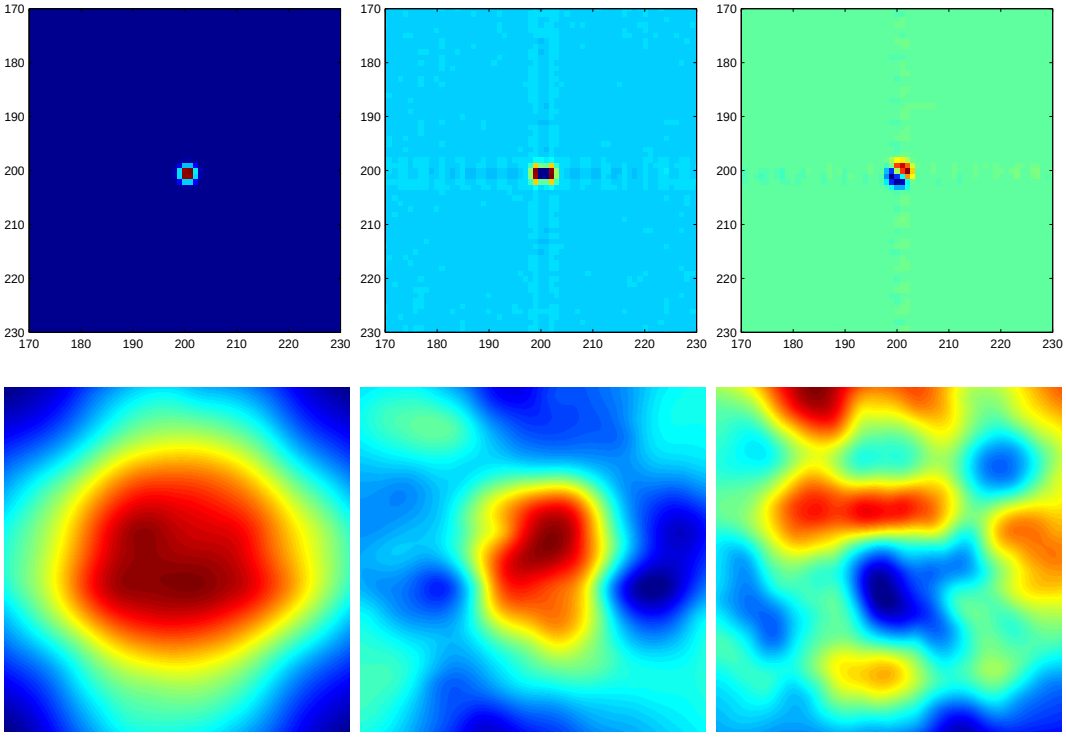


**Figure 5.12:** *Three most important base PSFs obtained using the Karhunen Löve decomposition are plotted in the upper row. In fact, only the central part of the PSF is plotted to emphasize its structure. The intensity is in sqrt scaling, and the intensity of the central peak is an order of magnitude larger in case of the first most important base PSF than the intensities in the following two. The second row shows the profile of the parameter $a_i$ across the image.*

This is a sum of convolutions of the image, which is modified by the factor $a_i$, with the basic PSF $p_i$. A few summations are enough to achieve a required precision in man cases.

Now, the problem is in finding the appropriate basic PSFs and the parameter $a_i$ profiles across the image. This is computationally the most complicated part of this approach. The Karhunen Löve decomposition [51] is typically used for this job.

The whole process can be expressed as the following algorithm:

1. generate or measure the set of PSFs $P_j$ across the detector
2. move all the PSFs into a single point and normalize them
3. generate a covariance matrix between all the PSFs $C_{i,j} =< P_i, P_j >$
4. calculate eigenvectors $v_i$ and eigenvalues $\lambda_i$ of matrix $C_{i,j}$

5. sort eigenvectors according to the decreasing eigenvalues
6. choose $N$ to be the number of needed summation terms for a desired precision
7. basic PSF $p_i = \sum_{j=1}^{N} v_{ij} P_j$, where $v_{ij}$ is the j-th component of $v_i$
8. generate or measure the set of PSFs uniformly distributed across the detector $F_j$, generally different from the first set of PSFs $P_j$
9. for each of $F_j$ move all the basic PSF $p_i$'s into the same point and find the optimal set of $a_i$ in this point, such that $\sum a_i P_i = F_j$
10. from the set of optimal $a_i$'s in centers of $F_j$ construct the distribution of $a_i$ across the whole detector using an interpolation

An example of the Karhunen Löve decomposition of the Lobster Eye output is plotted in Figure 5.12.

The differences between images 5.11 and 5.13 show that using the Karhunen Löve decomposition leads to a smoother profile of intensities. In fact, because the number of basic PSFs needed for such a profile is much lower than the number of tiles or subdomains in the other approach, the computation is much faster and uses far less computer memory. On the other hand, preparing all the basic PSFs (three in this particular case) and parameter $a_i$ profiles was much more difficult and time consuming. Fortunately, this complex computation is done only once for a given optics design and energy combination.

The natural question is what number of basic PSFs is needed in case of any typical LE design. Let us suppose that we have ordered our basic PSFs by the magnitude of eigenvalues of the covariance matrix $C_{i,j}$. The decision should be based on the "experiment" but there are several points which we need to kepp in mind:

- Variations of the PSF central peak shape are relatively small. The change can be practically neglected for low photon fluxes, which are expected in astrophysical applications. One should be more careful in laboratory applications, but the number of needed basic PSFs would not increase substantially due to this effect.
- Variations of the PSF central peak height are relatively large, but are sufficiently covered by the first basic PSF, because the decrease in the peak intensity is almost fully described in distribution of its $a_i$ parameter. Other basic PSFs are rather a correction to the first one.
- Variations in the cross shape and/or position within the PSF lead to an increased number of basic PSFs. It would also need also simulated PSFs than

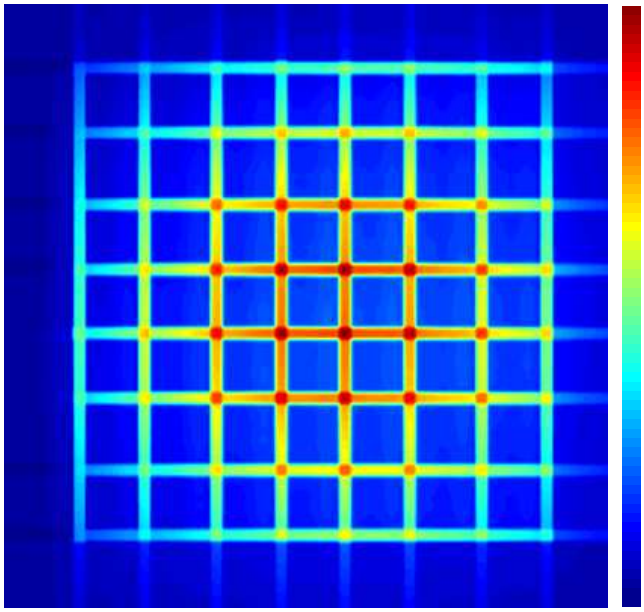

**Figure 5.13:** *An example of the approximation of integral (5.26). The integration was done as a sum of convolutions of three most important Karhunen Löve PSF decompositions.*

the actual image size. In other words, we have moved all the simulated PSFs into the center of the image to create the covariance matrix. Shifting the PSFs from the outer parts of the image towards the center would carry a truncated part of the cross (the part outside of the image). Hence even larger number of basic PSFs may be insufficient without larger pixel number.

We have used only first three basic PSFs in our simulation with satisfactory results. Of course, the results were satisfactory for the given application, i.e. the demonstration of convolution and processing of large scale structure.

### Low Shift Invariance Lucy–Richardson Modification

A low shift invariance modification of the Lucy–Richardson method is based on equation (5.24), where each convolution is calculated using the methods mentioned above. The general concept is described in [50].

In fact, two kinds of convolutions are present in the algorithm:

**forward:** where the true image of the sky or at least the estimate of the true image is convolved with the PSF to obtain the really observed image estimate

**backward:** where we convolve one of terms with the transposed PSF to obtain the correction of the true image estimate

If we wish to incorporate not only the change of the PSF shape but also the decrease of the PSF height with the distance from the optical axis, we need to modify the algorithm described in [50]. There are several simple steps how to realize the need for such a modification (please have equations (5.23) and (5.24) in mind while reading the following steps):

1. Let us suppose first that the original image of the sky is ideally flat, and hence the image which we observe is axially symmetric with intensity falling towards the edges of the image. This will be our input image.
2. Now let us start the standard Lucy–Richardson method.
3. Let us take a purely flat image as the first guess for the true image.
4. Let us convolve such a flat image with the Spatially Variant PSF, we obtain axially symmetric image with the intensity falling towards the edges of the image.
5. Correction factor from (5.24) is $\sim \frac{I}{I^{(n)}} * P(-x,-y)$. Because $\frac{I}{I^{(n)}}$ is almost constant over the whole image in our case, the resulting correction factor would be axially symmetric again with the intensity falling towards the edges of the image.
6. Hence, next guess for the original image should be corrected to have falling edges, which is in contradiction with the fact that our first guess was already near the optimum.

Therefore, in order to incorporate the change of the PSF height, the forward convolution has to be made using the true spatially dependent PSFs, which change both the shape and height, but a backward convolution has to be done using the normalized spatially dependent PSFs, which differ in shape, but has the equal heights.

We have used this modification of the Standard (not the MR) Lucy–Richardson method to process the image of the large grid presented in previous sections. The simulation and the reconstruction are plotted in Figure 5.14.

The method described here does not conserve the flux of the sources, which is the main feature of the LR method for astronomical purposes. On the other hand, a flatfielding is typically applied onto the image reconstructed using the LR method and the flatfielding itself does not also preserve the flux of the sources either. The above described modification of the LR algorithm performs a kind of flatfielding directly in the deconvolution process and thus the method is still perfectly usable.

Exactly the same modification can be made with the Multiresolution version of the Lucy–Richardson method.

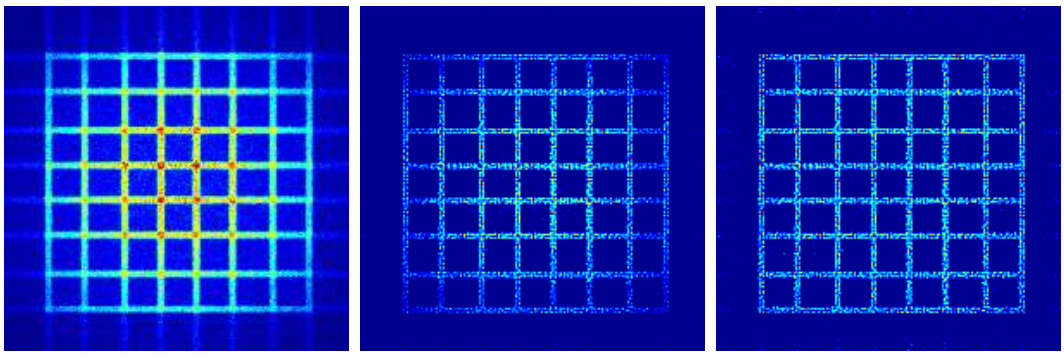

**Figure 5.14:** *The original simulation is plotted at left. The Standard LR deconvolution using a spatially variant PSF and splitting the image into a number of subdomains, where the PSF is relatively stable, but having the same PSFs for forward and backward convolution, is plotted in the middle. The same as the middle case except that a backward convolution uses the normalized PSFs. It is clearly visible that the output of the method with normalized PSFs for the backward convolution displays a uniformly bright grid, which is exactly the expected output. There are 150 iterations in each deconvolution.*

### 5.3.5 Summary

The Lucy–Richardson image reconstruction method is perfectly amenable to any X–Ray LE data. The method in its Multiresolution modification seems to have better resolving power for both astronomical and laboratory measurements if compared to the Standard form. We strongly encourage people to use the MR LR instead of the ordinary LR for processing any LE data. We would also recommend to use the Karhunen Löve decomposition into at least several basic PSFs for laboratory data, especially if a good imaging is desired. We would be rather cautions in incorporating it into processing of astronomical data, because the flux conservation is violated and it should be treated more carefully. Those who are interested in astronomical data should rather try the CLEAN method first, they would be probably more satisfied.

## 5.4 CLEAN

### 5.4.1 Standard Algorithm

The Standard CLEAN algorithm is designed to process an image of a number of point sources with a rather complex PSF. It was originally designed for radioastronomy, but we can use it wherever the condition of the point source is matched.

Let us first define several terms compatible with other literature where you can

find the CLEAN method description:

**dirty map:** is the image which you really measure

**clean map:** is the reconstructed image

**dirty beam:** is the PSF of the detecting optics and/or instrument

**clean beam:** is the ideal PSF used for generating the clean map from the set of source positions and intensities obtained during the processing (will be explained later)

The algorithm can be described as:

1. set $I_0$ equal to the dirty map
2. locate the maximum at the image $I_i$, the output of this step are coordinates $[x_i, y_i]$ of the i-th source candidate
3. find the dirty beam $PSF_{[x_i,y_i]}$, i.e. the PSF shifted into $[x_i, y_i]$ and multiplied with such a factor $s_i$, that $PSF_{[x_i,y_i]}$ matches the source the best
4. remember the values $[x_i, y_i]$ and $s_i$
5. subtract $PSF_{[x_i,y_i]}$ from $I_i$, the result is $I_{i+1}$
6. if ending condition is met, go to the next step, otherwise set $I_i = I_{i+1}$ and go to step 2.
7. convolve the set of source positions and intensities with the clean beam to obtain the clean map

There can be several ending conditions, depending on our problem:

- we break if a number of found sources reaches some previously set limit $N_{lim}$. It is important to note that some sources, especially the bright ones, are found several times during the iterations because they are slightly extended.
- we can break if the residual image $I_i$ looks much like the noise, hence when there is no pixel exceeding the $5\sigma$ limit for example
- any other condition made specially for the case of our application

The algorithm is strongly affected by the noise. It is quite difficult to find the correct source position if the source is only one or two pixels wide. Therefore, the image is often slightly smoothed by a low–pass filter before the algorithm is applied.

Additionally, if we deal with low fluxes and larger dirty beams, one needs to be careful when performing the subtraction. For instance, when the best fit for a central peak is found, it can lead to negative values at $I_{i+1}$ because of the noisy data at the low–flux–part of the PSF.

### 5.4.2 Multiresolution Algorithm

The Multiresolution version of the CLEAN algorithm is designed to be able to resolve both the point sources as well as the extended sources. It is a simple modification of the standard CLEAN algorithm:

1. decompose the dirty map into wavelet coefficients (planes) $I^j$, where $j$ denotes the resolution
2. decompose the PSF into wavelet coefficients (planes) $PSF^j$, where $j$ denotes the resolution
3. set $I_0^j$ the wavelet plane $I^j$
4. locate the maximum at the image $I_i^j$, the output of this step are coordinates $[x_i^j, y_i^j]$ of the i-th source candidate in resolution $j$
5. find the dirty map of the source at resolution $j$ $PSF^j_{[x_i^j, y_i^j]}$, i.e. the $PSF^j$ shifted into $[x_i, y_i]$ and multiplied with factor $s_i^j$ such, that $PSF^j_{[x_i^j, y_i^j]}$ matches the source the best
6. remember the values $[x_i^j, y_i^j]$ and $s_i^j$
7. subtract $PSF^j_{[x_i^j, y_i^j]}$ from $I_i^j$, the result is $I_{i+1}^j$
8. if ending condition is met, go to the next step, otherwise set $I_i^j = I_{i+1}^j$ and go to step 4.
9. if $j = N$ where $N$ is the number of resolutions, then go to next step, otherwise set $j = j + 1$ and go to step 3.
10. decompose the clean beam into wavelet coefficients, convolve the set of positions and intensities at each resolution with the decomposed clean beam and compose the final clean map.

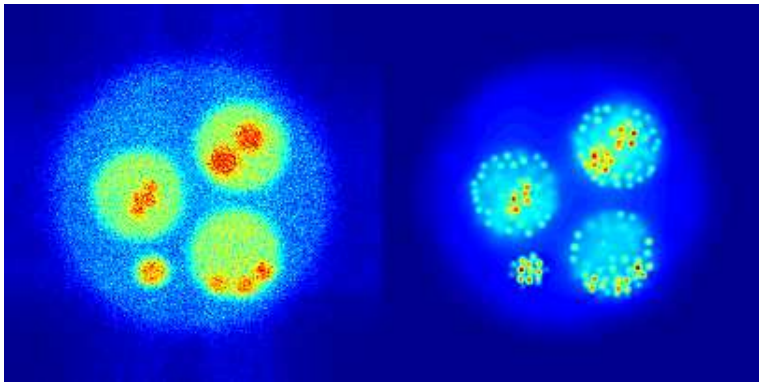

**Figure 5.15:** *An example of image processing using the Multiresolution CLEAN method. The simulated image (left) was iteratively decomposed into point sources at different scales, the output is plotted on the right part of the image. The tendency to find point sources at different scales is clearly visible.*

Please note that processing the wavelet planes can lead to completely different sets of "the sources" and in principle in completely different positions, although it lead to the correct reconstruction. We can find some extended sources in different positions than the point sources thanks to this behaviour.

An example of such processing is plotted in Figure 5.15. Smaller extended sources are decomposed into a set of point sources, while larger extended sources are correctly decomposed into a slowly fading large extended source. The problem is visible at the edges of the large extended source, where the intensity fades rapidly. The fast intensity change is the sum of large slowly fading source with a number of point sources located at the edge.

The CLEAN method generally has a tendency to resolve point sources at different scales.

### 5.4.3 PSF Generation

Correct processing using the CLEAN method is dependent on a precisely measured or generated PSF. It is completely sufficient to have a single simulated PSF and just shift it into the correct position if we deal with the shift invariant optical system. It would be necessary to divide the intensity between several pixels if a non-integer shift is desired.

On the other hand, if we deal with a non–shift–invariant optical system, we need to use an algorithm that returns the PSF properly according to the central peak position. It is clearly impossible, because of time efficiency, to simulate the PSF each

time we get a new source position. Therefore, we need to make some computations in advance to simplify obtaining the correct PSF just in time.

The idea is to compute the PSFs as smooth as we can for a number of points/sources at the sky, all equally bright. An example of such a calculation is plotted in Figure 4.20. There are only requirements on the equal intensity of all sources and for a rather uniform distribution of the sources over the detector. There is no need to align the sources into any kind of structure like in Figure 4.20.

Now, let us suppose that we need to compute the PSF with the peak position $[x, y]$ at the detector. Such a PSF will be a linear combination of the three "nearest" PSFs from a pre-computed set of the PSFs which are moved into the position $[x, y]$. The meaning of word "nearest" will depend on a particular algorithm used for tracing the $[x, y]$ surroundings. We have used the standard MATLAB function for the Delaunay triangulation in our case, and the word "nearest" means the three vertices of the triangle into which point $[x, y]$ belongs.

Hence, if $\mathrm{PSF}_{xy}$ is the PSF with the peak in $[x, y]$, and $\mathrm{PSF}_1$, $\mathrm{PSF}_2$, and $\mathrm{PSF}_3$ are the PSFs from the vertices of the surrounding triangle moved simply to the $[x, y]$ position, we can write:

$$\mathrm{PSF}_{xy} = \gamma \mathrm{PSF}_1 + \alpha \mathrm{PSF}_2 + \beta \mathrm{PSF}_3 \tag{5.33}$$

$$\alpha = \frac{\vec{u} \cdot \vec{w} v^2 - \vec{u} \cdot \vec{v} \vec{v} \cdot \vec{w}}{u^2 v^2 - (\vec{v} \cdot \vec{u})^2} \tag{5.34}$$

$$\beta = \frac{u^2 \vec{v} \cdot \vec{w} - \vec{v} \cdot \vec{u} \vec{u} \cdot \vec{w}}{u^2 v^2 - (\vec{v} \cdot \vec{u})^2} \tag{5.35}$$

$$\gamma = 1 - \alpha - \beta \tag{5.36}$$

where $\vec{u}$ and $\vec{v}$ are vectors of two edges of the triangle sharing one vertex as the origin, while $\vec{w}$ is a vector from the origin vertex to the $[x, y]$ position.

The same algorithm can be used for both the Standard and the Multiresolution version, except that in the Multiresolution version we treat each resolution separately.

### 5.4.4 Lobster Eye Application

The algorithm was used for reconstructing the simulation of realistic sky data. The result is plotted in Figure 5.16. The actual PSF was computed from 20 different PSF models spread across the image. Point sources are resolved exactly as expected. Expected source positions are encircled.

The ratio of measured and expected intensities is plotted in Figure 5.17. The relative dispersion is $\sim$ 24%, which is consistent with an analogous reconstruction

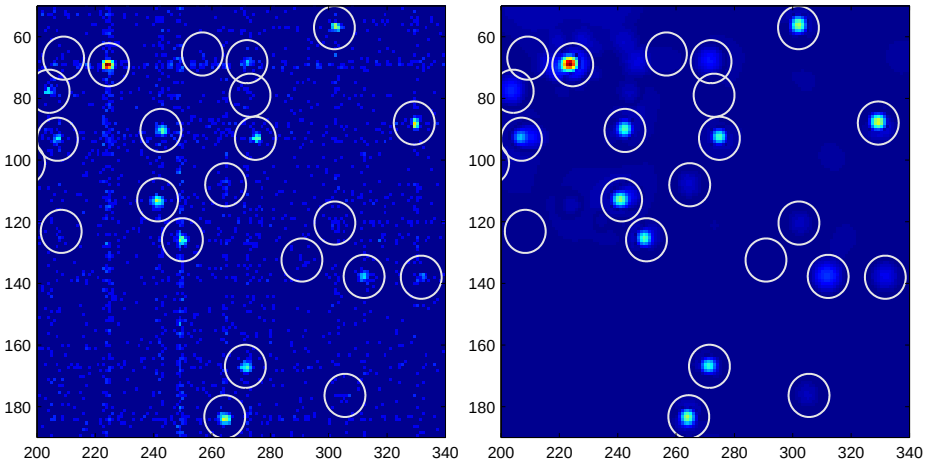


**Figure 5.16:** *The Multiresolution CLEAN method used for reconstructing the data (left) is plotted on the right image. Intensities are in sqrt scaling, images have* $400 \times 400$ *pixels.*

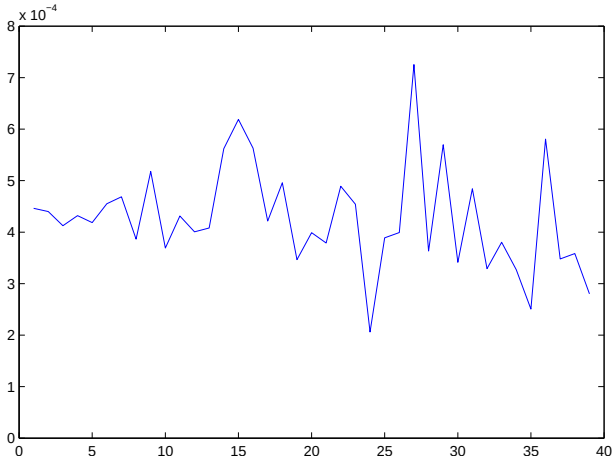


**Figure 5.17:** *The ratio of the measured value after the Multiresolution CLEAN reconstruction and the true intensity used for the simulation. The plot should be a straight horizontal line in the ideal case. Y values are in arbitrary units.*

made by the Lucy–Richardson method. Please note that just the Poisson nature of the process itself would lead to the relative dispersion $> 13\%$.

There is one substantial difference if compared to the MR LR. The effect of the changing central peak intensity as well as the changing PSF shape was not incorporated in the LR processing, and measured values had to be after corrected for vignettation. On the other hand, all the changes of the PSF are taken into account in the CLEAN method from the very beginning.

If compared to the spatially dependent modification of the MR Lucy–Richardson is the MR CLEAN much faster, although it can be memory consuming. The demands depend on the number of PSF models for generating the actual PSF. Efficient distribution of these model PSFs has to be used.

### 5.4.5 Subtracting

#### Localizing the Brightest Source

The most simple way is to find the pixel with the maximal intensity. This is the first guess for the position of the brightest source. Then refining of the source position using a weighted averaging through some window is applied. Although it is simple, this method generates very good results.

A more sophisticated approach takes a probabilistic nature of the emission and/or detection process into account . The whole process can be divided into two steps:

1. localize the sources
2. find the brightest

In the fist step, we need to know the estimate of an average background count rate and an estimate of a typical point source size in the image. The typical point source size restricts the size of the averaging window. We then move the averaging window across the image and whenever the average flux exceeds the limit given together by the Poissonian distribution, the background count rate, and the probability limit, we have a source candidate. All candidates ordered by the intensity give the estimate of the brightest source. The position will be refined immediately using the averaging across the window and the estimate of the source intensity will be computed as well.

There is a disadvantage that a single source will produce several source candidates, as the averaging window moves with a single pixel step while the typical source size is several pixels. Fortunately, all these candidates will differ in intensity, and only the brightest one is the one we are looking for.

### Fitting the PSF

In this step, we assume that the change in position is less or equal than one pixel and the PSF does not change substantially up to this one pixel shift. Changing the position of the PSF is done by splitting of the signal from one pixel into several surrounding pixels proportionally to the shift. The only value which can change substantially is the intensity scaling of the PSF.

While the cross of the PSF is important because it influences the other sources, the main peak is essential for the carefully examined source. Therefore, we select only the central peak area and fit the source using only this part of the PSF. Such approach has several advantages. First, only the area near the source influences the fitting, while the further sources will not impact the process. Second, much faster processing is possible, because the lower number of pixels has to be examined.

The area of the image, which has to be examined in each step, i.e. the central peak area, can be defined in several ways. One is the manual definition for each or the pre–computed PSFs and a linear combination of these areas. Another way, which was also initially used, is thresholding the PSF to remove the crossing bars.

The process itself is to minimize the function $F$ with respect to the parameter s:

$$F(\mathrm{x},\mathrm{y},\mathrm{s}) = \sum_{\text{surroundings}} \left(\mathrm{SRC} - \mathrm{s} \times \mathrm{PSF}(\mathrm{x},\mathrm{y})\right)^2 \tag{5.37}$$

where [x, y] is the PSF shift, s is the intensity scaling factor of the PSF to fit the source, PSF(x, y) is the shifted PSF, and SRC is the really measured image on the detector.

### Subtracting the PSF

We now know the position and scaling of the fitted PSF. A simple subtraction of such a scaled PSF from the image can produce reasonable results if a large number of detected photons or long exposure time is available.

A typical X–ray observation, however, will look like the one plotted in Figure 5.18. A simple subtraction would often lead to negative values and consequently to false peaks. We should respect the probabilistic nature of the emission/detection process.

In fact, the scaled PSF represents the mean value of a random variable with the Poissonian distribution. We can calculate the $p$–bounds for such distribution, which shows the interval where we can expect a random value with the probability $p$. An example for $p = 95\%$ is plotted in Figure 5.19.

The subtracting algorithm has to be modified in such way that we calculate the $p$–bounds for each pixel at the image. Then for each of them we perform:

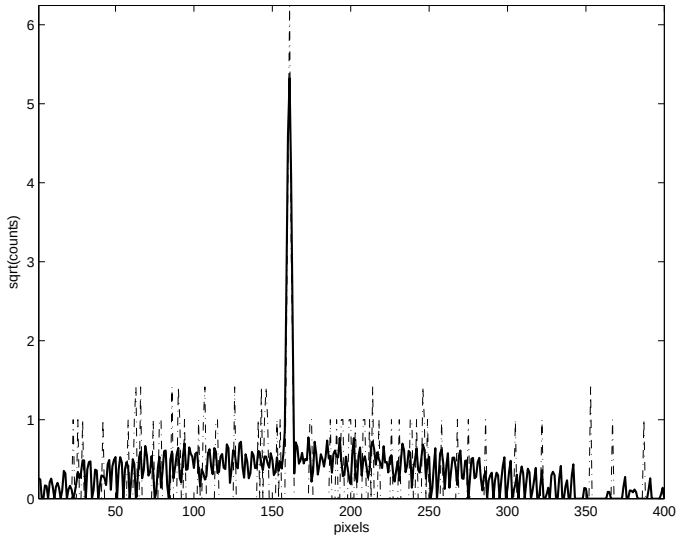


**Figure 5.18:** *An example of a fitted source.* 100 $\mu m$ *pixels are on the x–axis, square root of counts detected on a given pixel is on the y–axis. The dotted line is the real detected profile, the solid line is the fit.*

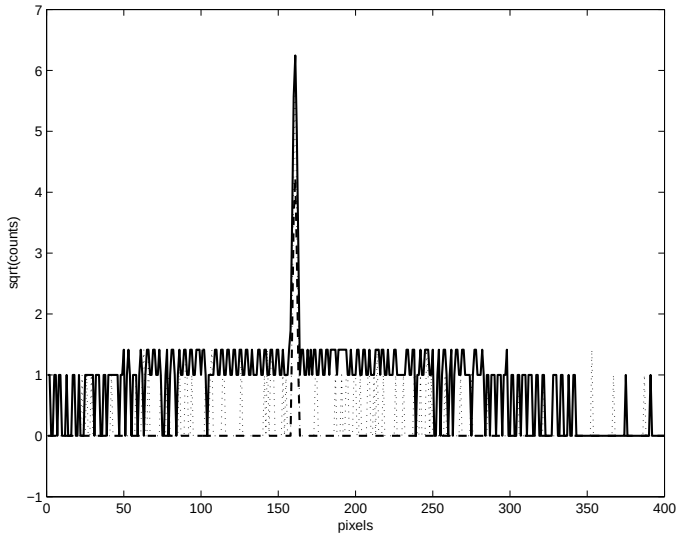


**Figure 5.19:** *An example of a fitted source.* 100 $\mu m$ *pixels are on the x–axis, square root of counts detected on a given pixel is on the y–axis. The dotted line is the really detected profile, the solid line is the upper boundary, and the dashed line is the lower boundary for the probability of* 95%.

- if the pixel value is between the probability bounds, subtract the whole pixel value
- if the pixel value is above the upper bound, subtract the scaled PSF value, which is equal to the mean value
- if the pixel value is below the lower bound do nothing

In the Multiresolution CLEAN method, the wavelet coefficients at each resolution are generally real numbers with a zero mean value, in ideal case. The statement still holds even for small photon counts. The simple subtraction is now amenable much better and produces well formed sources of correct intensity. Processing plotted in Figure 5.16 was done using such a simple subtraction.

A modification of the probabilistic subtracting algorithm for the Multiresolution CLEAN is similar to the one presented above. For each wavelet coefficient in each resolution plane we calculate a $p$–bounds supposing that the ideal value would be the one obtained from the scaled PSF. Then:

- if the wavelet coefficient value is between the probability bounds, subtract the whole wavelet coefficient value
- otherwise, subtract the mean value

The question is how to calculate the $p$–bounds in this case. We have currently been working exactly on this problem, but, unfortunately, we have currently no valid solution yet to be presented in this work.

### 5.4.6 Summary

The Multiresolution version of the CLEAN method seems to be ideal for any of X–Ray ASMs, because we typically encounter the point sources and potentially a few extended sources. The method is quite fast and sufficiently accurate.

On the other hand, it is not ideal for the laboratory LE, where the sources of complex shape can be found. The method has tends to find the point sources at any scale, and therefore the reconstructed image is “dotted”.

# Chapter 6

# Conclusions

We have tried to analyse the optical and/or imaging properties of the Multi–Foil optics designs and to use the acquired knowledge for analysing the methods for the future image processing.

In order to achieve this goal, we have developed our own ray–tracing code for simulations of a number of optics designs. The code is now actively used and its validity was verified by comparing the ray–tracing results to the measured values.

In fact, the code has been successfully used for the design and development of the soft X–Ray condenser (Section 4.1). The purpose of the instrument is to gather as much X–Ray $\sim$ 100 eV photons as possible from the laser plasma source to the small area in the experimental chamber 400 mm away. Optical properties of the designed and manufactured condenser were already measured and they match those originally proposed. The condenser is now used for scientific measurements at Military University of Technology, Warsaw.

Once we had a powerful tool for the design verifications and optimizations, we have started to study several interesting X–Ray optics designs. Some of them are our original concept and some of them emerged from the discussions with our colleagues and we have further developed them in this work.

Our work logically started with the Standard Lobster Eye, as was theoretically developed by [2, 1] thirty years ago. The design is basically the wide Field X–Ray focusing optics. We have described for the first time more or less comprehensively its optical properties and especially the imaging capabilities. We have shown the limitations of the uniformity of displayed sources, changes of the source shape across the FOV, and the dependance of the properties on the incoming photon energy. Although the results are shown for one particular Lobster Eye optics, the results can be simply generalized to the designs which differ in dimensions and/or dimension ratios.

A special interest has been devoted to the study of positional errors and to their importance for scanning observations performed the Standard Lobster Eye. Specific distortions have been shown explicitly for the first time, as well as the overall imaging capabilities at the scanning mode. The results show that the Standard Lobster Eye is ideal tool for an scanning observations, although the positional shift corrections have to be applied for correct results.

One of the other designs, which are typically the Standard Lobster Eye modifications, has emerged from a discussion with our colleagues and we call it the Hybrid Lobster Eye. It is specially designed to have a better angular resolution in one direction at the expense of a smaller FOV in this direction. The work was originally motivated by the typical use case of the instrument, i.e. the scanning observations. Although we have proven an increase in the angular resolution, we have encountered a substantial decrease in the source intensity. Consequently, the design can be used only for scanning observations of bright sources or for pointed observations of asymmetric sources in the laboratory.

Our next completely new design, the Gently Focusing Lobster Eye, preserves the advantages of the Standard Lobster Eye but provides a better angular resolutions in both directions. In fact, all the mirrors of the Standard LE are equally bent in order to increase the focusing power of each mirror. However, the discussions and computations showed that it is extremely difficult to built it with the current level of technology. Yet, the design itself has been proven to work as expected. There exist possible future technological ways for manufacturing it or at least its derivatives.

All our calculations, simulations, and experience with the Lobster Eye or the Multi–Foil Optics show that the Standard Lobster Eye (and possibly the Gently Focusing Lobster Eye in the future) is the best choice for scanning astronomical observations, while the general Multi–Foil Optics carefully designed for a given purpose is the best for the laboratory and/or the industry.

We have also proposed several other X–Ray optics as spin–offs of our ray–tracing code development and other work during several years.

The one which can be published here in this work has emerged as a consequence of our participation in the discussions about the proposed XEUS mission. It led us to a "gedanke" experiment and/or design. We have proposed the large space based X–Ray telescope working on the principle of modifying the wave front. In fact, it is a large spinning cylinder filled with gas. Such optics then focuses, although at extremely large focal lengths at the order milion of kilometers. Although there already exist technically similar laboratory optics, the idea of the space based spinning gas is unique as far as we know. We have outlined the basic concept in this work together with initial calculations and questions to be further solved.

The second part of our work uses the output of the design process of the Lobster

Eye optics and its derivatives, namely the simulations of the observations made with such an optics.

We have studied the image processing and reconstruction methods for images obtained by such a kind of optics. We have used two basic reconstruction methods, the Lucy–Richardson method and the CLEAN method, and multiresolution modifications of both of them.

The Lucy–Richardson method showed to be ideal for laboratory sources of any shape and even under small count–rates. The best results were obtained with its Multiresolution version. However, because of some image distortions shown in Section 4.2, we strongly recommend to use some technique to manage the small uniformity of the PSF across the FOV. The effect is often neglected, but can lead to strong distortions especially at large off–axis distances. The implementation was shown to be relatively simple and fast.

Although the Lucy–Richardson can be successfully used for point or point–like sources, the CLEAN method gives even better results. Its Multiresolution version is able to resolve astronomical fuzzy sources like nebulae, and no additional modification for the small uniformity of PSFs across the FOV is needed. It is an integral part of the method. However, the method gives poor results for laboratory sources with complicated borders.

We believe that the Lobster Eye optics and its derivatives, as well as some of the other mentioned optics designs, have an interesting future in both commercial and/or on–the–ground applications as well as for astronomical purposes. We have tried to show their benefits and potential problems, which one has to face during the selection of the right optics and the consequent data processing. If anyone finds this helpful for his/her own work, our attempts would succeed.

# Bibliography

[1] J. R. P. Angel. Lobster eyes as X-ray telescopes. ApJ, 233:364–373, October 1979.

[2] W. K. H. Schmidt. A proposed X-ray focusing device with wide field of view for use in X-ray astronomy. *Nuclear Instruments and Methods*, 127:285–292, 1975.

[3] A. G. Michette. REVIEW ARTICLE: X-ray microscopy. *Reports of Progress in Physics*, 51:1525–1606, December 1988.

[4] R. Hudec, L. Sveda, A. Inneman, and L. Pina. Astronomical lobster eye telescopes. In G. Hasinger and M. J. L. Turner, editors, *Proceedings of the SPIE, Volume 5488, pp. 449-459 (2004).*, pages 449–459, October 2004.

[5] B. Haisch and J. H. M. M. Schmitt. Advances in Solar-Stellar Astrophysics. PASP, 108:113–+, February 1996.

[6] http://en.wikipedia.org/wiki/H-R_diagram.

[7] http://en.wikipedia.org/wiki/Roche_lobe.

[8] http://en.wikipedia.org/wiki/Lagrangian_point.

[9] H.-J. Grimm, M. Gilfanov, and R. Sunyaev. The Milky Way in X-rays for an outside observer. Log(N)-Log(S) and luminosity function of X-ray binaries from RXTE/ASM data. A&A, 391:923–944, September 2002.

[10] http://en.wikipedia.org/wiki/Chandrasekhar_limit.

[11] S. Immler and W. H. G. Lewin. X-Ray Supernovae. *LNP Vol. 598: Supernovae and Gamma-Ray Bursters*, 598:91–111, 2003.

[12] L. Sveda, Inneman P. Hudec, R., and S. Immler. SNe and Lobster Eye X-ray Telescopes. In Marcaide, J. M.., and K. W. Weiler, editors, *Cosmic Explosions: On the 10th Anniversary of Sn1993j (Iau Colloquium 192)*, 2003.

[13] J. Heise, J. in't Zand, R. M. Kippen, and P. M. Woods. X-Ray Flashes and X-Ray Rich Gamma Ray Bursts. In E. Costa, F. Frontera, and J. Hjorth, editors, *Gamma-ray Bursts in the Afterglow Era*, pages 16–+, 2001.

[14] A. G. Michette and C. Burkey. *X-ray science and technology*. Institute of Physics Pub, Bristol, 1993.

[15] B. L. Henke, E. M. Gullikson, and J. C. Davis. X-Ray Interactions: Photoabsorption, Scattering, Transmission, and Reflection at E = 50-30,000 eV, Z = 1-92. *Atomic Data and Nuclear Data Tables*, 54:181–+, 1993.

[16] J. H. Hubbell, W. J. Veigele, E. A. Briggs, R. T. Brown, D. T. Cromer, and R. J. Howerton. Atomic form factors, incoherent scattering functions, and photon scattering cross sections. *Journal of Physical and Chemical Reference Data*, 4:471–538, October 1975.

[17] http://www-cxro.lbl.gov.

[18] http://en.wikipedia.org/wiki/Classical_electron_radius.

[19] R. Němec. *Měření mikrodrsnosti optických povrchů v oblasti měkkého RTG záření*. PhD thesis, Czech Technical University in Prague, Prague, Czech rep., 1995.

[20] Š Višnovský. Lectures on optics.

[21] http://en.wikipedia.org/wiki/Abbe_Sinne_Condition.

[22] P. Kirkpatrick and A. V. Baez. Formation of optical images by x-rays. *Journal of the Optical Society of America (1917-1983)*, 38:766–+, September 1948.

[23] H. Wolter. A Generalized Schwarschild Mirror. Systems For Use. at Glancing Incidence for X-ray Imaging. *Ann. Physik.*, 10:286, 1952.

[24] http://www.src.le.ac.uk/projects/lobster/.

[25] W. C. Priedhorsky, A. G. Peele, and K. A. Nugent. An X-ray all-sky monitor with extraordinary sensitivity. MNRAS, 279:733–750, April 1996.

[26] M. Gertsenshteyn, T. Jannson, and G. Savant. Staring/focusing lobster-eye hard x-ray imaging for non-astronomical objects. In R. B. James, L. A. Franks, and A. Burger, editors, *Advances in Metrology for X-Ray and EUV Optics. Edited by Assoufid, Lahsen; Takacs, Peter Z.; Taylor, John S. Proceedings of the SPIE, Volume 5922, pp. 107-117 (2005).*, pages 107–117, August 2005.

[27] http://www.nanotech.wisc.edu/shadow/shadow.html.

[28] F. Schäfers. RAY - the BESSY raytrace program to calculate synchrotron radiation beamlines. Technical Report TB 202, 1996.

[29] F. Schäfers and M. Krumrey. REFLEC - A program to calculate VUV and soft X–Ray optical elements and synchrotron radiation beamlines. Technical Report TB 201, 1996.

[30] http://www.physics.muni.cz/ holy/.

[31] J. E. Harvey, E. C. Moran, and W. P. Zmek. Transfer function characterization of grazing incidence optical systems. Appl. Opt., 27:1527–1533, April 1988.

[32] R. Hudec, L. Pina, A. Inneman, L. Sveda, V. Semencova, M. Skulinova, V. Brozek, M. Mika, R. Kacerovsky, and J. Sik. Novel technologies for x-ray multi-foil optics. In O. Citterio and S. L. O'Dell, editors, *Optics for EUV, X-Ray, and Gamma-Ray Astronomy II. Edited by Citterio, Oberto; O'Dell, Stephen L. Proceedings of the SPIE, Volume 5900, pp. 276-287 (2005).*, pages 276–287, August 2005.

[33] A. Bartnik, H. Fiedorowicz, R. Jarocki, J. Kostecki, R. Rakowski, and M. Szczurek. Wide band laser-plasma soft X-ray source using a gas puff target for direct photo-etching of polymers. In K. M. Abramski, A. Lapucci, and E. F. Plinski, editors, *Infrared Photoelectronics. Edited by Rogalski, Antoni; Dereniak, Eustace L.; Sizov, Fiodor F. Proceedings of the SPIE, Volume 5958, pp. 279-287 (2005).*, pages 279–287, September 2005.

[34] L Sveda, L. Pina, A. Inneman, V. Semencova, J. Marsik, R. Hudec, A. Bartnik, H. Fiedorowicz, R. Jarocki, J. Kostecki, R. Rakowski, and M. Szczurek. Multi-foil optic condenser for a laser plasma EUV source. *Phys. Scr.*, pages 131–134, March 2006.

[35] G. K. Skinner. Coded mask imagers when to use them - and when not. *New Astronomy Review*, 48:205–208, February 2004.

[36] A. Inneman. *Technologické aspekty vývoje a výroby optických prvků pro rentgenové záření.* PhD thesis, Czech Technical University in Prague, Prague, Czech rep., 2001.

[37] L. Sveda, L. Pina, R. Hudec, and A. Inneman. Lobster X-Ray All Sky Monitor. In J.-M. Hameury and J.-P. Lasota, editors, *ASP Conf. Ser. 330: The Astrophysics of Cataclysmic Variables and Related Objects*, pages 487–+, May 2005.

[38] Q. Z. Liu, J. van Paradijs, and E. P. J. van den Heuvel. A catalogue of low-mass X-ray binaries. A&A, 368:1021–1054, March 2001.

[39] H.-J. Grimm, M. Gilfanov, and R. Sunyaev. The Milky Way in X-rays for an outside observer. Log(N)-Log(S) and luminosity function of X-ray binaries from RXTE/ASM data. A&A, 391:923–944, September 2002.

[40] L. Sveda, V. Semencova, A. Inneman, L. Pina, and R. Hudec. Hybrid lobster optic. In G. A. Kyrala, J.-C. J. Gauthier, C. A. MacDonald, and A. M. Khounsary, editors, *Fourth Generation X-Ray Sources and Optics III. Edited by Tatchyn, Roman O.; Biedron, Sandra G.; Eberhardt, Wolfgang. Proceedings of the SPIE, Volume 5918, pp. 22-30 (2005).*, pages 22–30, August 2005.

[41] http://www.rssd.esa.int/index.php?project=XEUS.

[42] L. Šubrt. *Teorie desek a skořepin.* České vysoké učení technické, Prague, Czech rep., 1987.

[43] http://www.niac.usra.edu/files/studies/final_report/389Cash.pdf.

[44] B. E. A. Saleh and M. C. Teich. *Základy fotoniky.* MATFYZPRESS, Prague, Czech rep., 1994.

[45] E. L. Dereniak. *Optical Radiation Detectors.* Wiley, New York, 1984.

[46] http://en.wikipedia.org/wiki/Nonlinear_optics.

[47] R. Molina, J. Nunez, F. J. Cortijo, and J. Mateos. Image restoration in astronomy: a Bayesian perspective. *IEEE Signal Process. Mag*, 18:11–29, March 2001.

[48] J. L. Starck, F. Murtagh, and A. Bijaoui. *Image Processing and Data Analysis; The Multiscale Approach.* Cambridge University Press, Cambridge, 2000.

[49] G. Kaiser. *Friendly Guide to Wavelets.* Birkhauser, Boston, 1994.

[50] T. Lauer. Deconvolution with a spatially-variant PSF. In J.-L. Starck and F. D. Murtagh, editors, *Astronomical Data Analysis II. Edited by Starck, Jean-Luc; Murtagh, Fionn D. Proceedings of the SPIE, Volume 4847, pp. 167-173 (2002).*, pages 167–173, December 2002.

[51] http://en.wikipedia.org/wiki/Karhunen-Lo%C3%A8ve_theorem.